Peter Eshuis

This thesis is the result of four years work in the Physics of Fluids group of Prof. Detlef Lohse at the University of Twente, and partly at the University of Patras with Prof. Ko van der Weele.

Vertically shaken granular matter shows very attractive collective phenomena (see the pictures on this cover), which are studied in this thesis by a combination of experiments, numerical simulations and theoretical analysis.

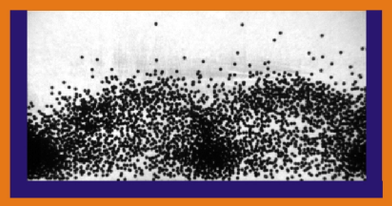

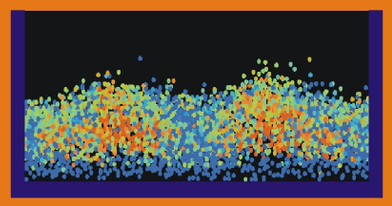

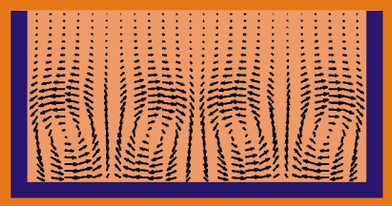

ISBN 978-90-365-2616-6 (February 2008)

Peter Eshuis

Collective Phenomena in Vertically Shaken Granular Matter

Collective Phenomena in Vertically Shaken Granular Matter

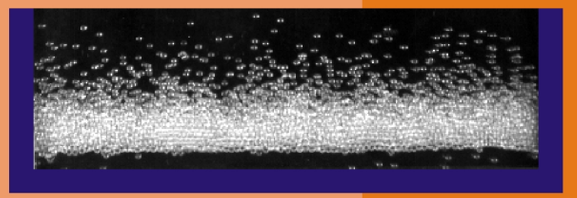

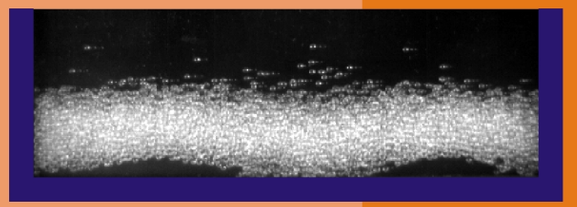

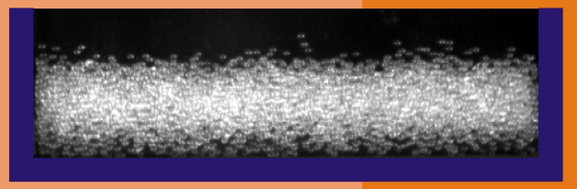

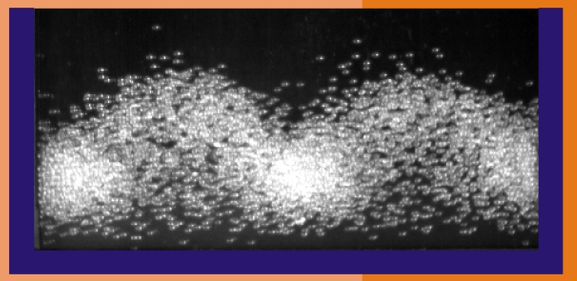

Peter Eshuis

COLLECTIVE PHENOMENA

IN VERTICALLY SHAKEN

GRANULAR MATTER

PETER ESHUIS

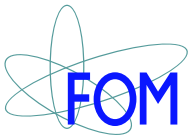

The research described in this thesis is part of the research program of the "Stichting voor Fundamenteel Onderzoek der Materie" (FOM), which is financially supported by the "Nederlandse Organisatie voor Wetenschappelijk Onderzoek" (NWO). It was carried out at the Physics of Fluids research group of the faculty of Science and Technology of the University of Twente.

Hospitality of the University of Patras (Greece) during two work visits is greatly acknowledged.

Nederlandse titel:
Collectieve verschijnselen
in vertikaal geschudde granulaire materie.

Cover design: Peter Eshuis
Front cover - The five phenomena studied in Chapter 2: Bouncing bed, undulations, granular Leidenfrost effect, convection rolls, and granular gas.

Back cover - Three views of the convection rolls as presented in Chapter 4: Experiment, numerical simulation, and hydrodynamic theory.

Publisher:
Peter Eshuis, Physics of Fluids, University of Twente,
P.O Box 217, 7500 AE Enschede, The Netherlands
http://pof.tnw.utwente.nl
http://www.petereshuis.nl

Print: Gildeprint B.V., Enschede

ISBN 978-90-365-2616-6

NEDERLANDS: Onderaan elke pagina is een zogenaamd *flipboek* afgedrukt. Door snel door de pagina's te bladeren vormen de plaatjes een film. Elk plaatje toont 3 deeltjes op een rij, die met elkaar botsen (zie Hoofdstuk 5):

- Oneven pagina's (rechterkant): De botsingen tussen de deeltjes zijn *inelastisch*, wat betekent dat er bij elke botsing energie verloren gaat. Het is precies deze eigenschap die ervoor zorgt dat er zich een cluster van deeltjes aan de rechterwand vormt. (Begin dit flipboek aan het eind van het proefschrift)

- Even pagina's (linkerkant): De botsingen tussen de deeltjes zijn *elastisch*, dat wil zeggen, er gaat nu geen energie verloren tijdens de botsingen. Het resultaat is dat de deeltjes niet gaan clusteren, maar evenredig verdeeld blijven over het systeem. (Begin dit flipboek aan het begin van het proefschrift)

ENGLISH: Two *flip books* are printed on the bottom of every page. When flipping through the pages, the snapshots of 3 particles form a movie (see Chapter 5):

- Odd pages (right hand side): *Inelastic* particle-particle collisions with a restitution coefficient $e = 0.5$, meaning that one half of the velocity is lost in each collision. This inelasticity causes the development of the cluster close to the right wall. (Start this flip book at the end of the thesis)

- Even pages (left hand side): *Elastic* collisions between particles (restitution coefficient $e = 1.0$). No energy is lost in the collisions and the particles remain uniformly distributed over the system. (Start this flip book at the beginning of the thesis)

The initial conditions (particle position and velocity) are the same for both movies and when the leftmost particle hits the left wall, it is given the same fixed velocity; so the only difference between the systems is the value of the restitution coefficient e. The collisions of the rightmost particle with the right wall are completely elastic in both flip books, so no energy is lost here.

Samenstelling promotiecommissie:

Voorzitter	
Prof. dr. ir. L. van Wijngaarden	Universiteit Twente
Promotoren	
Prof. dr. rer. nat. D. Lohse	Universiteit Twente
Prof. dr. J.P. van der Weele	University of Patras (Greece)
Assistent-promotor	
Dr. R.M. van der Meer	Universiteit Twente
Leden	
Prof. dr. H.M. Jaeger	University of Chicago (USA)
Prof. dr. P. Reimann	Universität Bielefeld (Germany)
Prof. dr. B. Nienhuis	Universiteit van Amsterdam
Prof. dr. rer. nat. S. Luding	Universiteit Twente
Dr. ir. M. van Sint Annaland	Universiteit Twente

COLLECTIVE PHENOMENA

IN VERTICALLY SHAKEN

GRANULAR MATTER

PROEFSCHRIFT

ter verkrijging van
de graad van doctor aan de Universiteit Twente,
op gezag van de rector magnificus,
prof. dr. W. H. M. Zijm,
volgens besluit van het College voor Promoties
in het openbaar te verdedigen
op donderdag 14 februari 2008 om 15.00 uur

door

Pieter Gerben Eshuis
(Peter)

geboren op 12 januari 1980

te Hengelo

Dit proefschrift is goedgekeurd door de promotoren:

Prof. dr. rer. nat. Detlef Lohse

Prof. dr. Ko van der Weele

en de assistent-promotor:

Dr. Devaraj van der Meer

Voor mijn ouders

Table of Contents

1 Introduction **1**
1.1 The relevance of granular matter 2
1.2 A guide through the chapters 4
References 8

2 Phase Diagram of Vertically Shaken Granular Matter **11**
2.1 Introduction 12
2.2 Bouncing Bed 14
2.3 Undulations 16
2.4 Granular Leidenfrost effect 22
2.5 Convection rolls 26
2.6 Granular gas 29
2.7 Phase diagram 30
References 34

3 Granular Leidenfrost effect: Experiment and theory of floating particle clusters **41**
3.1 Introduction 42
3.2 Experimental results 43
3.3 Order parameter 45
3.4 Hydrodynamic model 47
3.5 Conclusion 50
References 50

4 Buoyancy Driven Convection in Vertically Shaken Granular Matter: Experiment, Numerics, and Theory **55**
4.1 Introduction 56
4.2 Experimental Setup and Results 58
4.3 Molecular Dynamics simulations 63
4.4 Theoretical Model 65
4.4.1 Granular hydrodynamics 65

4.4.2 Constitutive relations 66
4.4.3 Linearization around the Leidenfrost state 67
4.4.4 Boundary conditions 69
4.4.5 Making the hydrodynamic equations dimensionless 71
4.4.6 Formulation of the eigenvalue problem 75
4.4.7 Linear stability analysis using spectral methods 78
4.4.8 Solution 80
4.5 Comparing Experiment, Numerics, and Theory 83
4.5.1 Cell length Λ vs. Shaking strength S 84
4.5.2 Density profile 86
4.5.3 Velocity profile 88
4.5.4 Temperature profile 89
4.6 Conclusion 90
4.7 Appendix A 91
4.8 Appendix B 93
References 95

5 Granular Hydrodynamics at its Edge: A Horizontal Array of Inelastic Particles 101
5.1 Introduction 102
5.2 Molecular Dynamics simulations 106
5.3 Hydrodynamics of the steady state 108
5.4 Localized-energy-exchange model 113
5.5 Conclusion 114
References 115

6 Granular Realization of the Smoluchowski-Feynman Ratchet 117
6.1 Introduction 118
6.2 Symmetrically coated vanes 120
6.3 Asymmetrically coated vanes: Ratchet 123
6.4 Conclusion 126
References 127

7 Oscillations of Leidenfrost Stars 129
7.1 The Leidenfrost effect 130
7.2 Leidenfrost stars 132
7.3 Drop morphology and particle tracking 134
7.4 Capillary eigenfrequency 136

7.5 Transfer of kinetic energy 139
7.6 Discussion 141
7.7 Conclusion 142
References 142

8 General Conclusion **145**
8.1 Conclusion 146
8.2 Outlook 147
References 150

9 **153**
9.1 Summary 154
9.2 Samenvatting 156
9.3 Publications, Talks, and Posters 159
9.4 About the Author 164
9.5 Over de Auteur 165
9.6 Dankwoord 166

1
Introduction

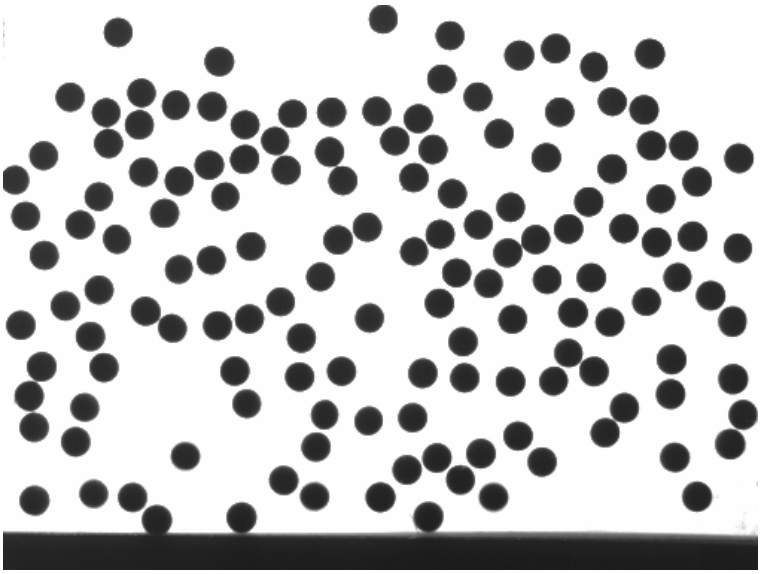

1.1 The relevance of granular matter

Granular, grain-like materials can be encountered anywhere: In everyday life one can think of sugar, salt and cereals (to name a few), and also in industries like the pharmaceutical and food industry the examples are numerous. The chemical industry for example is heavily dominated by these materials: More than 75% of the raw materials and half of their final products are in the form of granular matter [1].

One of the problems with granular matter that arise in nature occurs when sand dunes move slowly but steadily through the desert. Although the maximum speed of a dune is only 100 meter a year (under the most favorable circumstances [2]), it can easily "stroll" onto a road or swallow the suburbs of a city like Nouakchott in Mauritania (see Fig. 1.1).

In industry problems can arise while transporting, handling, or storing granular materials, see for example the collapsed silo of Fig. 1.1. Annually about 1000 silos fail in North-America alone due to avoidable design problems [3].

Figure 1.1: Sugar and pills are examples of granular materials. Problems with granular matter become visible in the large dune threatening to swallow the city of Nouakchott (capital of Mauritania) and the collapsed silo.

Another study showed that start-up problems under 39 new granular solids-processing plants were considerable [4]: The scheduled start-up time was three months on average, but the actual time needed to start up was nine months on average, and one third of the plants even needed more than one year. The delay was usually caused by granular materials forming a plug, sticking together, flowing unevenly or uncontrollably.

Globally about 10% of the energy is consumed by the industries processing granular matter and approximately 40% (500 billion dollar) of this energy is wasted due to problems with a granular origin as sketched above [3].

A lot of engineering experience has been applied directly to industrial problems, but the persistence of these problems indicates that there is a great demand for fundamental research to get a better understanding of the underlying physics in granular systems.

Even though these materials seem so ordinary, since they appear to behave like a normal solid, liquid or a gas (see Fig. 1.2), they often show counterintuitive effects and differ to some extent from these normal states of matter. Therefore granular matter is often referred to as the fourth state of matter [5–7]. Compare for example an hourglass with a water clock (or "clepsydra"). The flow rate of a running water clock decreases rapidly, due to the decreasing hydrostatic pressure in the upper vessel. By contrast, the sand in the hourglass runs at a constant speed. The reason for this behavior is that there is hardly any build-up of the pressure inside the sand, because arch-like structures redirect the pressure of the sand towards the wall of the hourglass. This results in an almost constant pressure at the orifice and therefore an almost empty hourglass flows just as fast as a full one.

Fundamental research on granular matter started to receive increasing atten-

Figure 1.2: Granular matter can behave either like a solid (sand castle), a liquid (hourglass) or a gas (sandstorm).

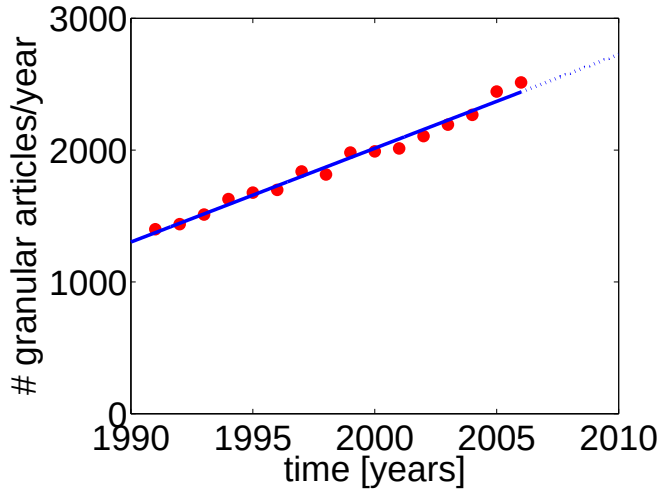

Figure 1.3: The number of articles containing the word "granular" in the title or abstract published annually since 1991 (based on Web of Science). The straight line is a linear fit through the data with a slope 71 articles/year^2.

tion around 1990. This is reflected by Fig. 1.3, which shows the growth in the annual number of articles published in this relatively young branch of physics. The number of articles on granular research published each year has doubled in the past 15 years.

This thesis focuses on granular matter that behaves solid-, liquid-, or gas-like when shaken vertically. The collective phenomena observed in this system often show a mix of these states. To describe these phenomena hydrodynamic models are used, adapted to granular materials. This is in the spirit of what is probably the most important question in granular research today: "To what extent can hydrodynamic-like models describe phenomena observed in granular systems?" [8–12]. This thesis combines experiments, molecular dynamics simulations, and theoretical analysis. All three are found to agree very well, shedding light on the degree to which hydrodynamics can be applied to vertically shaken granular matter.

1.2 A guide through the chapters

In Chapter 2 an experimental phase diagram for a quasi 2-D system is constructed, giving an overview of the wide range of collective phenomena observed in ver-

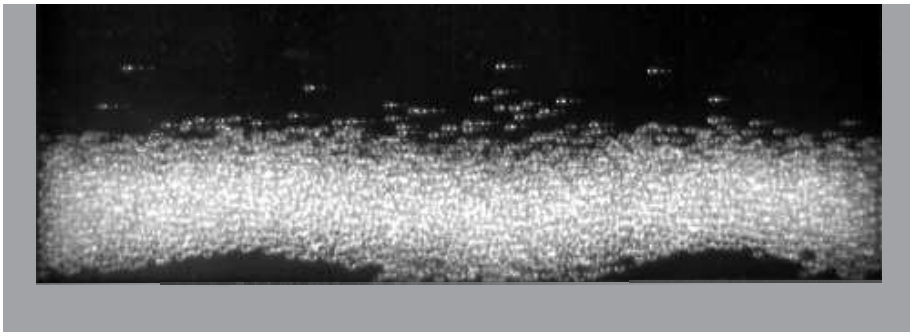

Figure 1.4: Undulations, a standing wave pattern, showing up in the experimental phase diagram of Chapter 2.

tically shaken granular matter; bouncing bed, undulations, granular Leidenfrost effect, convection rolls, and granular gas. These phenomena and the transitions between them are characterized by the following dimensionless control parameters: the shaking acceleration Γ, the shaking strength S, and the number of particle layers F.

The granular version of the Leidenfrost effect, in which a dense cluster floats on a dilute layer of fast particles, is the subject of Chapter 3. The granular Leidenfrost effect is observed above a critical shaking strength and for a sufficient number of particles in a 2-D setup. The experimental observations are success-

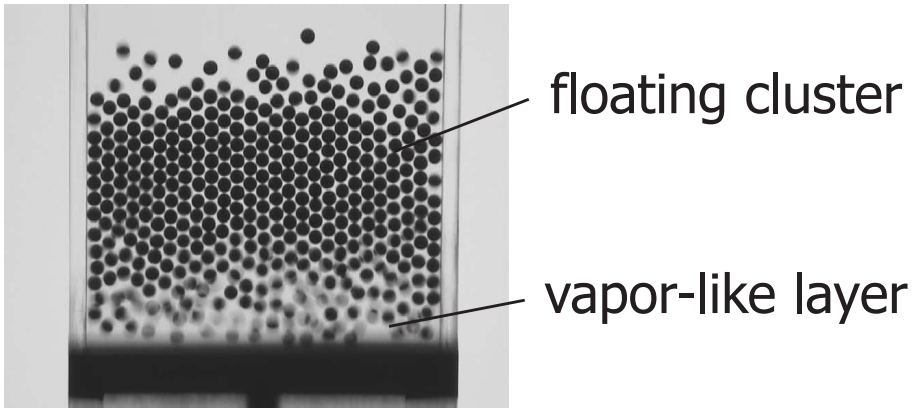

Figure 1.5: The granular Leidenfrost effect is successfully described by a hydrodynamic model in Chapter 3.

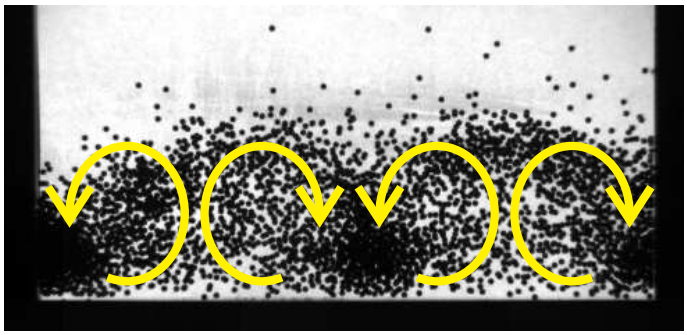

Figure 1.6: Granular convection is studied in Chapter 4 by means of experiment, simulations and theoretical analysis. The observed effects are qualitatively and quantitatively captured by a hydrodynamic model.

fully explained by a hydrodynamic model, which makes the granular Leidenfrost effect a prime example of a granular system captured by hydrodynamic equations.

Buoyancy driven granular convection is studied for a quasi 2-D system in Chapter 4. Counter-rotating convection rolls with pronounced density variations are formed at strong shaking strengths. The experimental observations are confirmed by numerical simulations and the onset of convection is correctly described by a linear stability analysis of the hydrodynamic model presented in Chapter 3.

Chapter 5 discusses the horizontal 1-D system of inelastic particles introduced by Du, Li, and Kadanoff [8], which is essentially a horizontal version of the granular Leidenfrost effect: In the characteristic steady state a single particle commutes between the driving wall and a dense cluster (see Fig. 1.7). The main reason why we study this system is not the analogy with the Leidenfrost effect, but something which is more central to the scope of this thesis: We show that this system marks the precise extent to which granular hydrodynamics can go. The density is well captured by a hydrodynamic description incorporating the finite size of the

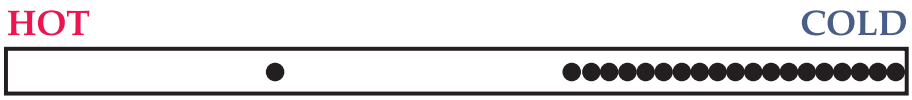

Figure 1.7: The horizontal array of inelastic particles of Chapter 5: A single particle commutes between the hot left side and an almost immobile cluster at the right.

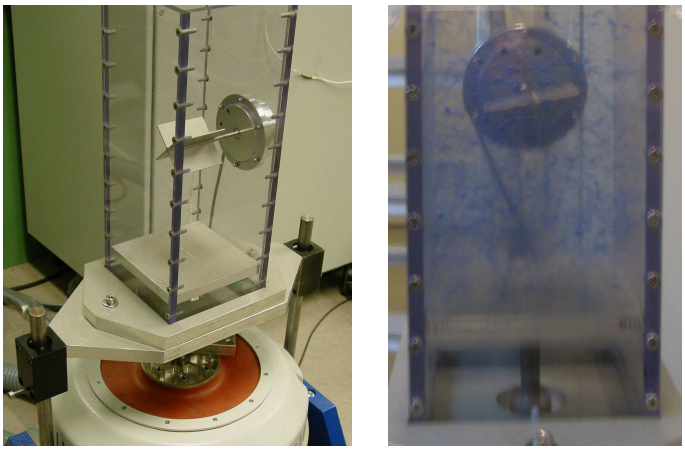

Figure 1.8: The first granular realization of the Smoluchowski-Feynman ratchet, presented in Chapter 6.

particles. The temperature profile, however, is not described by the hydrodynamic equations, since all energy exchange is localized at the border of the cluster: Granular hydrodynamics at its edge.

In Chapter 6 we present the first granular realization of the Smoluchowski-Feynman ratchet. It consists of four vanes that are allowed to rotate freely in a vertically shaken granular gas. The two sides of the vanes are coated differently to induce a preferential direction of rotation, i.e., the ratchet effect.

Originally, in the Gedankenexperiment of Smoluchowski [14] and Feynman [15] the device was submerged in a heat bath at thermal equilibrium, where the second law of thermodynamics prohibits any ratchet effect: No work can be extracted spontaneously from an environment in thermodynamic equilibrium. The granular gas, however, is far from equilibrium, so the granular ratchet *can* work. The device cleverly translates the energy from its noisy environment (which is pumped into the system by the vibrating bottom) into a directed motion. After various chemical motors on the micro-scale [16], this is the first macroscopic Smoluchowski-Feynman ratchet, and the first one that is able to sustain a continuous rotation.

The Leidenfrost effect is the phenomenon that a drop of water can float on its own vapor layer over a hot plate for a long time. Chapter 7 studies the star-like shape oscillations of such a Leidenfrost drop, i.e., Leidenfrost stars. Particle

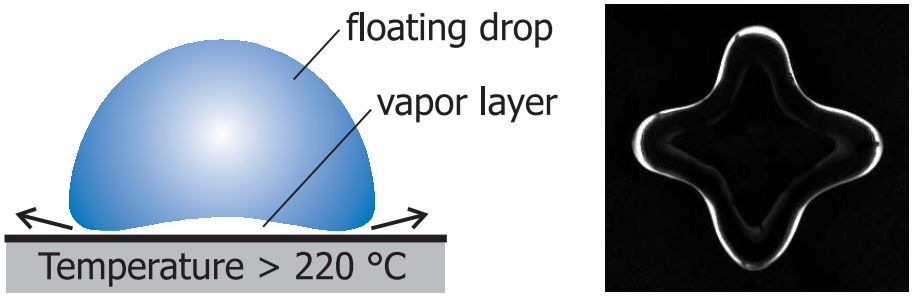

Figure 1.9: The floating drop of water of the Leidenfrost effect shows rapid shape oscillations: Leidenfrost star (Chapter 7).

tracking within the drop reveals that these lateral shape oscillations form just one of the possible modes of motion in which the symmetry of the floating drop is broken. The observed transitions between these modes correspond to a transfer of kinetic energy.

Finally, the thesis ends with a general conclusion and outlook in Chapter 8.

References

[1] R. M. Nedderman, *Statics and kinematics of granular materials* (Cambr. Univ. Press, Cambridge, UK, 1992).

[2] V. Schwämmle and H. J. Herrmann, *Solitary wave behaviour of sand dunes*, Nature **426**, 619 (2003).

[3] T. M. Knowlton, J. W. Carson, G. E. Klinzing, and W-C. Yang, *The importance of storage, transfer and collection*, Chem. Eng. Prog. **90**, 44 (1994).

[4] E. W. Merrow, *Estimating startup times for solids-processing plants*, Chem. Eng. **10**, 89 (1988).

[5] H. M. Jaeger and S. R. Nagel, *Physics of the granular state*, Science **255**, 1523 (1992).

[6] H. M. Jaeger, S. R. Nagel, and R. P. Behringer, *Granular solids, liquids, and gases*, Rev. Mod. Phys. **68**, 1259 (1996).

[7] R. P. Behringer H. M. Jaeger, S. R. Nagel, *The physics of granular materials*, Physics Today **49**, 32 (1996).

[8] Y. Du, H. Li, and L. P. Kadanoff, *Breakdown of hydrodynamics in a one-dimensional system of inelastic particles*, Phys. Rev. Lett. **74**, 1268 (1995).

[9] L. P. Kadanoff, *Built upon sand: Theoretical ideas inspired by granular flows*, Rev. Mod. Phys. **71**, 435 (1999).

[10] J. Duran, *Sand, Powders and Grains: An Introduction to the Physics of Granular Materials* (Springer-Verlag, New-York, 1999).

[11] I. Goldhirsch, *Rapid granular flows*, Annu. Rev. Fluid Mech. **35**, 267 (2003).

[12] I. S. Aranson and L. S. Tsimring, *Patterns and collective behavior in granular media: Theoretical concepts*, Rev. Mod. Phys. **78**, 641 (2006).

[13] J. G. Leidenfrost, *De Aquae Communis Nonnullis Qualitatibus Tractatus* (University of Duisburg, Duisburg, Germany, 1756), translated into English in: Int. J. of Heat and Mass Transfer **9**, 1153 (1966).

[14] M. Smoluchowski, *Experimentell nachweisbare, der üblichen thermodynamik widersprechende Molekularphänomene*, Physik. Zeitschr. **13**, 1069 (1912).

[15] R. P. Feynman, R. B. Leighton, and M. Sands, *The Feynman Lectures on Physics*, Vol. **1**, Ch. 46 (Addison-Wesley, Reading, MA, 1963).

[16] P. Reimann, *Brownian motors: Noisy transport far from equilibrium*, Phys. Reports **361**, 57 (2002).

2

Phase Diagram of Vertically Shaken Granular Matter

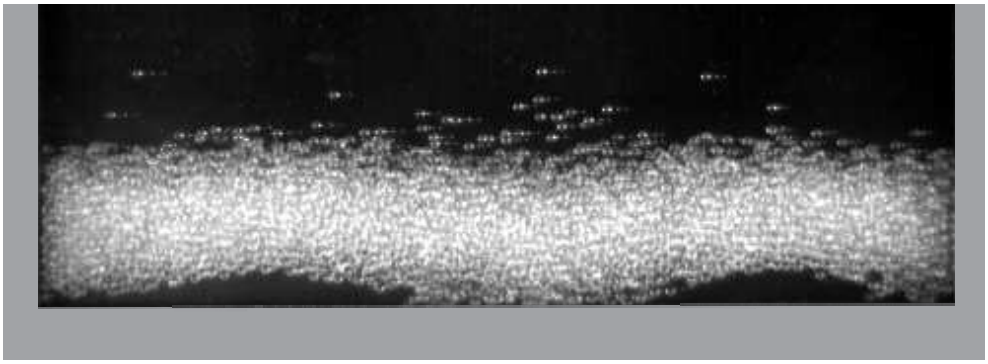

Peter Eshuis, Ko van der Weele, Devaraj van der Meer, Robert Bos, and Detlef Lohse, *Physics of Fluids* **19**, 123301 (2007).

A shallow, vertically shaken granular bed in a quasi 2-D container is explored experimentally yielding a wider variety of phenomena than in any previous study: (1) bouncing bed, (2) undulations, (3) granular Leidenfrost effect, (4) convection rolls, and (5) granular gas. These phenomena and the transitions among them are characterized by dimensionless control parameters and combined in a full experimental phase diagram.

2.1 Introduction

Vertically shaken granular matter exhibits a wealth of fluid-like phenomena: Undulations [1–3] and other wave patterns [4, 5] (comparable to Faraday waves in an ordinary liquid [6, 7]), the granular Leidenfrost effect [8] (being the granular version of the synonymous effect of a water drop hovering over a hot plate [9]), and convection rolls reminiscent of those found in a fluid heated from below beyond the Rayleigh-Bénard instability [10, 11]. However, while in normal fluids and gases these phenomena are fully understood, this is much less the case for their granular counterparts. One of the major challenges in granular research today is to achieve a hydrodynamic-like description of these effects, and although such a description has been given successfully for some isolated cases, we are still far from an overall theory.

An indispensable step towards any such theory, and an important indication of the physical mechanisms at work, is the determination of the dimensionless control parameters that govern the phenomena. Here we present an experimental study of a vibrated bed of glass beads in which we do exactly this: For each observed effect (and the phase transitions between them) we identify the relevant control parameters. The paper culminates in the construction of an experimental phase diagram in which all observed phenomena are combined.

Our experimental setup (Fig. 2.1) consists of a quasi 2-D Perspex container of dimensions $L \times D \times H = 101 \times 5 \times 150$ mm (with L the container length, D the depth, and H the height), partially filled with glass beads of diameter $d =$ 1.0 mm, density $\rho = 2600$ kg/m^3, and coefficient of normal restitution $e \approx 0.95$. The setup is mounted on a sinusoidally vibrating shaker with tunable frequency f and amplitude a. Most of the experiments presented in this paper are performed by upsweep experiments in which the frequency is increased linearly at 75 Hz/min. These experiments are recorded with a high-speed camera capturing 2000 frames; adequate recording times ($4 - 16$ s) are obtained by adjusting the frame rate.

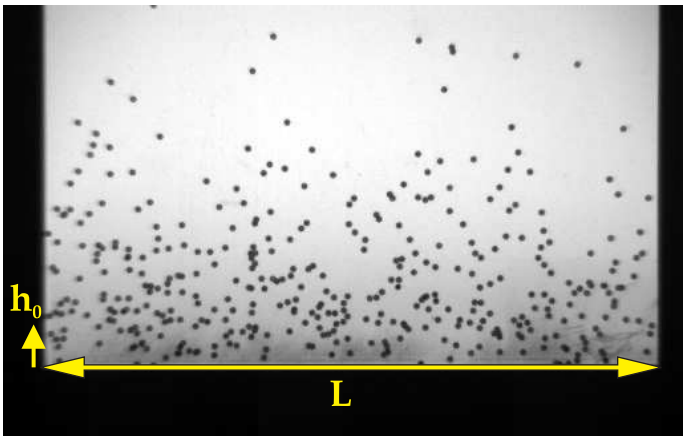

Figure 2.1: The experimental setup in which glass beads of diameter $d = 1.0$ mm are vibrofluidized. The length of the container is $L = 101$ mm; the bed height at rest (h_0) is varied in our experiments such that the aspect ratio L/h_0 always remains large. The container depth is only five particle diameters, making the setup quasi two-dimensional.

The natural dimensionless control parameters to analyze the experiments are (i) the shaking parameter $a^2\omega^2/g\ell$ (with $\omega = 2\pi f$ and $g = 9.81$ m/s^2), being the ratio of the kinetic energy inserted into the system by the vibrating bottom and the potential energy associated with a typical displacement of the particles ℓ; (ii) the number of bead layers F; (iii) the inelasticity parameter $\varepsilon = (1 - e^2)$; and (iv) the aspect ratio L/h_0, where h_0 denotes the bed height at rest. The parameter ε is taken to be constant in this paper, since we ignore the velocity dependence and use the same beads throughout. The aspect ratio varies by changing the bed height h_0 (i.e., the number of layers F) but remains large in all experiments; i.e., $L/h_0 \gg 1$. We will systematically vary the first two dimensionless parameters, by changing the amplitude a, the frequency f, and the number of layers F.

The most intriguing of the four parameters above is the first one, the shaking parameter, since the typical displacement of the particles ℓ is influenced in a non-trivial way by the vibration intensity and the number of particle layers. For *mild* fluidization, the displacement of the particles is determined by the amplitude of shaking a, since the bed closely follows the motion of the bottom. The energy ratio in this case becomes identical to the well-known dimensionless shaking acceleration

$$\Gamma = \frac{a\omega^2}{g}. \tag{2.1}$$

For *strong* fluidization, the particles no longer follow the bottom, so (instead of a) some intrinsic length scale needs to be taken for ℓ, such as the particle diameter d. This leads to the dimensionless shaking strength S (see Refs. [8] and [12])

$$S = \frac{a^2\omega^2}{gd}. \tag{2.2}$$

At intermediate fluidization, we will encounter phenomena in which there is a competition of length scales. In this region the transitions are affected by changing one of the competing length scales, meaning that the choice of the appropriate shaking parameter is not a priori clear. This will become an issue in particular for the transition from undulations to the granular Leidenfrost effect described in Section 2.4.

In the following Sections, the various phenomena observed in our system are discussed one by one, in the order in which they appear as the fluidization is increased: bouncing bed (Section 2.2), undulations (Section 2.3), granular Leidenfrost effect (Section 2.4), convection rolls (Section 2.5), and granular gas (Section 2.6). Finally, in Section 2.7 all five phenomena will be combined in a phase diagram of the relevant shaking parameter versus the number of layers.

2.2 Bouncing Bed

For shaking accelerations $\Gamma \leq 1$ (and even for Γ slightly above 1) the granular bed behaves as a solid, co-moving with the vibrating bottom and never detaching from it. In order to detach, the bottom must at some point during the cycle have a downward acceleration that overcomes gravity (as for a single bouncing ball [13, 14]) *plus* the friction between the bed and the walls of the container. These walls carry a considerable portion of the bed weight, as described in the Rayleigh-Janssen model [15, 16] by the detachment condition for the dimensionless shaking acceleration:

$$\Gamma_{detach} = 2 - e^{-\chi}, \text{ with } \chi = K\mu_s\xi. \tag{2.3}$$

Here χ is the decompaction parameter, which is defined by the coefficient of redirection toward the wall K, the static friction coefficient for Perspex $\mu_s = 0.8$ and the ratio of the contact area over the cross-sectional area ξ:

$$\xi = \frac{Ph_0}{A} = \frac{2(D+L)h_0}{DL} \quad \rightarrow \quad \xi = \frac{2h_0}{D} \ (D \ll L), \tag{2.4}$$

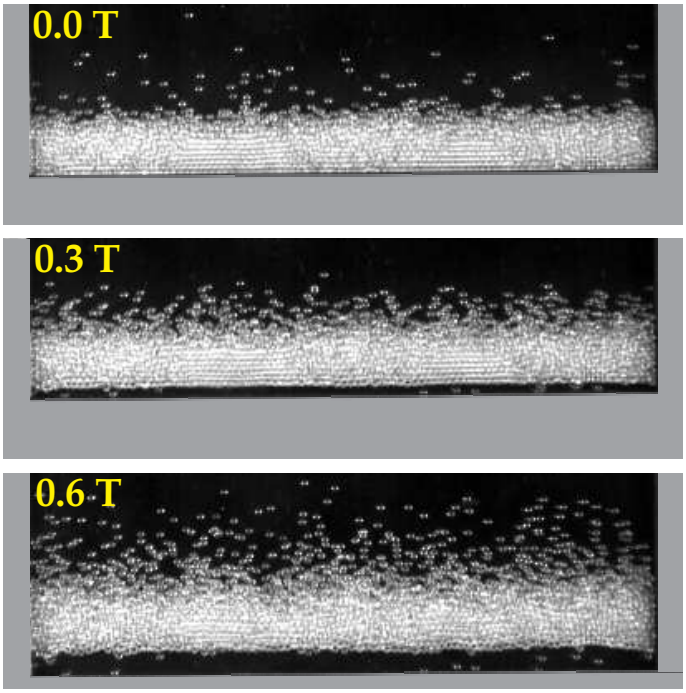

Figure 2.2: Time-series of a bouncing bed for $F = 8.1$ layers of $d = 1.0$ mm glass beads at shaking acceleration $\Gamma = 2.3$ ($a = 4.0$ mm, $f = 12.0$ Hz). The phase of the sinusoidally vibrating bottom is indicated in each snapshot, where T is the period of shaking [$y_{bottom}(t) = a\sin(2\pi t/T)$]. The friction between the particles and the container walls causes the downward curvature of the bed close to the sidewalls that is visible in the lower snapshot.

where P is the perimeter, h_0 the bed height at rest, and A the cross-sectional area of the container. Once the detachment condition of Eq. (2.3) is fulfilled, the bed bounces in a similar way as a single particle would do: We call this a bouncing bed, see Fig. 2.2.

The value of Γ at which the transition from solid to bouncing bed occurs in experiment has been determined by gradually increasing the frequency f (for three fixed shaking amplitudes $a = 2.0,\ 3.0$, and 4.0 mm). The onset value grows with the number of layers F, as shown in Fig. 2.3. The reason for this is the larger contact area with the front- and sidewalls (larger ξ) causing a proportionally higher frictional force, leading to a higher value of Γ_{detach} as described by Eq. (2.3). To compare the model with the experiments we have to take into account that the forces in our quasi 2-D setup ($D \ll L$) are redirected weaker in comparison with

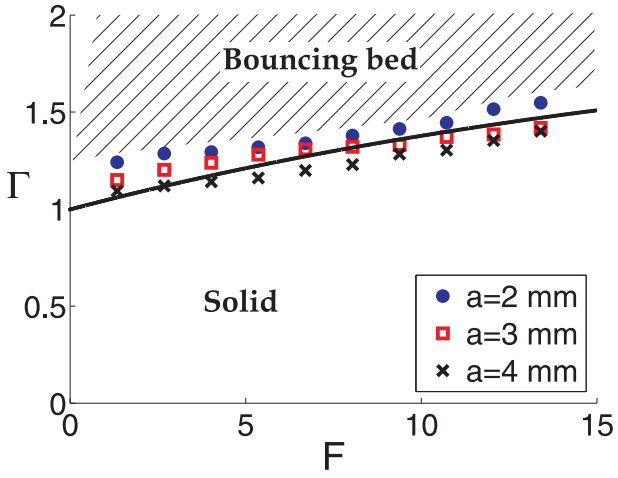

Figure 2.3: The transition from solid behavior to bouncing bed is governed by the shaking parameter Γ. The critical value (here determined for three fixed amplitudes: $a = 2.0, 3.0, 4.0$ mm) increases with the number of particle layers F following the Rayleigh-Janssen model (solid line) with the redirection coefficient ($K = 0.15$) adapted to our quasi 2-D setup.

the 3-D situation of the Rayleigh-Janssen model. Thus, the redirection coefficient K is expected to be smaller than the value for a compact triangular packing ($K = 0.58$). This is indeed found, the best fit through the experimental data of Fig. 2.3 is achieved for $K = 0.15$.

Figure 2.3 indicates that for the current transition (which occurs at mild fluidization) Γ is a good dimensionless parameter, as explained in the Sec. 2.1. It is not ideal, as exemplified by the fact that the onset values do not exactly coincide for the different amplitudes of shaking, but for a different choice of the shaking parameter (S), the onset values differ much more.

2.3 Undulations

Starting from a bouncing bed and increasing the shaking frequency f, three different phenomena are observed: (a) For $F \leqslant 3$ layers the bed is vaporized and becomes a granular gas (Sec. 2.6); (b) for $3 < F \leqslant 6$ convection rolls form (Sec. 2.5); and (c) for $F > 6$ layers the bed develops standing waves oscillating at twice the period of shaking (known as "undulations", "arches", "ripples", or "$f/2$-

waves" [1, 3–5, 17]), and these will be covered in this section.

In the undulations regime, the granular bed shows standing wave patterns similar to a vibrating string as shown in Fig. 2.4. The container (length L) accommodates an integer number n of half-wavelengths of the granular string:

$$L = n\frac{\lambda}{2}, \quad n = 1,2,3,\ldots, \tag{2.5}$$

where λ is the length of one arch in the undulation pattern. This λ represents a new length scale in the system besides the shaking amplitude a and the particle diameter d. Unlike these previous length scales, λ is connected to the elastic properties of the particles, which play an important role in the undulations.

We observe that each collision with the bottom causes a shock wave through the bed at a roughly constant speed v. This sends compaction waves along the

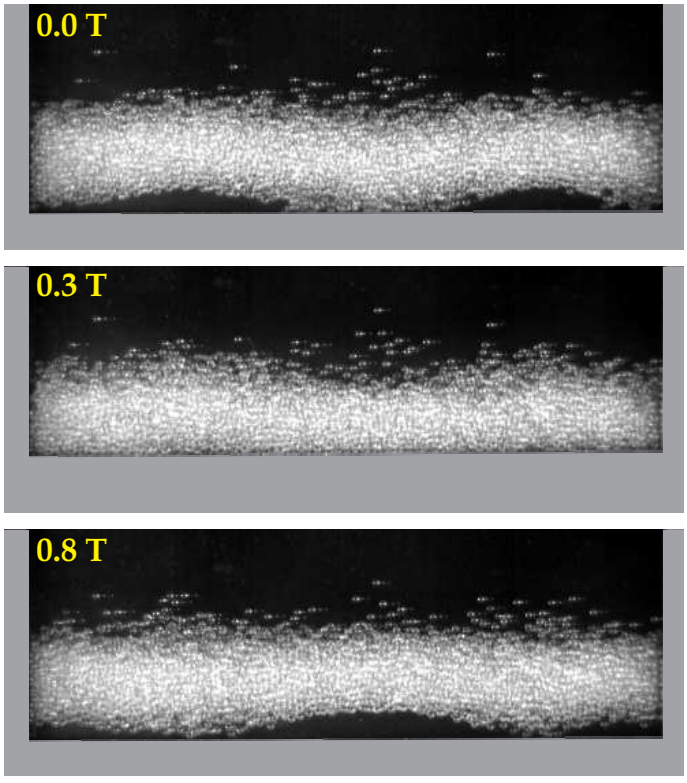

Figure 2.4: One complete standing-wave cycle of the $n = 4$ undulation mode for $F = 9.4$ particle layers at $\Gamma = 12$ ($a = 2.0$ mm, $f = 39.3$ Hz). The undulation cycle takes $2/f$; i.e., twice the period of shaking.

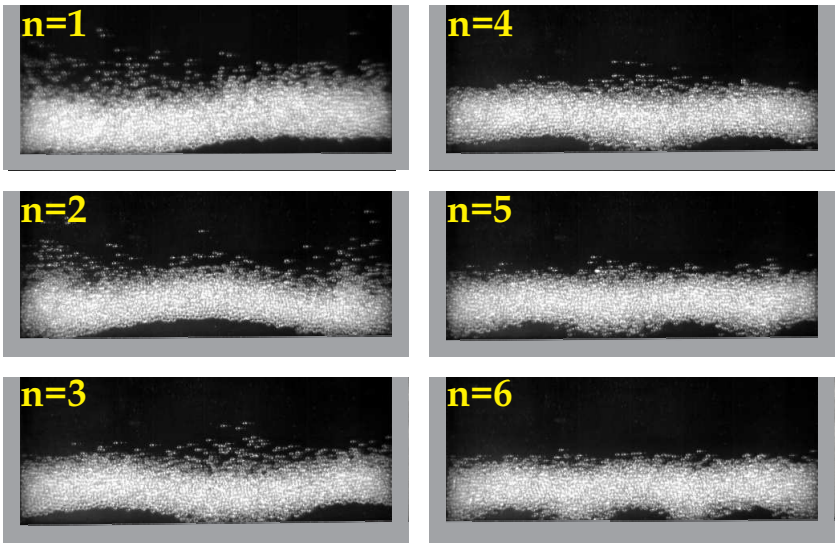

Figure 2.5: Six successive undulation modes, for $F = 9.4$ layers and $a = 2.0$ mm, at shaking frequencies $f = 29.0$, 32.6, 38.2, 39.3, 46.1, 50.2 Hz. The mode number n (the number of half-wavelengths fitting the container length L) increases with the shaking intensity.

arch, starting out from the lower parts and meeting in the center. At this point the waves bring each other to a halt and the center falls down to the bottom. (At the same time, the previous lower parts are now elevated.) This occurs after one shaking period and the collision with the bottom generates new shock waves, repeating the series of events. In our experiments the undulation modes are always perpendicular to the sidewalls; i.e., they show either a minimum or a maximum there. This same boundary condition was also found by Sano [3]. We propose the following physical reason: Whenever the bed does not move perpendicularly to the wall, the particles will bounce off the sidewall instead of being halted by it, and as a result the undulation mode is adjusted or shifted until it is perpendicular to the wall.

Since it takes precisely two shaking periods to complete one full oscillation of the undulation pattern (meaning that the minima and maxima exchange positions every vibration cycle), the successive undulation modes appear with increasing steps of half a wavelength.

Generally, the first undulation to be formed is the $n = 1$ mode, and for increasing shaking intensity the higher modes depicted in Fig. 2.5 successively appear. They are triggered by the horizontal dilatancy the bed experiences when it collides

with the vibrating bottom [3]: the string of particles along the bottom *dilates* and beyond a certain threshold, *buckling* will occur, which forces the particles into an arch. Using this physical picture, Sano [3] was able to derive a theoretical form of the undulation modes, which agrees with the form of the experimental ones in Fig. 2.5. Let s denote the position along the length of the layer, following the contour of the undulation, and $\theta(s)$ the angle the bed makes (at position s) with the horizontal x-axis. This angle is governed by [3]

$$\frac{d^2\theta}{ds^2} = -\alpha^2 \sin\ \theta. \tag{2.6}$$

Here $\alpha = \sqrt{F/\widetilde{E}I}$, with F the reaction force from the side walls upon both ends of the bed, $\widetilde{E}$ the effective Young's modulus of the bed, and I its moment of inertia.

Equation (2.6) is the well-known pendulum equation with s instead of the time t. It can be solved analytically in terms of the Jacobi elliptic functions [3], but for our purposes it is sufficient to consider the small angle approximation, $\sin\ \theta \approx \theta$, which simplifies the problem to that of a harmonic oscillator. Inserting the boundary conditions $\theta(0) = 0$ and $\theta(L) = 0$ (the bed is horizontal at both ends, as discussed above), this yields the following solution:

$$\theta(s) = \theta_{max}\ \sin\left(\frac{n\pi s}{L}\right), \tag{2.7}$$

with θ_{max} denoting the maximal angle with the horizontal x-axis (which is an increasing function of the mode number n). In the small angle approximation, the horizontal distance x is equal to the measured length along the undulation layer ($x \approx s$), so the shape of the undulation modes can simply be calculated by integrating Eq. (2.7) over x:

$$y(x) = \theta_{max}\frac{L}{n\pi}\left[1 -\ \cos\left(\frac{n\pi x}{L}\right)\right], \quad n = 1,2,3,\ldots. \tag{2.8}$$

The profiles generated by Eq. (2.8) match the experimental modes of Fig. 2.5 very well.

In our experiments, we first focused on the transition from the bouncing bed behavior to the $n = 1$ mode. In Fig. 2.6 this transition is shown in the (Γ, F)-phase diagram for three fixed amplitudes of shaking, $a = 2.0$, 3.0, and 4.0 mm. We observe that the onset value of Γ decreases with growing number of layers F. The reason for this is that the necessary horizontal dilation (of the lower layer) upon

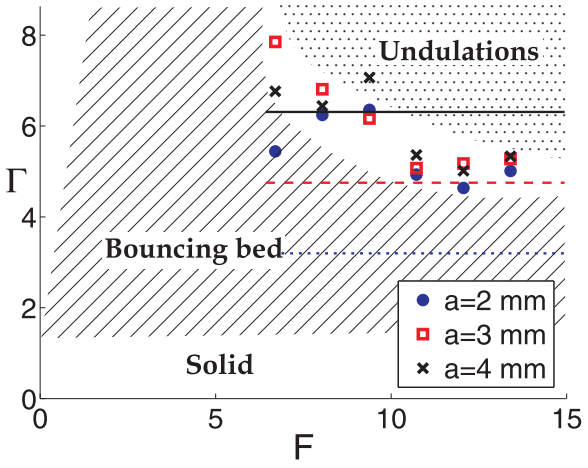

Figure 2.6: The transition from bouncing bed to undulations in the (Γ, F)-plane, for three fixed values of the shaking amplitude ($a = 2.0, 3.0, 4.0$ mm). The critical value of the shaking acceleration Γ decreases with growing number of particle layers F, since the horizontal dilation of the bottom layer (required to trigger undulations, see text) becomes more pronounced as a result of the extra layers on top. The horizontal lines correspond to the onset of undulations predicted by Eq. (2.9) with $n = 1$, where the dotted blue line corresponds to $a = 2.0$ mm, the dashed red line to $a = 3.0$ mm and the solid black line to $a = 4.0$ mm.

impact with the bottom is more readily accomplished due to pressure from the extra layers on top.

It is seen in Fig. 2.6 that the data for the three different shaking amplitudes coincide reasonably well, except at the threshold value of $F = 6$ layers. Presumably, at this small value of F the dilation can only become sufficient if the density is locally enhanced by a statistical fluctuation; were the experiment repeated many times, the agreement between the averaged data for various a would be expected to become better. For $F < 6$ layers no undulations are found, since the particle density is then definitely too small (even in the presence of fluctuations) to reach the required level of dilation.

The undulation regime lies in the area of mild fluidization, and Fig. 2.6 shows that the dimensionless shaking acceleration Γ [see Eq. (2.1)] is indeed the appropriate governing parameter for the undulation phase, in agreement with what has been reported in the literature. Many researchers constructed a phase diagram using $\Gamma = a(2\pi f)^2/g$ in combination with $f^* = f\sqrt{h_0/g}$, which however

are not independent of each other [3, 5, 18, 19]. We use the (Γ, F)-phase diagram, in which the two control parameters are independent, as was also done by, e.g., Wassgren *et al.* [20] and Hsiau and Pan [21].

Now we come to the higher undulation modes. We have already mentioned the role played by shock waves in the formation of undulations. Such a compaction wave starts out from the lower regions, propagates along the arch, and is halted in the center by its counterpart going in the opposite direction. Hence, these shock waves travel a distance $\frac{1}{2}\lambda = L/n$ in one period of shaking $T = 1/f$; i.e., their speed is given by $v = Lf/n$. We know from the experiments that the speed of the shock waves decreases roughly linearly from $v = 2$ m/s for $n = 1$, to $v = 1$ m/s for the $n = 6$ mode, caused by the lower density inside the granular bed at higher fluidization. Thus, we can estimate the shaking frequency f_n at which a certain mode will appear:

$$f_n = \frac{nv(n)}{L}. \tag{2.9}$$

Equation (2.9) predicts the onset of undulations [i.e., the first mode $n = 1$, with $v(1) = 2$ m/s] reasonably well, as shown in Fig. 2.6. The higher undulation modes observed for shaking amplitude $a = 2.0$ mm are displayed in Figure 2.7 along with the location of the transitions for the various undulation modes n based on Eq. (2.9). The location of these transitions is a fair match to the experimental findings, which may be taken as a confirmation of the shock-wave mechanism described above.

As already observed in Fig. 2.5 and demonstrated in Eq. (2.9), the mode number n increases for growing Γ. However, the sequence of modes is seen to be interrupted somewhere in the middle: Here the undulation pattern gives way to the granular Leidenfrost state [8], in which a cluster of slow particles is floating on top of a dilute layer of fast particles. Normally, this state appears at the end of the undulation regime (see Sec. 2.4), but when a certain standing wave pattern is energetically unfavorable the system chooses the Leidenfrost state instead: In Fig. 2.7 we see that this happens to the $n = 3$ undulation, which is completely skipped from the sequence for $F \gtrsim 12$ layers. This can be understood from the fact that the $n = 3$ mode has an antinode at the sidewall (i.e., a highly mobile region), whereas the friction with the wall tends to slow down the particles here. This inherent frustration gives rise to the appearance of the granular Leidenfrost effect.

Likewise, the small Leidenfrost region for $9 \leq F \lesssim 12$ below the onset line of the $n = 5$ undulation has to do with a frustrated $n = 5$ mode. The frustration is, however, not strong enough to skip the mode entirely as in the $n = 3$ case. In

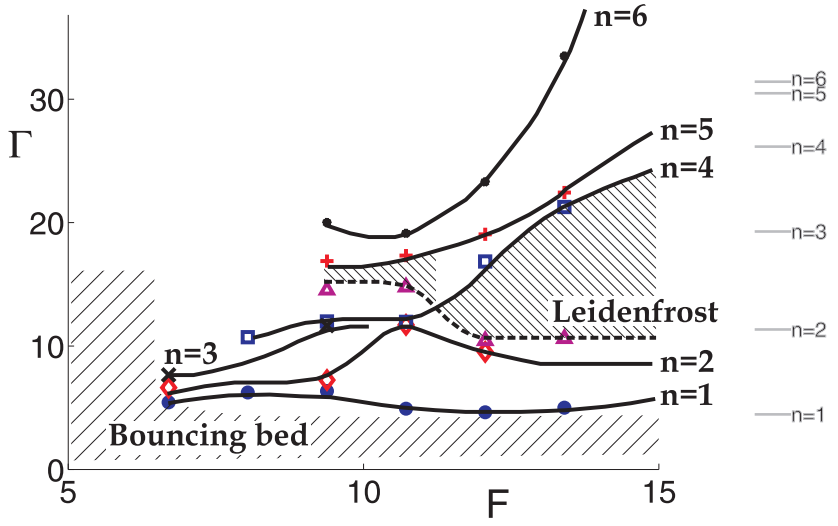

Figure 2.7: The onset of the successive undulation modes $n = 1, 2, .., 6$ at a fixed shaking amplitude $a = 2.0$ mm. The mode number n increases with the shaking parameter Γ, but occasionally the undulations give way to the granular Leidenfrost effect (the hatched regions above the dashed curve), where a dense cluster without any arches is floating on a uniformly dilute granular layer. The grey lines on the right indicate the location of the various undulation modes based on Eq. (2.9) and agree reasonably with the experimental observations. The black lines are a guide to the eye.

our experiments, the intermediate Leidenfrost regions become smaller for larger shaking amplitude a. For $a = 4.0$ mm they have disappeared altogether from the undulation regime, as will be shown in Sec. 2.7.

2.4 Granular Leidenfrost effect

When the shaking frequency is increased beyond a critical level, the highest undulation mode becomes unstable and we enter the granular Leidenfrost regime [8], see Ch. 3: Here a dense cloud of particles is elevated and supported by a dilute gaseous layer of fast beads underneath, see Fig. 2.8. The bottom layer of the undulations is completely evaporated and forms the gaseous region on which the cluster floats. The phenomenon is analogous to the original Leidenfrost effect in which a water droplet hovers over a hot plate on its own vapor layer, when the temperature of the plate exceeds a critical value [9]. The vaporized lower part of

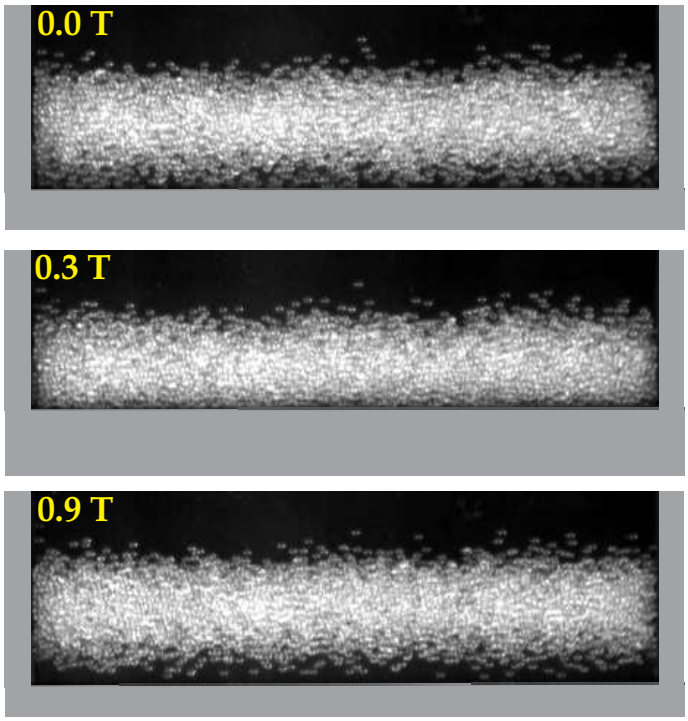

Figure 2.8: Snapshots of the granular Leidenfrost effect for $F = 8.1$ particle layers shaken at $f = 43.0$ Hz and $a = 3.0$ mm (corresponding to a dimensionless acceleration $\Gamma = 22$ or shaking strength $S = 67$). A dense cluster is elevated and supported by a dilute layer of fast particles underneath. The cluster never touches the vibrating bottom, which makes this state distinctively different from the bouncing bed or the undulations.

the drop provides a cushion to hover on, and strongly diminishes the heat contact between the plate and the drop, enabling it to survive for a relatively long time.

In Fig. 2.9 the transition from the undulations to the granular Leidenfrost state is shown, both in the (Γ, F) and in the (S, F)-plane. Despite the fact that we have left the mild fluidization regime behind, Γ still appears to be the governing shaking parameter, since the data for the different amplitudes ($a = 2.0, 3.0, 4.0$ mm) collapse better on a single curve in the (Γ, F) than in the (S, F)-plane. In fact, the critical S-values in the latter plane show a systematic increase for growing amplitude a.

This is in contrast to the observations on the granular Leidenfrost effect in a previous study of smaller aspect ratio [8, 22], see Ch. 3, for $d = 4.0$ mm glass beads in a 2-D container, where the phase transition was shown to be governed

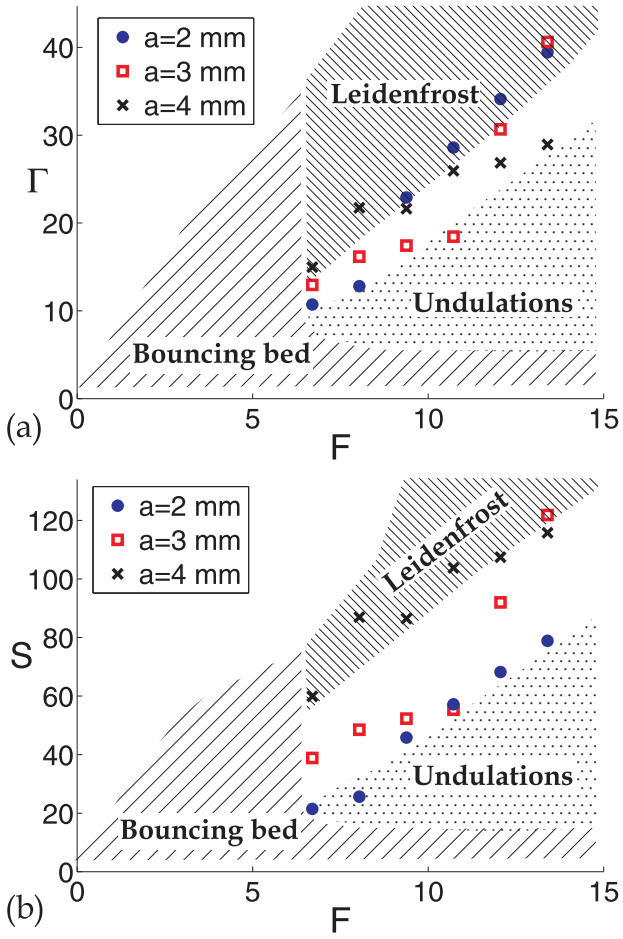

Figure 2.9: The transition from undulations to the granular Leidenfrost effect for increasing frequency f and fixed amplitude $a = 2.0, 3.0, 4.0$ mm: (a) In the (Γ, F)-plane, (b) in the (S, F)-plane. Since in our experiments the Leidenfrost state always originates from the undulation regime, the same minimum number of layers is needed: $F > 6$. The critical values of Γ and S increase with F, since a higher energy input is required to elevate a larger cluster.

by the dimensionless shaking strength S. In that case the Leidenfrost state was reached directly from the solid bouncing bed regime, without the intermediate stage of undulations. Presumably this was due to the much smaller aspect ratio L/h_0, which was on the order of 1 (against $L/h_0 \sim 10$ in the present Leidenfrost

experiments) [23]. Another important difference was that the depth of the setup was just slightly more than one particle diameter (against five diameters in the present setup), so the motion of the granular bed was much more restricted; indeed, the floating cluster in Ref. [8], see Ch. 3, showed a distinctly crystalline packing. It may be concluded, as already remarked in the Sec. 2.1, that the Leidenfrost effect lies in the regime of intermediate fluidization, where both Γ and S are candidates to describe the behavior of the granular bed. The proper choice of the shaking parameter here depends not only on the degree of fluidization, but also on the dimensions of the specific system investigated.

It has been shown that the granular Leidenfrost effect observed in the 2-D container of Ref. [8], see Ch. 3, is successfully explained by a continuum description based on the hydrodynamic equations. The first one is the equation of state,

$$p = nT\frac{n_c + n}{n_c - n}, \quad n_c = \frac{2}{\sqrt{3}d^2}. \tag{2.10}$$

Here p is the pressure, n the number density with n_c the density of a hexagonal close packing, and T the granular temperature. The second equation is the force balance,

$$\frac{dp}{dy} = -mgn, \tag{2.11}$$

where m is the mass of a single particle and g the gravitational acceleration. Finally we have the energy balance:

$$\frac{d}{dy}\left(\kappa\frac{dT}{dy}\right) = \frac{C_1}{\ell}\varepsilon n T^{3/2}, \tag{2.12}$$

in which κ is the thermal conductivity, ℓ the mean free path, $\varepsilon = (1 - e^2)$ the inelasticity parameter, and C_1 is a constant.

The model described by Eqs. (2.10)-(2.12) is closed by three boundary conditions: (1) A prescribed granular temperature at the bottom $T_0 = const$, (2) a vanishing energy flux $[\kappa(y)\frac{dT}{dy} = 0]$ at the top of the system, and (3) the conservation of particles $\int_0^\infty n(y)dy = Fn_c\, d$. In Ref. [8], see Ch. 3, this set of equations plus boundary conditions is solved numerically and the resulting density profiles agree quantitatively with the experimental profiles. Thus, the experimental results are successfully captured by the hydrodynamic model.

2.5 Convection rolls

In our experiments, granular convection rolls are formed at high fluidization from either (a) the bouncing bed (for $3 < F \leqslant 6$ layers) or (b) the granular Leidenfrost effect (for $F > 6$). In both cases the onset of convection is caused by a set of particles in the cluster that are more mobile (higher granular temperature) than the

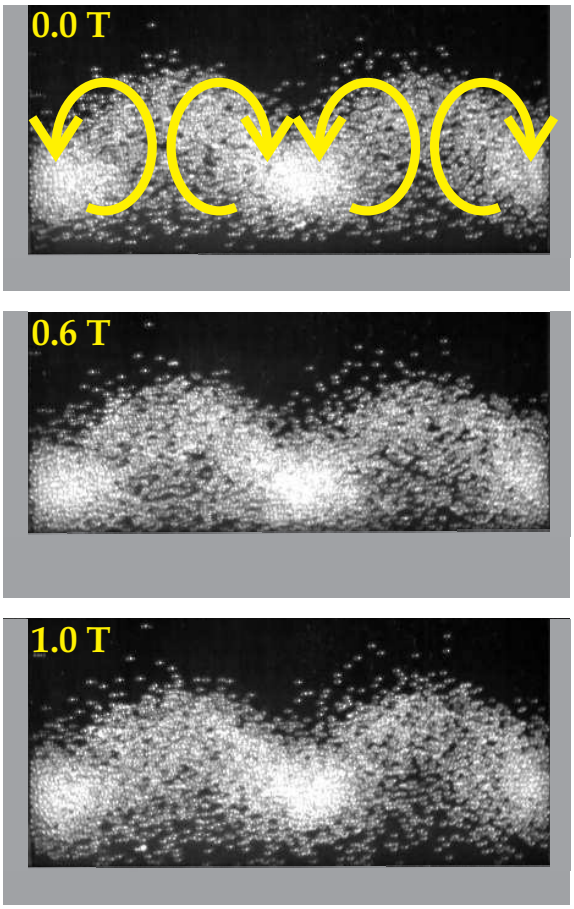

Figure 2.10: Granular convection for $F = 8.1$ layers at $f = 73.0$ Hz and $a = 3.0$ mm (dimensionless shaking strength $S = 193$), showing four counter-rotating rolls. The beads move up in the dilute regions (high granular temperature) and are sprayed sideways to the three dense clusters (low granular temperature). In our system two clusters are always located near the sidewalls, which have a relatively low granular temperature due to the extra dissipation.

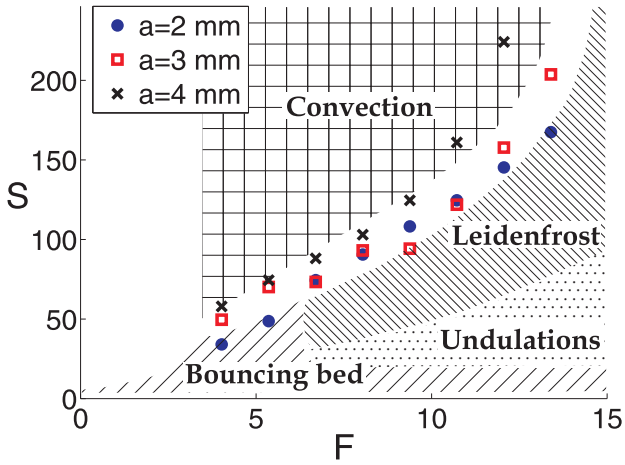

Figure 2.11: The transition towards granular convection from the bouncing bed ($3 < F \leqslant 6$) and the Leidenfrost state ($F > 6$) in the (S,F)-plane, for fixed shaking amplitude $a = 2.0, 3.0$ and 4.0 mm. Just as for the Leidenfrost transition, the convection sets in at higher values of S as the number of layers F is increased, because a higher dissipation must be overcome for larger bed heights.

surrounding area, creating an opening in the bed. These particles have picked up an excess of energy from the vibrating bottom (due to a statistical fluctuation) and collectively move upwards, very much like the onset of Rayleigh-Bénard convection in a classical fluid heated from below [10, 24]. This upward motion of the highly mobile beads must be balanced by a downward movement of neighboring particles, leading to the formation of a convection roll.

The downward motion is most easily accomplished at the sidewalls, due to the extra source of dissipation (i.e., the friction with the walls), and for this reason the first convection roll is always initiated near one of the two sidewalls. Within a second, this first roll triggers the formation of rolls throughout the entire length of the container, leading to a fully developed convection pattern as in Fig. 2.10.

The convection rolls of Fig. 2.10 are fundamentally different from the rolls reported in the literature: Extensive research has been done on granular convection experimentally [25–35], numerically [36–46], and theoretically [47–51]. All studies deal with a *mild* fluidization (typically $\Gamma < 10$) for which the convection is principally boundary-driven and with a nearly constant density in the system. The convection observed here, however, occurs at *strong* fluidization and the

rolls show large density differences; i.e., we report of buoyancy-driven convection rather than boundary-driven which is therefore distinctly different. We are aware of only one numerical study, by Paolotti *et al.* [11], showing the same kind of rolls with large density gradients, and we here present the first experimental observations. In the numerical model by Paolotti *et al.* the container walls were taken to be perfectly elastic, leading to convection patterns in which the rolls were either moving up or down along the sidewalls, whereas in our system (with dissipative walls) they always move down.

To theoretically describe this buoyancy-driven convection we have expanded the 1-D hydrodynamic model of the granular Leidenfrost effect (see Sec. 2.4) to a 2-D model, similar to the approach by Khain and Meerson [50]. The set of equations is linearized around the solution for the granular Leidenfrost state and a stability analysis then yields the point at which the Leidenfrost state gives way to convection rolls. The analysis will be discussed in detail in Chapter 4.

Figure 2.11 shows the transition to convection in the (S,F)-plane, starting from either the bouncing bed or the Leidenfrost state, which are taken together because the transition dynamics is the same in both cases. This is the first instance in which the data points (acquired for all shaking amplitudes: $a = 2.0,\ 3.0$, and 4.0 mm) collapse better for the shaking parameter S than for the dimensionless acceleration Γ, meaning that S is the preferred control parameter for the convection transition.

The onset values of S grow with the number of layers F, because for large F more energy input from the vibrating bottom is necessary to break through the larger dissipation in the granular bed and trigger the first convection roll. Related to this, the number of rolls in the convection pattern decreases for growing F: Due

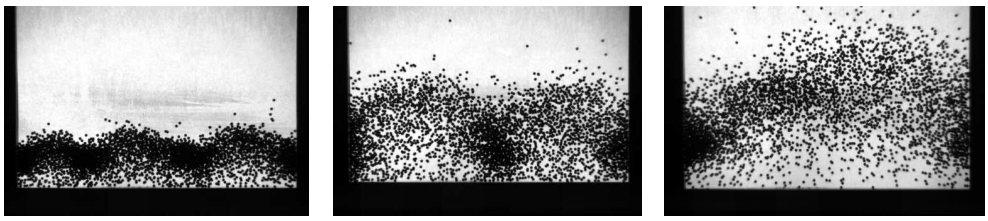

Figure 2.12: Convection patterns for $F = 6.2$ layers of 1.0 mm stainless steel beads at three consecutive shaking strengths: $S = 58$ ($a = 2.0$ mm, $f = 60.0$ Hz), $S = 130$ ($a = 3.0$ mm, $f = 60.0$ Hz), and $S = 202$ ($a = 4.0$ mm, $f = 56.0$ Hz). For increasing S the convection rolls expand, hence a smaller number of them fits into the container. The steel beads behave qualitatively the same as the glass beads used in the rest of the paper.

to the larger total dissipation, the dense clusters of each roll grow in size. Hence, the convection rolls become wider, meaning that less rolls fit into the container.

When, for a given number of layers F, the shaking strength S is increased (either via the frequency f or the amplitude a), the number of rolls in the convection pattern becomes smaller. This is illustrated in Fig. 2.12: The higher energy input induces expansion of the convection rolls, and the number of rolls decreases stepwise as S is increased. The steps involve two rolls at a time, since the pattern always contains an even number of rolls due to the downward motion imposed by the sidewalls.

2.6 Granular gas

In this section we briefly discuss the fifth and last phenomenon observed in our system: A granular gas, being a dilute cloud of particles moving randomly throughout the container as in Fig. 2.13. This state has also been seen in various other experimental systems and is well described by hydrodynamic-like models found in the literature [52, 53]. In fact, one can use the same continuum description as for the granular Leidenfrost effect (Sec. 2.4): For a granular gas, the equation of state of Eq. (2.10) simplifies to the ideal gas law $p = nT$, since the density in a gas is always smaller than the critical number density ($n \ll n_c$). The force balance of Eq. (2.11) remains the same for a gas and in the energy balance of Eq. (2.12) the thermal conductivity κ is no longer a function of the height, but a constant. This set of equations is accompanied by boundary conditions and forms a model that accurately describes the experimental observations.

In our setup the gas state is observed only for a small number of layers ($F \leqslant 3$) and always originates from the bouncing bed regime. At these small F, the bed shows expansion and compaction during every vibration cycle due to the low total dissipation. At the critical value of the shaking parameter, the bed expands to such an extent that it evaporates and forms a gas.

The evaporation of the bouncing bed requires more energy as the number of layers F increases. The transition seems to be controlled by the shaking acceleration Γ (which also governs the transition from solid to bouncing bed) rather than the shaking strength S. However, the data points available are too few ($F \leqslant 3$) to make this conclusive. The measurements will be presented in the full phase diagram of the next section.

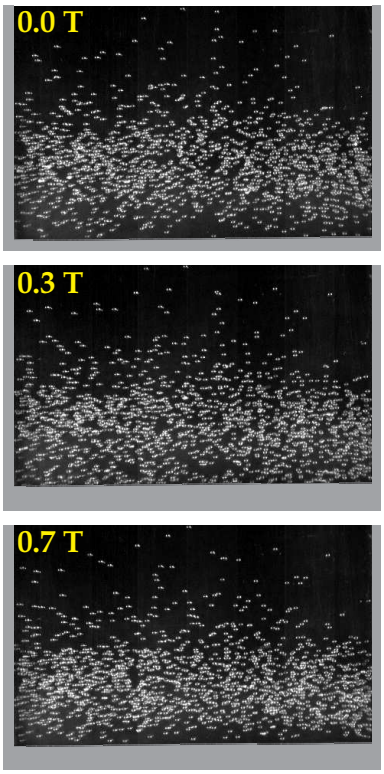

Figure 2.13: Granular gas for $F = 2.7$ layers at $f = 50.0$ Hz and $a = 3.0$ mm ($\Gamma = 30$), which has originated from a bouncing bed by increasing the shaking beyond a critical level [see Fig. 2.14(b)]. With the vibration power available in our system, granular gases are only observed for $F \leqslant 3$ layers.

2.7 Phase diagram

Finally, all the phenomena and associated transitions described in the previous sections are combined in the phase diagram of Fig. 2.14. Both shaking parameters (Γ and S) are used in this diagram, each of them indicating the respective transitions they were found to govern. The parameter Γ is shown along the left vertical axis and the corresponding data points (the critical Γ values) are colored red. The parameter S is plotted along the right vertical axis and the corresponding experimental data are colored blue; this concerns only the "+" signs at the convection transition [54]. For comparison, the Γ-axis is kept the same in all three phase diagrams.

Figure 2.14 contains three separate phase diagrams for the three fixed shaking

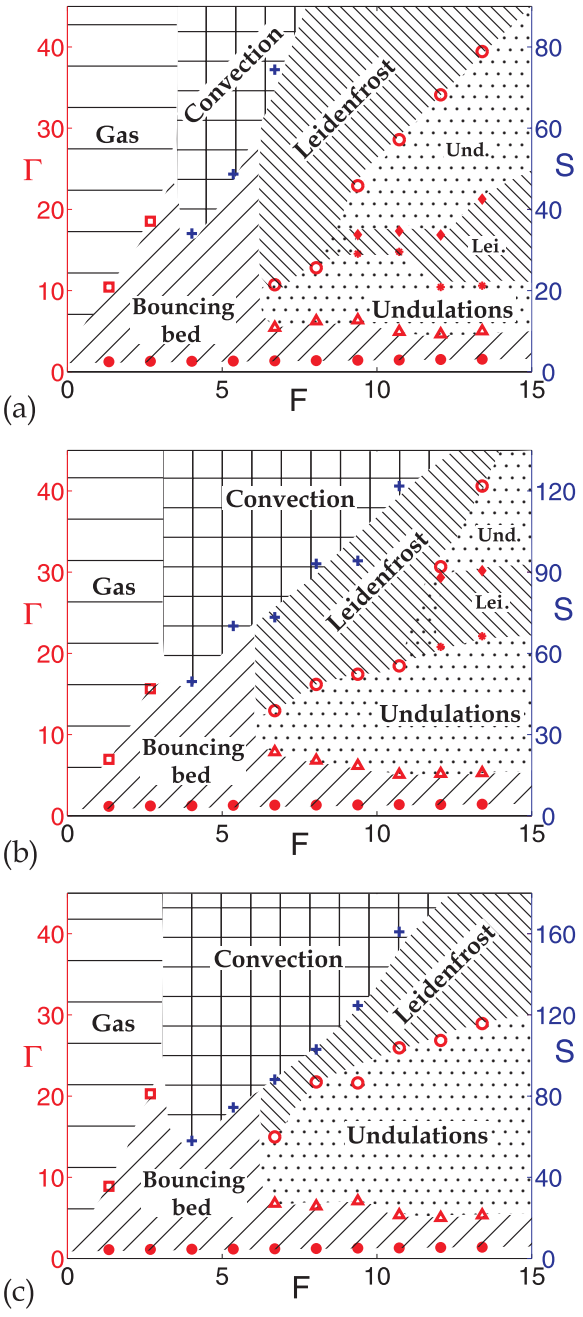

Figure 2.14: Phase diagram of the shallow granular bed at three fixed values of the shaking amplitude: (a) $a = 2.0$ mm, (b) $a = 3.0$ mm, and (c) $a = 4.0$ mm. The five phenomena explored in this paper are indicated by the different shadings. The onset values for bouncing bed, undulations, Leidenfrost effect, and gas are governed by the shaking parameter Γ (left vertical axis, in red); the onset of convection is controlled by S (right vertical axis, in blue). The narrow region without shading along the horizontal F-axis (below the bouncing bed regime) corresponds to the solid phase, in which the bed never detaches from the vibrating bottom.

amplitudes we have used throughout the paper: $a = 2.0$, 3.0, and 4.0 mm. Most of the phase transitions are hardly affected, with the exception of the various transitions between the undulations and the Leidenfrost state. These transitions lie in the regime of *intermediate* fluidization, where the system experiences a competition of length scales: the amplitude a, the particle diameter d, and additionally the wavelength of the undulations λ. This becomes especially clear in the phase diagram of Fig. 2.14(a) for $a = 2.0$ mm where the competition results in an alternation of states. By increasing a, in Figs. 2.14(b) and 2.14(c) it becomes the dominant length scale and the alternation vanishes ultimately.

How does Fig. 2.14 compare with other phase diagrams for shaken granular matter in the literature?

First we discuss the experimental phase diagram by Wassgren *et al.* [20] for a bed of 1.28 mm glass beads at mild fluidization ($\Gamma \leq 10$). For increasing Γ, they observe a series of transitions from a solid bed to undulations ("arching") in qualitative agreement with our own experiments at mild shaking. Their series of transitions is interlaced however with several phenomena (Faraday heaping, surface waves) that are not observed in our system. This is presumably due to the larger depth of their container (12.5 particle diameters, versus 5 in our container, which means that their setup deviates considerably from 2-D) and to the fact that their bed height was typically an order of magnitude larger than ours: The lowest aspect ratio L/h_0 in their experiments was 2, versus 10 in our system. Hsiau and Pan [21], who conducted experiments in a similar setup in the mild fluidization regime, found the same sequence of phenomena as Wassgren *et al.* [20]. Indeed, in three dimensions a much wider variety of phenomena is observed than in 2-D systems, both in experiment [4, 5, 55–68] and in numerics [69–74], e.g., oscillons, heaping, standing wave patterns like squares, stripes, hexagons, spirals, $f/2$-waves, $f/4$-waves, as well as phase bubbles and flat surfaces with kinks. We have restricted ourselves to the shaking amplitude range $a = 2.0 - 4.0$ mm, and therefore we do not see oscillons which are only present for large amplitudes in our setup. Heaping is not observed since the role of air on the $d = 1$ mm particles is too small to develop heaps. Furthermore, all the above standing wave patterns are surface phenomena and they are simply not observed because of the quasi 2-D nature of our setup.

Secondly, Sunthar and Kumaran [43] construct a phase diagram (shaking strength vs. number of layers) based on event-driven simulations in a 2-D system with an aspect ratio $L/h_0 \gtrsim 10$, comparable to ours. At low shaking strength, their phase diagram shows a region where the bed is "homogeneous", corresponding to the solid and bouncing bed regimes in our diagram. At higher shaking strength,

they find a granular gas for $F < 5$ and a region of granular convection for $F > 5$. The gaseous region compares well with the gas region in Fig. 2.14. The convection observed by Sunthar and Kumaran, however, occurs at a much milder fluidization than in our system. In contrast to our convection rolls, the density of their rolls is almost constant, indicating that the bed behaves more like a fluid than a gas.

Thirdly, Eshuis *et al.* [8], see Ch. 3, construct an experimental phase diagram (supported by a theoretical model) for a bed of 4 mm glass beads in a 2-D setup. The (S,F)-diagram shows a bouncing solid regime for low shaking strength and a gas region for small F. Between these two phases, for $S \gtrsim 16$ and $F > 8$, the Leidenfrost regime is located. This is qualitatively the same as in Fig. 2.14, without the regions of undulations and granular convection though. The fact that these latter phenomena were absent is probably due to the much smaller aspect ratio ($L/h_0 \sim 1$) and the much stronger confinement to two dimensions, since the depth of the container was just slightly more than one particle diameter.

Finally, Paolotti *et al.* [11] performed a 2-D numerical study of a granular bed with aspect ratio $L/h_0 \approx 8$, focusing on the transition towards convection. Their convection rolls show similar arches and distinct density differences similar to those observed in our experiments. Starting from strong fluidization, for a given number of layers, they observe two transitions as the shaking strength is reduced: First a transition from a non-convective state (presumably a granular gas) to convection, followed by a transition towards a non-convective state again, in which the particles remain localized near the bottom. This latter state is not further specified, but most probably corresponds to a bouncing bed. In the phase diagram of Fig. 2.14 the same sequence is found if one follows a path from the gas regime to the bouncing bed via convection.

The phase diagram of Fig. 2.14 distinguishes various phase transitions, of which some are phase boundaries and some mark gradual changes. Examples of such a gradual change are the transition from a solid to a bouncing bed, the evaporation of the lower regions of the undulations leading to the floating Leidenfrost cluster, and the expansion of the convection rolls towards a granular gas, which will eventually occur if the shaking strength is increased further. The phenomena observed before and after the transition all display the same symmetry. In contrast, the transitions from a bouncing bed to undulations and the breakthrough of convection rolls starting from the granular Leidenfrost effect show a transition to a state with a different symmetry; they mark the solid-liquid and liquid-gas boundary, respectively.

A solid-gas phase boundary is also found for small number of layers $F < 6$, where the bouncing bed expands to either a granular gas or to convection rolls. For

a larger number of layers, the solid-liquid phase boundary between the bouncing bed and undulations discriminates between the non-fluidized and fluidized system. When the system is fluidized a hydrodynamic approach is successful, and as we get to a fully fluidized system, the transition from the Γ-dominated to the S-dominated regime is marked by the liquid-gas phase boundary between the Leidenfrost effect and convection.

In conclusion, we have constructed the experimental phase diagram for a vertically shaken shallow granular bed in a quasi 2-D container, identifying the dimensionless control parameters that govern the various transitions in this diagram. In the present work we have concentrated on Γ and S (the shaking parameters), and the parameter F (number of particle layers), and we have briefly outlined the current theoretical models used to describe the various phenomena. From the discussion above, it may be concluded that the aspect ratio is also an important control parameter, determining, e.g., the set of different phenomena that a given system is able to exhibit.

The diagram of Fig. 2.14 shows the full range of phases that granular matter can display, behaving like a solid, a fluid, or a gas [75–79]. A determination of the dimensionless parameters that govern the transitions between these phases is a crucial step towards a better understanding of the physics of vertically shaken granular matter.

Acknowledgments: We thank Stefan Luding for stimulating discussions.

References

[1] S. Douady, S. Fauve, and C. Laroche, *Subharmonic instabilities and defects in a granular layer under vertical vibrations*, Europhys. Lett. **8**, 621 (1989).

[2] E. Clément, L. Labous, and L. Vanel, *Granular packing under vibration*, Europhys. News **29**, 107 (1998).

[3] O. Sano, *Dilatancy, buckling, and undulations on a vertically vibrating granular layer*, Phys. Rev. E **72**, 051302 (2005).

[4] F. Melo, P. B. Umbanhowar, and H. L. Swinney, *Transition to parametric wave patterns in a vertically oscillated granular layer*, Phys. Rev. Lett. **72**, 172 (1994).

[5] S. J. Moon, M. D. Shattuck, C. Bizon, D. I. Goldman, J. B. Swift, and H. L. Swinney, *Phase bubbles and spatiotemporal chaos in granular patters*, Phys. Rev. E **65**, 011301 (2001).

[6] M. Faraday, *On a peculiar class of acoustical figures; and on certain forms assumed by groups of particles upon vibrating elastic surfaces*, Philos. Trans. R. Soc. London **52**, 299 (1831).

[7] M. C. Cross and P. C. Hohenberg, *Pattern formation outside of equilibrium*, Rev. Mod. Phys. **65**, 851 (1993).

[8] P. Eshuis, K. van der Weele, D. van der Meer, and D. Lohse, *Granular Leidenfrost effect: Experiment and theory of floating particle clusters*, Phys. Rev. Lett. **95**, 258001 (2005).

[9] J. G. Leidenfrost, *De Aquae Communis Nonnullis Qualitatibus Tractatus* (University of Duisburg, Duisburg, Germany, 1756), translated into English in: Int. J. of Heat and Mass Transfer **9**, 1153 (1966).

[10] S. Chandrasekhar, *Hydrodynamic and hydromagnetic stability* (Oxford Univ. Press, Oxford, UK, 1961).

[11] D. Paolotti, A. Barrat, U. M. B. Marconi, and A. Puglisi, *Thermal convection in monodisperse and bidisperse granular gases: A simulations study*, Phys. Rev. E **69**, 061304 (2004).

[12] H. K. Pak and R. P. Behringer, *Surface waves in vertically vibrated granular materials*, Phys. Rev. Lett. **71**, 1832 (1993).

[13] P. J. Holmes, *The dynamics of repeated impacts with a sinusoidally vibrating table*, J. of Sound and Vibration **84**, 173 (1982).

[14] A. Mehta and J. M. Luck, *Novel temporal behavior of a nonlinear dynamical system: The completely inelastic bouncing ball*, Phys. Rev. Lett. **65**, 393 (1990).

[15] H. A. Janssen, *Getreidedruck in Silozellen*, Zeitschrift des Vereins Deutscher Ingenieure **39**, 1045 (1895).

[16] J. Duran, *Sand, Powders and Grains: An Introduction to the Physics of Granular Materials* (Springer-Verlag, New-York, 1999).

[17] B. Thomas, M. O, Mason, Y. A. Liu, and A. M. Squires, *Identifying states in shallow vibrated beds*, Powder Technology **57**, 267 (1989).

[18] A. Ugawa and O. Sano, *Undulations of a thin granular layer induced by vertical vibration*, J. Phys. Soc. Jpn. **72**, 1390 (2003).

[19] K. Kanai, A. Ugawa, and O. Sano, *Experiment on vibration-induced pattern formation of a vertically thin granular layer*, J. Phys. Soc. Jpn. **74**, 1457 (2005).

[20] C. R. Wassgren, C. E. Brennen, and M. L. Hunt, *Vertical vibration of a deep bed of granular material in a container*, J. Appl. Mech. **63**, 712 (1996).

[21] S. S. Hsiau and S. J. Pan, *Motion state transitions in a vibrated granular bed*, Powder Technology **96**, 219 (1998).

[22] P. Eshuis, K. van der Weele, D. van der Meer, and D. Lohse, *The granular Leidenfrost effect*, in *Powders and Grains*, Vol. **2**, 1155 (Balkema Publ., Leiden, The Netherlands, 2005).

[23] In a related 2-D numerical study by Meerson *et al.*, which showed a granular Leidenfrost effect with a strongly crystalline cluster, the aspect ratio was even smaller than 1. See Fig. 1 in B. Meerson, T. Pöschel, and Y. Bromberg. *Close-packed floating clusters: Granular hydrodynamics beyond the freezing point?*, Phys. Rev. Lett. **91**, 024301 (2003).

[24] E. Bodenschatz, W. Pesch, and G. Ahlers, *Recent developments in Rayleigh-Bénard convection*, Annu. Rev. Fluid Mech **32**, 709 (2000).

[25] E. Clément and J. Rajchenbach, *Fluidization of a bidimensional powder*, Europhys. Lett. **16**, 133 (1991).

[26] J. B. Knight, H. M. Jaeger, and S. R. Nagel, *Vibration-induced size separation in granular media: The convection connection*, Phys. Rev. Lett. **70**, 3728 (1993).

[27] E. E. Ehrichs, H. M. Jaeger, G. S. Karczmar, J. B. Knight, V. Y. Kuperman, and S. R. Nagel, *Granular convection observed by magnetic resonance imaging*, Science **267**, 1632 (1995).

[28] K. M. Aoki, T. Akiyama, Y. Maki, and T. Watanabe, *Convective roll patterns in vertically vibrated beds of granules*, Phys. Rev. E **54**, 874 (1996).

[29] J. B. Knight, E. E. Ehrichs, V. Y. Kuperman, J. K. Flint, H. M. Jaeger, and S. R. Nagel, *Experimental study of granular convection*, Phys. Rev. E **54**, 5726 (1996).

[30] S. S. Hsiau and C. H. Chen, *Granular convection cells in a vertical shaker*, Powder Technology **111**, 210 (2000).

[31] R. D. Wildman, J. M. Huntley, and D. J. Parker, *Convection in highly fluidized three-dimensional granular beds*, Phys. Rev. Lett. **86**, 3304 (2001).

[32] A. Garcimartin, D. Maza, J. L. Ilquimiche, and I. Zuriguel, *Convective motion in a vibrated granular layer*, Phys. Rev. E **65**, 031303 (2002).

[33] S. S. Hsiau, P. C. Wang, and C. H. Tai, *Convection cells and segregation in a vibrated granular bed*, AIChE J. **48**, 1430 (2002).

[34] C. H. Tai and S. S. Hsiau, *Dynamics behaviors of powders in a vibrating bed*, Powder Technology **139**, 221 (2004).

[35] G. M. Rodriguez-Linan and Y. Nahmad-Molinari, *Granular convection driven by shearing interial forces*, Phys. Rev. E **73**, 011302 (2006).

[36] J. A. C. Gallas, H. J. Herrmann, and S. Sokolowski, *Convection cells in vibrating granular media*, Phys. Rev. Lett. **69**, 1371 (1992).

[37] Y.-h. Taguchi, *New origin of a convective motion: Elastically induced convection in granular materials*, Phys. Rev. Lett. **69**, 1367 (1992).

[38] S. Luding, E. Clément, A. Blumen, J. Rajchenbach, and J. Duran, *The onset of convection in molecular dynamics simulations of grains*, Phys. Rev. E **50**, R1762 (1994).

[39] M. Bourzutschky and J. Miller, *Granular convection in a vibrated fluid*, Phys. Rev. Lett. **74**, 2216 (1995).

[40] Y. Lan and A. D. Rosato, *Convection related phenomena in granular dynamics simulations of vibrated beds*, Phys. Fluids **9**, 3615 (1997).

[41] K. M. Aoki and T. Akiyama, *Control parameter in granular convection*, Phys. Rev. E **58**, 4629 (1998).

[42] R. Ramírez, D. Risso, and P. Cordero, *Thermal convection in fluidized granular systems*, Phys. Rev. Lett. **85**, 1230 (2000).

[43] P. Sunthar and V. Kumaran, *Characterization of the stationary states of a dilute vibrofluidized granular bed*, Phys. Rev. E **64**, 041303 (2001).

[44] J. Talbot and P. Viot, *Wall-enhanced convection in vibrofluidized granular systems*, Phys. Rev. Lett. **89**, 064301 (2002).

[45] P. Cordero, R. Ramirez, and D. Risso, *Buoyancy driven convectino and hysteresis in granular gases: Numerical solution*, Physica A **327**, 82 (2003).

[46] D. Risso, R. Soto, S. Godoy, and P. Cordero, *Friction and convection in a vertically vibrated granular system*, Phys. Rev. E **72**, 011305 (2005).

[47] H. Hayakawa, S. Yue, and D. C. Hong, *Hydrodynamic description of granular convection*, Phys. Rev. Lett. **75**, 2328 (1995).

[48] X. He, B. Meerson, and G. Doolen, *Hydrodynamics of thermal granular convection*, Phys. Rev. E **65**, 030301 (2002).

[49] T. Ohtsuki and T. Ohsawa, *Hydrodynamics for convection in vibrating beds of cohesionless granular materials*, J. Phys. Soc. Jpn. **72**, 1963 (2003).

[50] E. Khain and B. Meerson, *Onset of thermal convection in a horizontal layer of granular gas*, Phys. Rev. E **67**, 021306 (2003).

[51] G. Miao, K. Huang, Y. Yun, and R. Wei, *Active thermal convection in vibrofluidized granular systems*, Eur. Phys. J. B **40**, 301 (2004).

[52] J. Eggers, *Sand as Maxwell's demon*, Phys. Rev. Lett. **83**, 5322 (1999).

[53] I. Goldhirsch, *Rapid granular flows*, Annu. Rev. Fluid Mech. **35**, 267 (2003).

[54] To keep the phase diagram well-proportioned, not all data points of the Leidenfrost-convection transition (+) are presented in Fig. 2.14. The full set of data points can be seen in Fig. 2.11.

[55] S. B. Savage, *Streaming motions in a bed of vibrationally fludized dry granular material*, J. Fluid Mech. **194**, 457 (1988).

[56] F. Melo, P. B. Umbanhowar, and H. L. Swinney, *Hexagons, kinks, and disorder in oscillated granular layers*, Phys. Rev. Lett. **75**, 3838 (1995).

[57] T. H. Metcalf, J. B. Knight, and H. M. Jaeger, *Standing wave patterns in shallow beds of vibrated granular material*, Phys. A **236**, 202 (1997).

[58] C. Bizon, M. D. Shattuck, J. B. Swift, W. D. McCormick, and H. L. Swinney, *Patterns in 3D vertically oscillated granular layers: Simulation and experiment*, Phys. Rev. Lett. **80**, 57 (1998).

[59] N. Mujica and F. Melo, *Solid-liquid transition and hydrodynamic surface waves in vibrated granular layers*, Phys. Rev. Lett. **80**, 5121 (1998).

[60] N. Mujica, L. Caballero, and F. Melo, *Collective motion and solid-liquid type transitions in vibrated granular layers*, Phys. A **263**, 362 (1999).

[61] O. Sano, *Random motion of a marker particle on square cells formed on vertically vibrated granular layers*, J. Phys. Soc. Jpn. **68**, 1769 (1999).

[62] P. B. Umbanhowar and H. L. Swinney, *Wavelength scaling and square/stripe and grain mobility transitions in vertically oscillated granular layers*, Phys. A **288**, 344 (2000).

[63] D. Blair, I. S. Aranson, G. W. Crabtree, V. Vinokur, L. S. Tsimring, and C. Josserand, *Patterns in thin vibrated granular layers: Interfaces, hexagons, and superoscillons*, Phys. Rev. E **61**, 5600 (2000).

[64] J. M. Hill, M. J. Jennings, D. V. To, and K. A. Williams, *Dynamics of an elastic ball bouncing on an oscillating plane and the oscillon*, Appl. Math. Modelling **24**, 715 (2000).

[65] J. R. de Bruyn, B. C. Lewis, M. D. Shattuck, and H. L. Swinney, *Spiral patterns in oscillated granular layers*, Phys. Rev. E **63**, 041305 (2001).

[66] K. Kim and H. K. Pak, *Coarsening dynamics of striped patterns in thin granular layers under vertical vibration*, Phys. Rev. Lett. **88**, 204303 (2002).

[67] D. I. Goldman, J. B. Swift, and H. L. Swinney, *Noise, coherent fluctuations, and the onset of order in an oscillated granular fluid*, Phys. Rev. Lett. **92**, 174302 (2004).

[68] Y. S. Wong, C. H. Gan, C. H. Wang, X. Fan, D. J. Parker, A. Ingram, and J. P. K. Seville, *Instabilities in vertically vibrated granular beds at the single particle scale*, Phys. Fluids **18**, 043302 (2006).

[69] L. S. Tsimring and I. S. Aranson, *Localized and cellular patterns in a vibrated granular layer*, Phys. Rev. Lett. **79**, 213 (1997).

[70] T. Shinbrot, *Competition between randomizing impacts and inelastic collisions in granular pattern formation*, Nature **389**, 574 (1997).

[71] I. S. Aranson, L. S. Tsimring, and V. M. Vinokur, *Hexagons and interfaces in a vibrated granular layer*, Phys. Rev. E **59**, R1327 (1999).

[72] H. K. Park and H. T. Moon, *Square to stripe transition and superlattice patterns in vertically oscillated granular layers*, Phys. Rev. E **65**, 051310 (2002).

[73] S. J. Moon, J. B. Swift, and H. L. Swinney, *Role of friction in pattern formation in oscillated granular layers*, Phys. Rev. E **69**, 031301 (2004).

[74] J. Bougie, J. Kreft, J. B. Swift, and H. L. Swinney, *Onset of patterns in an oscillated granular layer: Continuum and molecular dynamics simulations*, Phys. Rev. E **71**, 021301 (2005).

[75] H. M. Jaeger and S. R. Nagel, *Physics of the granular state*, Science **255**, 1523 (1992).

[76] H. M. Jaeger, S. R. Nagel, and R. P. Behringer, *Granular solids, liquids, and gases*, Rev. Mod. Phys. **68**, 1259 (1996).

[77] A. J. Liu and S. R. Nagel, *Jamming is not just cool any more*, Nature **396**, 21 (1998).

[78] L. P. Kadanoff, *Built upon sand: Theoretical ideas inspired by granular flows*, Rev. Mod. Phys. **71**, 435 (1999).

[79] I. S. Aranson and L. S. Tsimring, *Patterns and collective behavior in granular media: Theoretical concepts*, Rev. Mod. Phys. **78**, 641 (2006).

3

Granular Leidenfrost effect: Experiment and theory of floating particle clusters

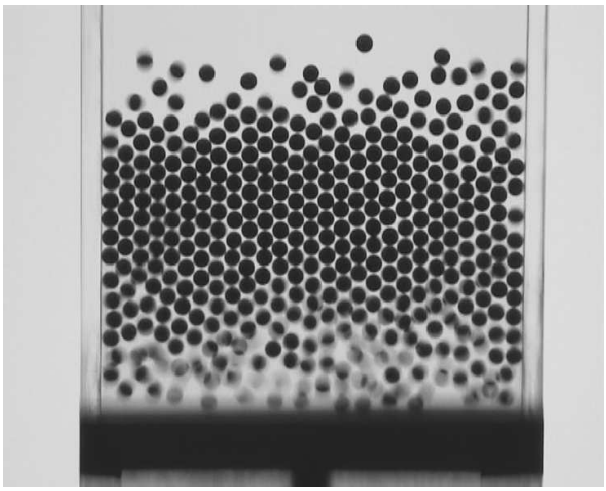

Peter Eshuis, Ko van der Weele, Devaraj van der Meer, and Detlef Lohse, *Physical Review Letters* **95**, 258001 (2005).

Granular material is vertically vibrated in a 2-D container: Above a critical shaking strength, and for a sufficient number of beads, a crystalline cluster is elevated and supported by a dilute gaseous layer of fast beads underneath. We call this phenomenon the granular Leidenfrost effect. The experimental observations are explained by a hydrodynamic model featuring three dimensionless control parameters: The energy input S, the number of particle layers F, and the inelasticity of the particle collisions ε. The (S,F)-phase diagram, in which the Leidenfrost state lies between the purely solid and gas phases, shows accurate agreement between experiment and theory.

3.1 Introduction

Vertically shaken granular matter typically exhibits a region of reduced density just above the vibrating bottom [1–5]. An exceptionally strong form of this so-called density inversion was recently encountered in a theoretical study by Meerson *et al.* [6]: For sufficiently strong shaking a dense cluster of particles, showing a hexagonal packing, was observed to be elevated and supported by a dilute layer of fast particles underneath.

Here we present the first *experimental* observation of this phenomenon, which we will call the granular Leidenfrost effect. It is analogous to the original Leidenfrost effect of a water droplet hovering over a hot plate [7–9]: When the temperature of the plate exceeds the Leidenfrost temperature $T_L \approx 220\,^{\circ}\mathrm{C}$ (equivalent to the critical shaking strength in the granular system), the bottom layer of the drop vaporizes instantly and prevents direct heat transfer from the plate to the drop, causing the droplet to hover and survive for a long time [8].

We also give a *theoretical* explanation in the spirit of Meerson *et al.* [6, 10, 11]. These authors focused on the point where the density at the bottom first becomes inverted, which is a precursor to the granular Leidenfrost effect (not yet the actual phase separation). We study the subsequent transition from this density-inverted state to the Leidenfrost state in which the solid and gas phases co-exist. A major challenge in granular research today is to achieve a hydrodynamic-like continuum description [12–17], which, however, in many cases breaks down due to the tendency of the particles to cluster together [18, 19]. We show that the Leidenfrost effect (despite the clustered phase) is well described by a hydrodynamic model.

3.2 Experimental results

Our experimental setup (Fig. 3.1) consists of a quasi-2D container ($10 \times 0.45 \times 14$ cm) [20] filled with glass beads of diameter $d = 4.0$ mm, density $\rho = 2600$ kg/m^3, and coefficient of normal restitution $e \approx 0.95$. The setup is mounted on a shaker with tunable frequency f and amplitude a. The Leidenfrost effect, see Fig. 3.1, is stably reproduced for given, sufficiently large values of the shaking strength and the number of particle layers.

The four natural dimensionless control parameters to analyze the experiment are (i) the shaking acceleration (with g the gravitational acceleration):

$$\Gamma = \frac{a(2\pi f)^2}{g}, \tag{3.1}$$

(ii) the number of bead layers F, (iii) the dimensionless shaking amplitude $A = a/d$, and (iv) the inelasticity parameter $\varepsilon = (1 - e^2)$.

First the dependence on Γ is investigated for a fixed number of layers $F = 16$. Figures 3.2(a) and 3.2(b) show an experimental snapshot and the corresponding density profile $n(y)$ (determined by counting the number of black pixels in each horizontal row) at moderate shaking, $\Gamma = 7.7$. The snapshot shows a hexagonal packing and this is reflected in the periodic structure of $n(y)$; i.e., the particles behave like a solid crystal. The theoretical profile in Fig. 3.2(c) does not show this periodicity, reflecting the continuum (non-particulate) character of the model.

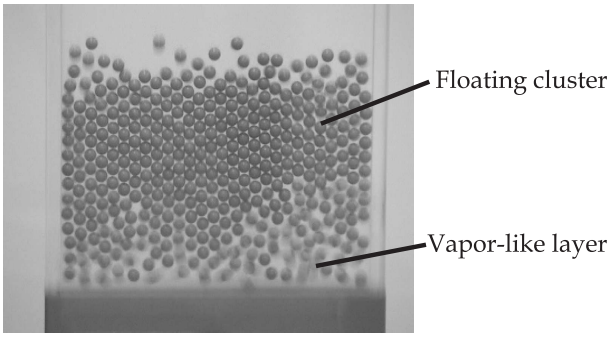

Figure 3.1: Granular Leidenfrost effect: Glass beads, vertically vibrated above a critical shaking strength, form a crystalline cluster that is elevated and supported by a vapor-like layer of fast particles underneath. The thickness of the dilute layer oscillates in time (never vanishing) due to the motion of the bottom, while the cluster floats steadily at the same position.

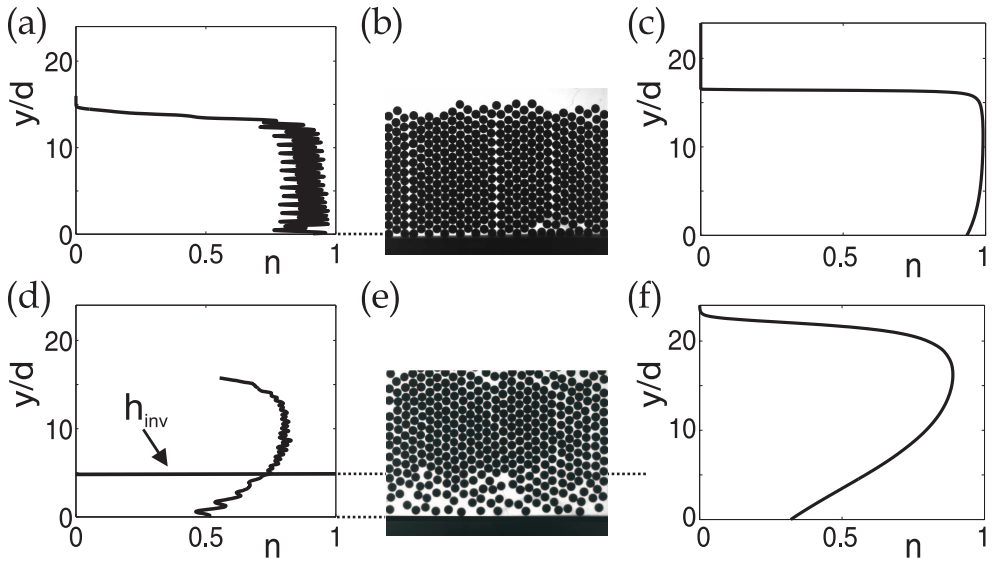

Figure 3.2: (a) Density profile, averaged over 300 consecutive snapshots, as a function of height for $F = 16$ layers at shaking strength $\Gamma = 7.7$ ($a = 0.3$ mm, $f = 80$ Hz). The origin $y/d = 0$ is set at the maximal positive displacement of the vibrating bottom. (b) A typical snapshot of this experiment recorded by a high-speed camera (1000 fps) and (c) the theoretical profile from the model in Eqs. (3.4)-(3.6) with $S = 0.58$. (d) Density profile for $F = 16$ layers at $\Gamma = 51.5$ ($a = 2.0$ mm, $f = 80$ Hz), showing the Leidenfrost state. The inversion height h_{inv} marks the border between the gaseous and the solid phase; it is determined via the method illustrated in Fig. 3.3. (e) The corresponding experimental snapshot and (f) the theoretical profile for $S = 25.76$.

At vigorous shaking [Figs. 3.2(d) and 3.2(e)] the Leidenfrost state is observed: A crystalline cluster floats on top of a dilute gaseous layer. The particular experiment of Fig. 3.2(e) was performed at $\Gamma = 51.5$, well above the critical shaking strength ($\Gamma_c \approx 25$ for $F = 16$ layers) at which the Leidenfrost effect sets in. Increasing the shaking strength even more causes the crystalline layer to become thinner and more dilute, until (at some very high value of Γ, beyond the capacity of our shaker) it will disappear altogether and the whole system becomes gaseous.

Regarding the dependence on the second control parameter (F), a Leidenfrost state only occurs for $F \gtrsim 8$ particle layers. For smaller F one witnesses a direct transition from the solid phase to a pure granular gas.

3.3 Order parameter

Now, what is a suitable order parameter to distinguish between the gaseous and the crystalline phase in the Leidenfrost state? To answer this, we turn to the pair correlations of the particles in a horizontal strip $(y, y+dy)$ (where dy is chosen to be equal to a particle diameter):

$$g_y(x) = \frac{1}{N} \sum_{i,j\,in\,(y,y+dy)} \sum_{i \neq j} \delta(x - (x_i - x_j)), \tag{3.2}$$

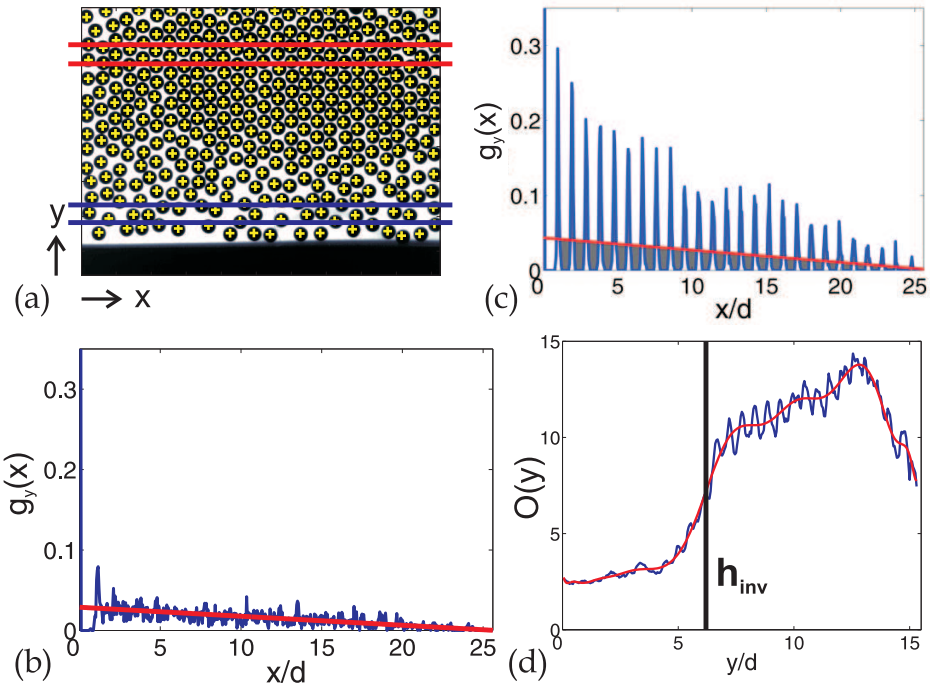

Figure 3.3: (a) Experimental Leidenfrost state for $\Gamma = 64.4$ ($a = 2.5$ mm, $f = 80$ Hz), with $F = 16$ layers: Two horizontal strips have been selected, one in the gaseous layer and one in the crystalline region. (b) The correlation $g_y(x)$ between the particle centers (+) in the gaseous strip, determined via Eq. (3.2). (c) The same in the crystalline strip, showing a clear periodicity. The shaded area is the order parameter O. (d) $O(y)$ (in arbitrary area units), determined for a number of strips at different heights. The smoothed fit through $O(y)$ is used to determine the inversion height h_{inv}, marking the transition from gas to crystal.

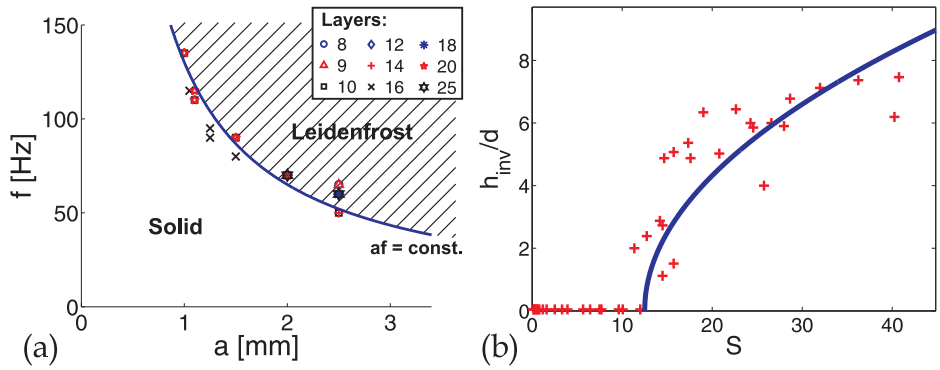

Figure 3.4: (a) The critical values of the shaking amplitude a and frequency f at which the transition from the solid to the Leidenfrost state occurs, for a number of experiments with $F = 8,..,25$ layers. The product af is constant along the transition curve, or equivalently, $S \equiv \Gamma A \propto (af)^2$ is constant. (b) The inversion height h_{inv} vs. the shaking parameter S for $F = 16$ layers, indicating that the transition is a continuous, second-order phase transition. The fit through the experimental data is of the form $h_{inv}/d \propto (S - S_{onset})^{1/2}$.

with N the number of particles in the strip, and $x_{i,j}$ their horizontal positions. Figure 3.3(b) gives $g_y(x)$ for a typical gas-like strip near the bottom, where the particle positions show hardly any correlation. On the other hand, the strip inside the floating cluster of Fig. 3.3(c) shows a strong periodic, crystalline correlation. This clear distinction between periodic and non-periodic behavior is exploited in the order parameter O, which we define as the modulus of the integrated difference between $g_y(x)$ and its running mean: O is the shaded area in Figs. 3.3(b) and 3.3(c). Figure 3.3(d) shows O as a function of height y, exhibiting a clear transition from the gas-like to the crystalline phase. By making a fit through $O(y)$ in which we smoothen out the oscillations associated with the crystalline order, the inversion height h_{inv} can be determined as the point where the slope of the fit is maximal [see Fig. 3.3(d)].

For all experimental runs, we determined from the associated order parameter plots [as in Fig. 3.3(d)] the critical shaking amplitude a and frequency f at the transition to the Leidenfrost state, i.e., when the inversion height becomes nonzero for the first time. The result is plotted in Fig. 3.4. Along the curve in the (a, f)-plane that marks the transition towards the Leidenfrost state [Fig. 3.4(a)],

the product af is constant, or equivalently:

$$S \equiv \Gamma A = \frac{(a2\pi f)^2}{gd} \tag{3.3}$$

is constant at the transition. So S (and not Γ) is the fundamental shaking parameter in the experiments. We will see later that this is not only true in our experiments, but also in the theoretical model.

Therefore, in Fig. 3.5 we present the location of the Leidenfrost regime, marked by crosses ($\times$), in the (S,F)-plane and not the (Γ,F)-plane. The transition from the solid phase ($\bullet$) to the Leidenfrost regime occurs along a nearly horizontal line, i.e., constant S, in agreement with the result from Fig. 3.4. Increasing the shaking strength further, the Leidenfrost state disappears again and the system now behaves as a pure gas ($\circ$). In experiment, this last transition can only be observed around the critical number of $F \approx 8$ layers; the transition line rises so steeply that for more layers our shaker is not strong enough to vaporize the Leidenfrost state.

3.4 Hydrodynamic model

To explain the experimental observations theoretically, we use a continuum description of the granular material. It is to be regarded as a minimal model (disregarding the effect of the side walls, which makes it essentially one-dimensional, and sidestepping the particle nature of the system), not intended to capture all the details of the experimental system, but to explain the granular Leidenfrost effect. The model is based on three hydrodynamic equations that have been derived within the context of the kinetic theory of granular gases [6, 13, 14, 16].

The first one is the standard force balance:

$$\frac{dp}{dy} = -mgn, \tag{3.4}$$

with $p(y)$ the pressure, m the mass of a single particle, and $n(y)$ the number density.

The second equation is the energy balance between the heat flux through the vibrated bed and the dissipation due to the inelastic particle collisions:

$$\frac{d}{dy}\left\{\kappa\frac{dT}{dy} + C_1\varepsilon l T^{3/2}\frac{dn}{dy}\right\} = \frac{\mu}{\gamma l}\varepsilon n T^{3/2}. \tag{3.5}$$

On the left-hand side, the thermal conductivity κ is proportional to the product of the density n, average particle velocity ($\propto T^{1/2}$, with T the granular temperature), and the mean free path l: $\kappa \propto nT^{1/2}l$ [14]. The second term on the left-hand side only becomes important when the density gradient dn/dy is large [15]. The term on the right is equal to the energy loss in one collision ($\propto \varepsilon T$) multiplied by the total number of collisions ($\propto nT^{1/2}$) [6]. The coefficients C_1, μ, and γ are constants.

Thirdly, we have the equation of state [14, 21]:

$$p = nT\frac{n_c + n}{n_c - n}, \tag{3.6}$$

which is the ideal-gas law ($p = nT$) corrected for excluded volume effects, with $n_c = 2/\sqrt{3}d^2$ being the number density of the close-packed hexagonal crystal. Equation (3.6) is an interpolation between the well-established equations of state in the low and high density limit [14, 21, 22].

The three equations (3.4)-(3.6) are supplemented by three boundary conditions. The first one states that the granular temperature at the bottom of the container is constant: $T_0 = \text{const}$. The second condition is that the energy flux must be zero at the top of the system: $\lim_{y\to\infty}[\kappa(y)dT/dy] = 0$, and the third condition is the conservation of particles: $\int_0^\infty n(y)\,dy = F\,n_c\,d$.

The above set of equations plus boundary conditions can be solved numerically, using a shooting method for the vanishing heat flux at infinity (second condition). Two typical examples of the resulting density profiles are shown in Figs. 3.2(c) and 3.2(f). They agree qualitatively with the experimental profiles, apart from the oscillations associated with the particle packing, which of course do not show up in the continuum approach. In all cases we encountered, the term proportional to dn/dy in the energy balance (3.5) proved to be negligible compared to the dT/dy term. So for our system Eq. (3.5) simplifies to:

$$\frac{d}{dy}\left\{\kappa\frac{dT}{dy}\right\} = \frac{\mu}{\gamma l}\varepsilon n T^{3/2}. \tag{3.7}$$

The equations (3.4), (3.6), and (3.7), plus boundary conditions, can be nondimensionalized by introducing the variables $\tilde{y} = y/d$, $\tilde{n} = n/n_c$, and $\tilde{T} = T/T_0$. Then the following dimensionless control parameter show up in the new set of equations and conditions: The number of layers F, the inelasticity $\varepsilon = (1 - e^2)$, and the energy input S defined in Eq. (3.3), just as in the experiment. Thus, from the four dimensionless control parameters identified originally [see Eq. (3.1) and

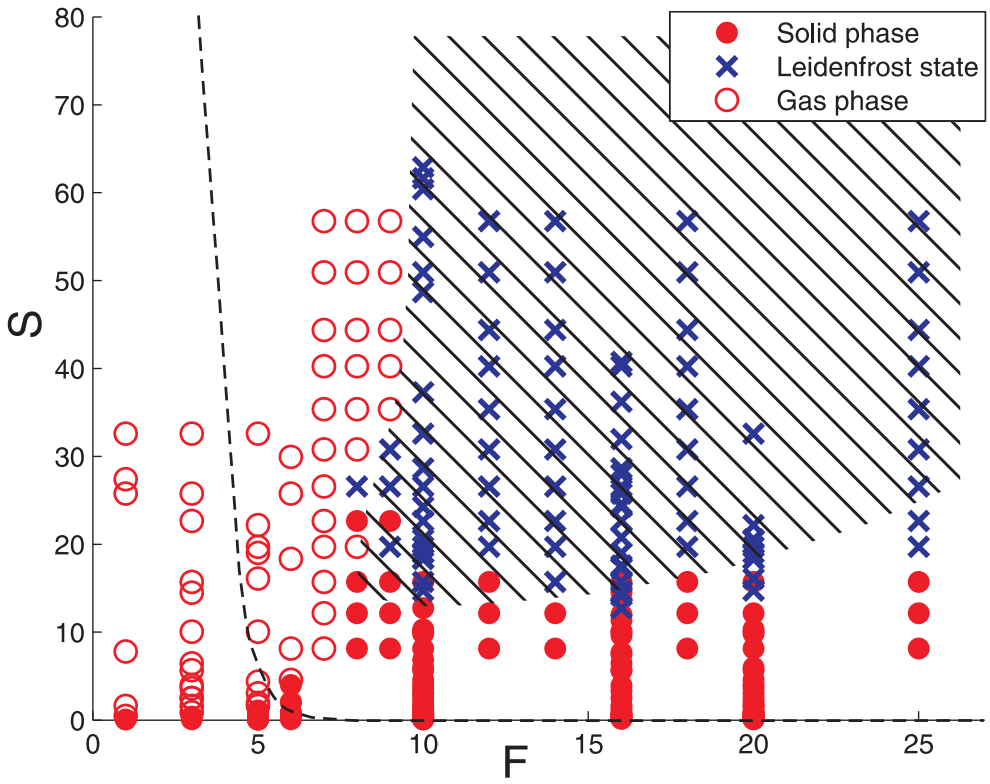

Figure 3.5: Phase diagram of F (number of layers) vs. S (shaking strength), with the Leidenfrost state showing up between the regions of solid and gas-like behavior. The symbols represent experimental data: solid phase (•), gas phase (○), and Leidenfrost state (×). The shaded area is the Leidenfrost regime according to our hydrodynamic theory. The dashed curve marks the onset of density inversion at the bottom, $dn/dy\,|_{y=0}= 0$, an essential precursor to the Leidenfrost effect.

below], only *three* remain because Γ and the dimensionless shaking amplitude A do not appear individually in the model, but only combined as $S \equiv \Gamma A$ [23].

The parameter S is proportional to the typical kinetic energy of the particles at the bottom [$\propto \frac{1}{2}m(af)^2$] divided by the potential energy needed for a particle to overcome its own diameter [mgd].

To extract the theoretical Leidenfrost regime in the (S,F)-plane (the shaded area in Fig. 3.5) we proceed as follows from the calculated density profiles [24]: The *onset* of the Leidenfrost effect from the solid state is taken to occur when a layer of at least 2 particle diameters near the bottom drops below the density threshold $n_1 = 0.5n_c$. When S is increased beyond its critical value $S_{onset} \approx 16$,

the crystalline as well as the gas-like phase gradually become more dilute. The *breakdown* of the Leidenfrost state, where it gives way to a pure gas, is taken to occur when the part of the profile exceeding $n_1 = 0.5n_c$ becomes less than 6 particle diameters thick. This upper boundary rises very steeply, e.g., at $F = 16$ layers $S_{breakdown} \approx 2000$ [25].

The required minimum thicknesses of the gaseous and the crystalline phase (2 respective 6 particle diameters) agree with the experimentally observed thicknesses in our snapshots. The parameter n_1 also reasonably agrees with the snapshots; its precise value is chosen such as to yield an optimal overlap between the experimental and theoretical Leidenfrost regimes in Fig. 3.5.

In Fig. 3.5 we have also included the dashed curve where $dn/dy\,|_{y=0}$ goes through zero, i.e., the onset of the density inversion studied earlier by Meerson *et al.* [6]. Above this curve $dn/dy\,|_{y=0}$ is positive, which paves the way for the Leidenfrost effect, but in itself does not mark a phase transition yet. Physically, the granular material is still fully either a gas or a solid at the dashed line [as can be verified via the order parameter $O(y)$].

3.5 Conclusion

In conclusion, the granular Leidenfrost effect has been demonstrated experimentally for the first time, in a 2-D setup: When the shaking strength S exceeds a critical value, and for sufficiently many particle layers, a dense cluster with a hexagonal packing floats on top of a gaseous region. The two co-existing phases in this hybrid state (solid and gas) can be distinguished from each other by their difference in crystalline order, through the order parameter $O(y)$. The experimental observations are quantitatively explained by our hydrodynamic model, as shown by the density profiles in Fig. 3.2 and the (S,F)-diagram of Fig. 3.5.

Acknowledgments: We thank I. Goldhirsch, B. Meerson, and T. Pöschel for stimulating discussions, and M. Sandtke for setting up the first experiment.

References

[1] Y. Lan and A. D. Rosato, *Macroscopic behavior of vibrating beds of smooth inelastic spheres*, Phys. Fluids **7**, 1818 (1995).

[2] A. Kudrolli, M. Wolpert, and J.P. Gollub, *Cluster Formation due to Collisions in Granular Material*, Phys. Rev. Lett. **78**, 1383 (1997).

[3] R.D. Wildman, J.M. Huntley, and J.-P. Hansen, in *Granular Gases* pp. 215-232 (Springer, Berlin, 2001).

[4] J.J. Brey, M.J. Ruiz-Montero, and F. Moreno, *Hydrodynamics of an open vibrated granular system*, Phys. Rev. E **63**, 061305 (2001).

[5] C. Huan, X. Yang, D. Candela, R. W. Mair, and R. L. Walsworth, *NMR experiments on a three-dimensional vibrofluidized granular medium*, Phys. Rev. E **69**, 041302 (2004).

[6] B. Meerson, T. Pöschel, and Y. Bromberg, *Close-packed floating clusters: Granular hydrodynamics beyond the freezing point?*, Phys. Rev. Lett. **91**, 024301 (2003).

[7] J. G. Leidenfrost, *De Aquae Communis Nonnullis Qualitatibus Tractatus* (University of Duisburg, Duisburg, Germany, 1756), translated into English in: Int. J. of Heat and Mass Transfer **9**, 1153 (1966).

[8] J. Walker, http://www.wiley.com/college/phy/halliday320005/pdf/leidenfrost_essay.pdf; essay accompanying the textbook *Fundamentals of Physics*, D. Halliday, R. Resnick, and J. Walker (6th Ed., Wiley, New York, 2001).

[9] A.-L. Biance, C. Clanet, and D. Quéré, *Leidenfrost drops*, Phys. Fluids **15**, 1632 (2003).

[10] Y. Bromberg, E. Livne, and B. Meerson, *Granular Gas Dynamics*, Lecture Notes in Phys. **624**, 251 (2003).

[11] Preliminary results have been reported in P. Eshuis, K. van der Weele, D. van der Meer, and D. Lohse, *The granular Leidenfrost effect*, in *Powders and Grains*, Vol. **2**, 1155 (Balkema Publ., Leiden, The Netherlands, 2005).

[12] J. T. Jenkins and S. B. Savage, *A theory for the rapid flow of identical, smooth, nearly elastic, spherical particles*, J. Fluid Mech. **130**, 187 (1983); J. T. Jenkins and M. W. Richman, *Boundary conditions for plane flows of smooth, nearly elastic, circular disks*, J. Fluid Mech. **171**, 53 (1986).

[13] P. K. Haff, *Grain flow as a fluid-mechanical phenomenon*, J. Fluid Mech. **134**, 401 (1983).

[14] E. L. Grossman, T. Zhou, and E. Ben-Naim, *Towards Granular Hydrodynamics in Two-Dimensions*, Phys. Rev. E **55**, 4200 (1997).

[15] N. Sela and I. Goldhirsch, *Hydrodynamic equations for rapid flows of smooth inelastic spheres to Burnett order*, J. Fluid Mech. **361**, 41 (1998).

[16] J. Eggers, *Sand as Maxwell's demon*, Phys. Rev. Lett. **83**, 5322 (1999).

[17] I. Goldhirsch, *Rapid granular flows*, Annu. Rev. Fluid Mech. **35**, 297 (2003).

[18] Y. Du, H. Li, and L. P. Kadanoff, *Breakdown of hydrodynamics in a one-dimensional system of inelastic particles*, Phys. Rev. Lett. **74**, 1268 (1995).

[19] L. P. Kadanoff, *Built upon sand: Theoretical ideas inspired by granular flows*, Rev. Mod. Phys. **71**, 435 (1999).

[20] Our container enables a direct comparison with the (2D) results of [6]. The friction from the front and back wall presumably has a slight stabilizing effect on the Leidenfrost state: see J. S. van Zon, J. Kreft, D. I. Goldman, D. Miracle, J. B. Swift, and H. L. Swinney, *Crucial role of sidewalls in velocity distributions in quasi-two-dimensional granular gases*, Phys. Rev. E **70**, 040301 (2004).

[21] O. Herbst, P. Müller, M. Otto, and A. Zippelius, *Local equation of state and velocity distributions of a driven granular gas*, Phys. Rev. E **70**, 051313 (2004).

[22] S. Luding, *Global equation of state of two-dimensional hard sphere systems*, Phys. Rev. E **63**, 042201 (2001).

[23] Various studies during the last decade proposed $(af)^\alpha$ as the appropriate shaking parameter in vibrofluidized granular systems, with α ranging from 1 to 2 depending on the system under consideration [26]. In our system both theory and experiment agree on the value $\alpha = 2$.

[24] The experimental order parameter $O(y)$ cannot be used here, since the pair correlations method is obviously not applicable to the continuum model.

[25] The steep rise of S at the Leidenfrost-gas transition agrees with an observation of B. Bernu, F. Delyon, and R. Mazighi, *Steady states of a column of shaken inelastic beads*, Phys. Rev. E **50**, 4551 (1994), who found that a 1D column of particles becomes very hard to fluidize when εF exceeds a certain threshold value.

[26] S. Warr, G. T. H. Jacques, and J. M. Huntley, *Tracking the translational and rotational motion of granular particles: use of high-speed photography and image processing*, Powder Technol. **81**, 41 (1994). S. Warr, J. M. Huntley, and G. T. H. Jacques, *Fluidization of a two-dimensional granular system: Experimental study and scaling behavior*, Phys. Rev. E **52**, 5583 (1995); S. Luding, H. J. Herrmann,

and A. Blumen, *Scaling behavior of 2-Dimensional arrays of beads under external bibrations*, Phys. Rev. E **50**, 3100 (1994); J. M. Huntley, *Scaling laws for a two-dimensional vibro-fluidized granular material*, Phys. Rev. E **58**, 5168 (1998); V. Kumaran, *Temperature of a granular material "fluidized" by external vibrations* Phys. Rev. E **57**, 5660 (1998); R. D. Wildman and J. M. Huntley, *Scaling exponents for energy transport and dissipation in binary vibro-fluidized granular beds*, Phys. Fluids **15**, 3090 (2003).

4

Buoyancy Driven Convection in Vertically Shaken Granular Matter: Experiment, Numerics, and Theory

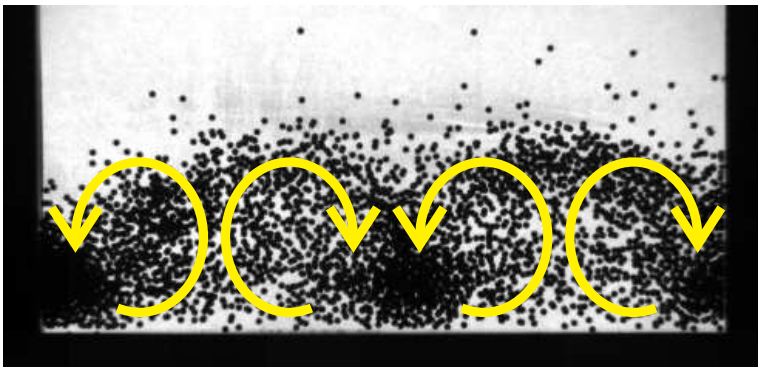

Peter Eshuis, Meheboob Alam, Devaraj van der Meer, Ko van der Weele, Stefan Luding, and Detlef Lohse, *preprint* (2008).

Buoyancy driven granular convection is studied for a shallow, vertically shaken granular bed in a quasi 2-D container. At sufficiently strong shaking counter-rotating convection rolls form with pronounced density variations. These rolls are also found in our Molecular Dynamics simulations. The onset of convection is quantitatively explained through a linear stability analysis of the hydrodynamic continuum model presented in Chapter 3.

4.1 Introduction

Ordinary fluids heated from below develop, when the heating is strong enough, so-called Rayleigh-Bénard convection rolls that effectively mix the cold and hot parts of the fluid [1–7]. As we have found in Chapter 2, similar convection rolls are observed in a system of vibrated granular particles, when the shaking is sufficiently strong, see Fig 4.1 [8]. Highly mobile particles move up in the dilute regions and are then sprayed sideways towards the dense clusters. The resemblance with an ordinary fluid is indeed remarkable, given the fact that the particles are not bound to each other by any adhesive forces.

In this paper we will model the granular convection in analogy with the hydrodynamic theory known from Rayleigh-Bénard convection, adapting it where necessary to the granular context. This study fits into the general context of what is probably the most important question in granular research today: "To what extent can hydrodynamic-like models describe phenomena observed in granular systems?" [9–13]. We will exploit experiment, numerical simulation, and theoretical analysis to provide insight in the underlying physics of buoyancy driven granular convection in vertically shaken granular matter.

Granular convection has been studied extensively at mild fluidization [14–39], for which the convection is boundary-driven. However, the buoyancy-driven convection observed here occurs at *high* fluidization and this has been reported rarely in the literature. We are aware of only one numerical study by Paolotti *et al.* [40] and one theoretical study by Khain and Meerson [41]. Here we present to our knowledge the first experimental observation. In the numerical model by Paolotti *et al.* the container walls were taken to be perfectly elastic, leading to convection patterns in which the rolls were either moving up or down along the sidewalls, whereas in our system (with dissipative walls) they always move down, see Fig 4.1. Another difference is that we observe that our convective state originates from an other steady state of vertically shaken granular matter, namely the

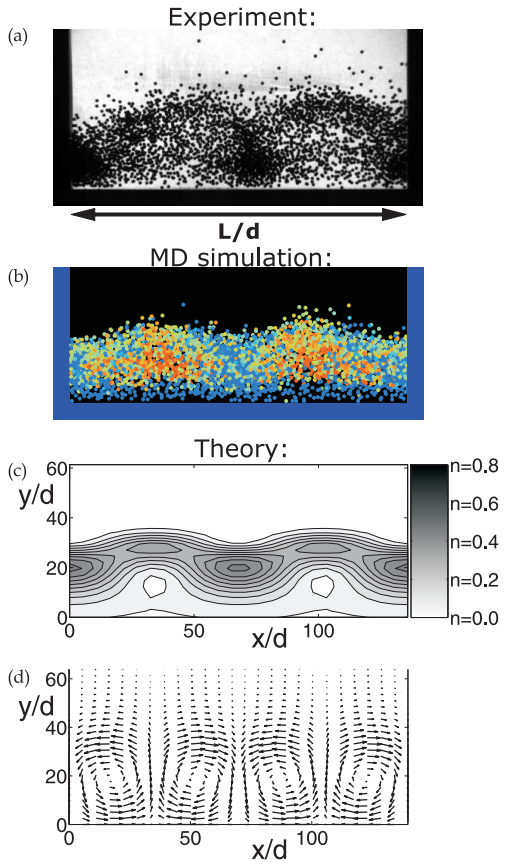

Figure 4.1: Experiment, MD simulation, and Theory: (a) The quasi 2-D experimental setup showing granular convection for $F = 6.2$ layers of $d = 1.0$ mm steel beads shaken at $a = 3.0$ mm and $f = 55.0$ Hz (dimensionless shaking strength $S = 110$). The adjustable container length is $L/d = 101$ in this experiment. Two convective cells are present here, each consisting of a pair of counter-rotating rolls. The beads move up in the dilute regions (high granular temperature) and are sprayed sideways to the three dense clusters (low granular temperature). The sidewalls induce a downward motion due to the extra dissipation, so we always find a cluster at the wall. (b) Molecular Dynamics simulation for $F = 6$ particle layers shaken at $a = 3.0$ mm and $f = 71$ Hz ($S = 183$). The red colored (dark) particles are moving upward and the blue (light) ones downward. (c) The density profile according to our hydrodynamic theory for $F = 6$ layers and a dimensionless shaking strength of $S = 110$. The color coding indicates the regions with high density (black) and low density (white). (d) The corresponding theoretical velocity profile showing two pairs of counter-rotating convection rolls.

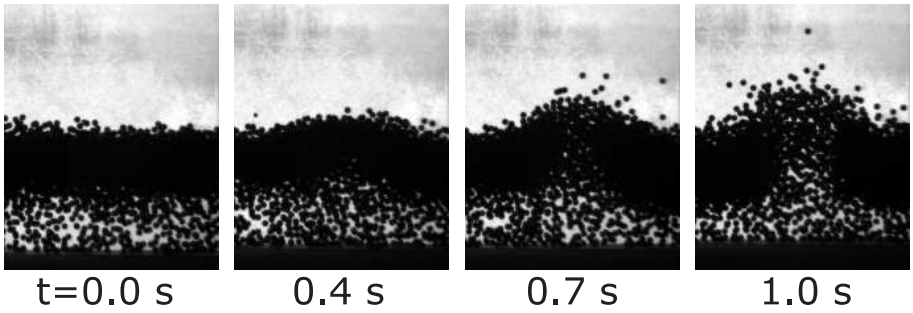

Figure 4.2: Experiment: Breakthrough of a convection roll for $F = 11.1$ layers of steel beads shaken at an amplitude of $a = 3.0$ mm and frequency $f = 45$ Hz (dimensionless shaking strength $S = 75$). These pictures show approximately one-third of the total container length $L/d = 101$, close to the right wall, from an experiment in which the frequency was linearly increased from $f = 42$ Hz to $f = 48$ Hz at a rate of 90 Hz/min. The breakthrough of the convection roll, starting from the Leidenfrost state, took place in less than 1 second, i.e., $\Delta f < 1.5$ Hz.

granular Leidenfrost state (see Fig. 4.2).

Khain and Meerson studied the onset of thermal convection in a granular gas using granular hydrodynamics. The geometry of their system was an infinite two-dimensional horizontal layer with a (fully elastic) closed top. In contrast, our experiment has a free surface instead of a closed top, which calls for a different kind of modelling. Another, even more important, difference is that Khain and Meerson [41] performed linear stability analysis on a *homogeneous* base state with a linear temperature profile to study the onset of convection, whereas we start out from the *inhomogeneous* Leidenfrost state in which a solid phase is supported by a gas phase. This state is obtained numerically as the solution of the hydrodynamic model by Eshuis *et al.* [42], see Ch. 3, and we will show that the experimentally observed onset of convection is *quantitatively* explained by a linear stability analysis around this state.

4.2 Experimental Setup and Results

Our experimental setup (Fig. 4.1) consists of a quasi 2-D perspex container of dimensions $L \times D \times H$ with an adjustable container length $L = 10 - 202$ mm, a depth $D = 5$ mm, and a height $H = 150$ mm. The container is partially filled with steel beads of diameter $d = 1.0$ mm, density $\rho = 7800$ kg/m^3, and coefficient

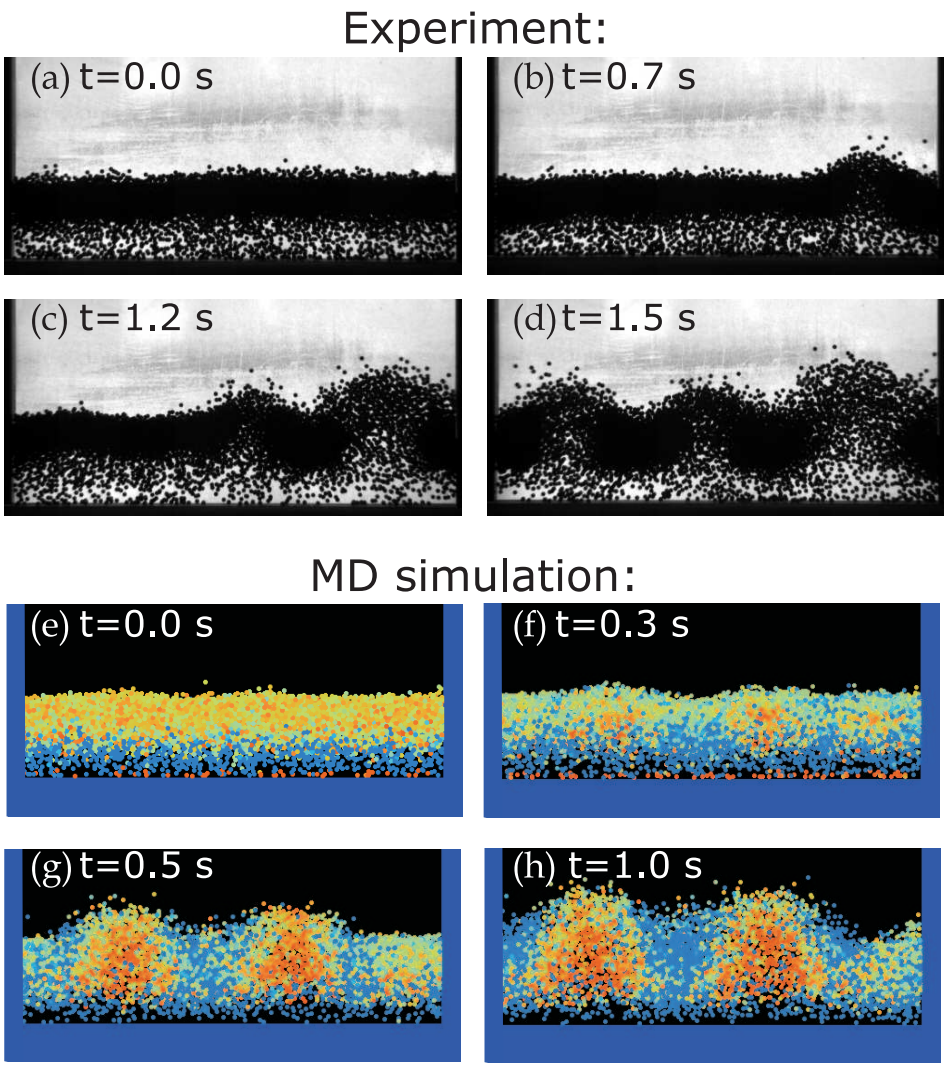

Figure 4.3: Experiment vs. MD simulation: Onset of convection. (a,b,c,d) The onset of convection for $F = 11.1$ layers of steel beads in a container of length $L/d = 101$ shaken at an amplitude of $a = 3.0$ mm and frequency $f = 45$ Hz ($S = 75$). The frequency was linearly increased in the range of $f = 42 - 48$ Hz at 90 Hz/min. The transition from the steady Leidenfrost state to fully developed convection took place in 1.5 seconds, i.e., $\Delta f < 2.3$ Hz. (e,f,g,h) The breakthrough process in a Molecular Dynamics simulation for the same number of layers as in experiment with shaking amplitude $a = 3.5$ mm and frequency $f = 80$ Hz ($S = 315$).

of normal restitution $e \approx 0.9$. The setup is mounted on a sinusoidally vibrating shaker with tunable frequency f and amplitude a. The experiments are recorded with a high-speed camera capturing 2000 frames per run at a frame rate of 1000 frames per second.

The natural dimensionless control parameters to analyze the experiments are:

- the shaking parameter for *strong* fluidization [8]:

$$S = \frac{a^2\omega^2}{gd}, \tag{4.1}$$

  with $\omega = 2\pi f$ and $g = 9.81$ m/s^2. The shaking strength S is the ratio of the kinetic energy inserted into the system by the vibrating bottom and the potential energy associated with the particle diameter d,

- the number of bead layers F,

- the inelasticity parameter $\varepsilon = (1 - e^2)$,

- the aspect ratio L/d.

The parameter ε is taken to be constant in this paper, since we ignore the velocity dependence and use steel beads throughout unless otherwise stated. The aspect ratio L/d is varied in the range of $L/d = 10 - 202$ by adjusting the container length L in steps of 4 mm; So, we will systematically vary all dimensionless parameters (except the inelasticity parameter ε) by changing the amplitude a, the frequency f, the number of layers F and the container length L.

From where do the convection rolls in our granular system originate? At high fluidization the rolls are formed out of the Leidenfrost state, in which a cluster of slow almost immobile particles is supported by a gaseous region of fast particles underneath. Figure 4.2 shows how a number of particles becomes more mobile (higher granular temperature) than the surrounding ones and creates an opening in the floating cluster of the Leidenfrost state. These particles have picked up an excess of energy from the vibrating bottom (due to a statistical fluctuation) and collectively move upwards, very much like the onset of Rayleigh-Bénard convection in a classical fluid heated from below. This upward motion of the highly mobile beads must be balanced by a downward movement of neighboring particles, leading to the formation of a convection roll.

The downward motion is most easily accomplished at the sidewalls, due to the extra source of dissipation (i.e., the friction with the walls), and for this reason

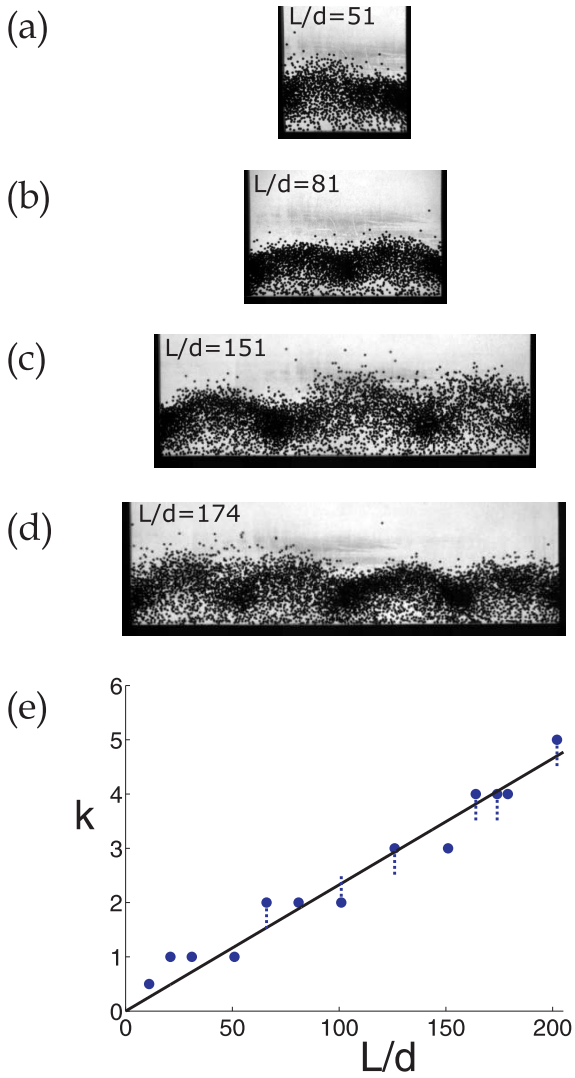

Figure 4.4: Experiment: The number of convective cells k for increasing container length L/d, keeping the number of layers fixed at $F = 6.2$ and the shaking strength at $S = 63$ ($a = 2.5$ mm and $f = 50$ Hz): (a) $k = 1$ (one pair of convection rolls), (b) $k = 2$ (two pairs), (c) $k = 3$, (d) $k = 4$. (e) The number of convective cells k as a function of the container length L/d for the same parameter values as in (a)-(d). The dotted vertical lines denote a situation in which the system continuously switches between two states with a different number of rolls, as explained in the text. The intrinsic cell length Λ, determined from the linear fit through the data points, is $\Lambda = 43$ mm.

the first convection roll is always seen to initiate near one of the two sidewalls. As shown in Fig. 4.3, this first roll within a second triggers the formation of rolls along the entire length of the container, leading to a fully developed convection pattern.

To find out how these fully developed convection patterns depend on the dimensionless control parameters, we systematically varied them individually, starting with the aspect ratio L/d:

Figure 4.4 shows that when the aspect ratio L/d is increased, the number of convection rolls increases. Let k be the number of observed convective cells, each consisting of a *pair* of counter-rotating rolls. We find that k grows linearly with the aspect ratio L/d, see Fig. 4.4(e). This indicates that the cells have an intrinsic typical length Λ independent of the aspect ratio. This is again similar to the rolls in Rayleigh-Bénard convection for a normal fluid, which also have an intrinsic length. The intrinsic cell length ($\Lambda = 43$ mm) is determined from the linear fit through the experimental data and is indicated by the straight, black line in Fig. 4.4(e).

The dotted vertical lines in Fig. 4.4(e) represent an interesting feature. For these aspect ratios the system continuously switches between two states: The length of the system here is either too long or too short to fit k intrinsic cell lengths, and the system tries to release this frustration by going towards a situation with one convection roll extra or less. But the system cannot hold this state either, since at that moment there is no cluster at one of the sidewalls, and due to the extra dissipation with the wall the previous frustrated situation with an integer number of cells k is restored, repeating the series of events indefinitely. Only for a very small aspect ratio of L/d we observed a stable state with $k = 1/2$, i.e., one convection roll with one cluster. The aspect ratio here is too small to allow for any switching to a neighboring state, so this specific situation is stabilized.

The influence of the other two parameters, the shaking parameter S and the number of layers F, will be presented after the introduction of the numerical simulations in Section 4.3 and the theoretical stability analysis in Section 4.4.

4.3 Molecular Dynamics simulations

We have used Molecular Dynamics (MD) simulations, also known as discrete element method (DEM) [43–51], to numerically study the quasi 2-D system discussed in the previous Section. The container has a length $L/d = 202$, depth $D/d = 5$, and height $H/d = 150$. It contains either $N = 7467$ or $N = 11200$ identical particles (diameter $d = 1.0$ mm, density $\rho = 7800$ kg/m^3, and hence mass $m = 4.1$ mg), corresponding to $F \approx 6$ and $F \approx 11$ particle layers, respectively [52]. We applied sinusoidal vibrations to the system with amplitude a and frequency f, i.e., the trajectory of the vibrating bottom is $y(t) = a\sin(2\pi ft)$.

The inelastic particle collisions are modelled by the force-displacement relation: Since all the forces between the particles that are in contact with each other (or with the wall) are known, and also the positions and velocities of the particles, we can integrate Newton's equations of motion:

$$m\frac{\mathrm{d}^2\vec{r}_i}{\mathrm{d}t^2} = \vec{f}_i + m\vec{g} \quad \text{for the translational motion,} \tag{4.2}$$

$$I_i\frac{\mathrm{d}\vec{\omega}_i}{\mathrm{d}t} = \vec{q}_i \quad \text{for the rotational motion,} \tag{4.3}$$

with $\vec{r}_i$ the position of particle i, $\vec{f}_i = \sum \vec{f}_i$ the total force on particle i, $\vec{g}$ the gravitational acceleration, I_i the moment of inertia, $\vec{\omega}_i = \mathrm{d}\vec{\varphi}_i/\mathrm{d}t$ the angular velocity, and $\vec{q}_i$ the total torque on the particle. Equation (4.2) is a set of $\mathrm{D} + \mathrm{D}(\mathrm{D}-1)/2$ coupled ordinary differential equations solved in $\mathrm{D} = 3$ dimensions using numerical integration schemes [43, 44, 53].

The inelasticity of the particle interaction is modelled by the linear spring-dashpot model, which describes the particle contact as a damped harmonic oscillator [54]. This is the simplest normal contact force model that takes excluded volume effects into account. The interactions of the particles with the walls are described by the same set of equations with a different contact criterion implying an infinite wall mass. All simulations have been carried out without tangential forces and torques, which means that we assume perfectly smooth spherical particles.

The simulations are either initialized by preparing a Leidenfrost state in the system, or by starting up from the final configuration of the preceding simulation performed at lower shaking amplitude a. The latter procedure considerably reduces the transient time for which a stable, steady situation is observed in the

system. The transient time is short (less than 10 vibration periods) when one is well inside the Leidenfrost or convection regime. It grows however drastically (roughly by a factor 10) at the phase transition between these two regions. Therefore we have performed long runs of 10 s, which go well beyond this transient time, to obtain a situation in dynamic equilibrium. In these simulations we observed hysteresis effects around the onset of convection.

We have varied the friction the particles experience when they hit the walls and found that the onset of convection occurs at a smaller shaking strength S if the wall friction is lowered. Usually we have used the same restitution coefficient for the wall interactions and for the particle-particle interactions: $e_{\text{wall}} = e$. However, the collisions with the front and back wall (a large portion of all the collisions) involve smaller velocities. In this situation, the velocity dependence of the restitution coefficient may start to play a role [55, 56] and can thereby effectively increase the restitution coefficient of the particle-wall collisions. This partly accounts for the fact that in the current simulations the shaking strength S required to get convection is much larger than the corresponding value of S in experiments and theory. In addition the roll friction between the particles is set to a relatively high value in the current simulations. This makes the total dissipation artificially large and explains why the S-value required in the MD simulations is too high.

4.4 Theoretical Model

In this Section we are going to explain the experimental and numerical results by a hydrodynamic theory. Our model is analogous to the one used to determine the onset of Rayleigh-Bénard convection in classical fluids in which linear stability analysis is applied to the homogeneous base state [57]. We perform basically the same procedure with a more intricate base state, namely the inhomogeneous Leidenfrost state with the dense cluster on top of the gaseous region, and with various special constitutive relations due to the granular nature of the problem.

We will show that the linear stability analysis quantitatively captures the critical shaking strength for which the onset of convection is observed in experiment. Moreover, we will show that the theoretically determined cell length Λ reasonably agrees with the experimental observations.

4.4.1 Granular hydrodynamics

The basis of our analysis is formed by the hydrodynamic equations in two dimensions, which describe the three hydrodynamic continuum fields: The number density $n(x,y,t)$, the velocity field $\vec{u}(x,y,t)$, and the temperature $T(x,y,t)$ [57].

The first continuum field, the density, is described by the continuity equation (or mass balance) and describes how the density varies in time:

$$\frac{\partial n}{\partial t} + \vec{u}\cdot\vec{\nabla}n + n\vec{\nabla}\cdot\vec{u} = 0. \tag{4.4}$$

Secondly, the time-variations of the components of the two-dimensional velocity field $\vec{u}$ are governed by the Navier-Stokes equation (i.e., the momentum or force balance):

$$mn\left(\frac{\partial\vec{u}}{\partial t} + \vec{u}\cdot\vec{\nabla}\vec{u}\right) = mn\vec{g} - \vec{\nabla}p + \vec{\nabla}\cdot\left(\mu\left[\vec{\nabla}\vec{u} + \left(\vec{\nabla}\vec{u}\right)^T\right]\right) + \vec{\nabla}\left(\lambda\vec{\nabla}\cdot\vec{u}\right), \tag{4.5}$$

in which m is the mass of a single particle, p the pressure, $\vec{g}$ the gravitational acceleration, μ the shear viscosity and λ the second viscosity. The velocity field $\vec{u}$ is a vector in two dimensions, so we have two equations, one for $\partial u_x/\partial t$ and

one for $\partial u_y/\partial t$:

$$mn\left[\frac{\partial u_x}{\partial t}+\left(u_x\frac{\partial u_x}{\partial x}+u_y\frac{\partial u_x}{\partial y}\right)\right] = -\frac{\partial p}{\partial x}+2\frac{\partial}{\partial x}\left(\mu\frac{\partial u_x}{\partial x}\right) +\frac{\partial}{\partial y}\left[\mu\left(\frac{\partial u_x}{\partial y}+\frac{\partial u_y}{\partial x}\right)\right] + \frac{\partial}{\partial x}\left[\lambda\left(\frac{\partial u_x}{\partial x}+\frac{\partial u_y}{\partial y}\right)\right]. \quad (4.6)$$

$$mn\left[\frac{\partial u_y}{\partial t}+\left(u_x\frac{\partial u_y}{\partial x}+u_y\frac{\partial u_y}{\partial y}\right)\right] = -mng-\frac{\partial p}{\partial y}+2\frac{\partial}{\partial y}\left(\mu\frac{\partial u_y}{\partial y}\right) +\frac{\partial}{\partial x}\left[\mu\left(\frac{\partial u_x}{\partial y}+\frac{\partial u_y}{\partial x}\right)\right] + \frac{\partial}{\partial y}\left[\lambda\left(\frac{\partial u_x}{\partial x}+\frac{\partial u_y}{\partial y}\right)\right]. \quad (4.7)$$

The third continuum field is the granular temperature, which is defined as the velocity fluctuations of the particles around the mean velocity, i.e., $\frac{1}{2}k_BT = \frac{1}{2}m\left(\langle\vec{u}^2\rangle-\langle\vec{u}\rangle^2\right)$ with $k_B=1$. The temperature change in time is described by the energy equation or energy balance:

$$n\frac{\partial T}{\partial t}+n\vec{u}\cdot\vec{\nabla}T=\vec{\nabla}\cdot\left(\kappa\vec{\nabla}T\right)-p\left(\vec{\nabla}\cdot\vec{u}\right)-I, \quad (4.8)$$

where κ is the thermal conductivity and I is the dissipative term due to the inelastic particle collisions. In Eq. (4.8) we did not include terms which are quadratic in $\vec{\nabla}\vec{u}$.

4.4.2 Constitutive relations

The granular hydrodynamic equations of Eqs. (4.4)-(4.8) are to be complemented by constitutive relations for the pressure field p, the energy dissipation rate I, and the transport coefficients κ, μ, and λ. Since our system combines dilute, gaseous regions with clusters where the density approaches unity, we need to take excluded volume effects into account.

First we have the equation of state for a two dimensional granular fluid [42, 58, 59]:

$$p=nT\frac{n_c+n}{n_c-n}, \quad \text{with} \quad n_c=\frac{2}{\sqrt{3}d^2}, \quad (4.9)$$

which is the ideal gas law with a VanderWaals-like correction [58] to account for the excluded area with $n_c=2/\sqrt{3}d^2$ the number density of a hexagonal close-packed crystal.

The second constitutive relation is the energy dissipation rate I [42, 58, 59]:

$$I = \frac{\varepsilon}{\gamma_c \ell} nT\sqrt{\frac{T}{m}}. \tag{4.10}$$

Here the inelasticity parameter $\varepsilon = (1-e^2)$, which we already identified as one of the experimental control parameters of this system, shows up also in the theoretical model. The value for the constant $\gamma_c = 2.26$ has been adopted from Grossman *et al.* [58].

The first transport coefficient is the thermal conductivity κ [42, 58, 59]:

$$\kappa = \frac{n(\alpha\ell + d)^2}{\ell}\sqrt{\frac{T}{m}}, \tag{4.11}$$

with the mean free path $\ell = (n_c - n)/[\sqrt{8}nd(n_c - an)]$ according to Grossman *et al.* [58], with the constant $a = 1 - \sqrt{3/8} = 0.39$ and n_c the number density of a hexagonal close-packed crystal. For the constant α we adopted the value $\alpha = 0.6$ from Meerson *et al.* [59].

In the literature various choices are proposed for the shear viscosity μ in granular systems [31, 35, 60], and in Appendix A we will show that the results for our system strongly depends on the relation chosen for μ. We take:

$$\mu = m\mathrm{Pr}\,\kappa, \tag{4.12}$$

in which Pr is the Prandtl number, which measures the ratio between convective and diffusive energy transfer. This dimensionless number is in principle unknown and we will show that in our system Pr is a constant of order unity, just as it is for molecular gases. Because the viscosity μ for our granular system behaves so analogously to classical fluids, we use the Stokes approximation (applicable for incompressible fluids, implying that the bulk viscosity is zero) to get the expression for the second viscosity λ [31, 35, 60]:

$$\lambda = -\frac{2}{3}\mu. \tag{4.13}$$

4.4.3 Linearization around the Leidenfrost state

As the model presented above is an extension of the one used in [42], see Ch. 3, the Leidenfrost state $n_L(y)$, $T_L(y)$ is a numerical solution, and we will now proceed

to linearize Eqs (4.4), (4.6), (4.7), and (4.8) around this state by adding a small perturbation to it:

$$\begin{aligned} n(x,y,t) &= n_L(y) + \delta n(x,y,t), && (4.14)\\ u_x(x,y,t) &= 0 + \delta u_x(x,y,t), && (4.15)\\ u_y(x,y,t) &= 0 + \delta u_y(x,y,t), && (4.16)\\ T(x,y,t) &= T_L(y) + \delta T(x,y,t). && (4.17) \end{aligned}$$

The next step is to insert this perturbed Leidenfrost state in the four hydrodynamic Eqs. (4.4), (4.6), (4.7), and (4.8). For every equation we have sorted the terms up to $O(\delta^2)$ in the following way: δn, δu_x, δu_y, and δT, each on its own line.

The linearized version of the continuity equation of Eq. (4.4) then reads:

$$\begin{aligned} \frac{\partial(\delta n)}{\partial t} = & \; 0 \\ & - n_L \frac{\partial(\delta u_x)}{\partial x} \\ & - \frac{\partial n_L}{\partial y}\delta u_y - n_L \frac{\partial(\delta u_y)}{\partial y} \\ & + 0. \end{aligned} \tag{4.18}$$

The force balance for the x-direction of Eq. (4.6) is linearized as follows

$$\begin{aligned} m n_L \frac{\partial(\delta u_x)}{\partial t} = & - \frac{\partial p}{\partial n}\Big|_L \frac{\partial(\delta n)}{\partial x} \\ & + 2\mu_L \frac{\partial^2(\delta u_x)}{\partial x^2} + \frac{\partial}{\partial y}\left(\mu_L \frac{\partial(\delta u_x)}{\partial y}\right) + \lambda_L \frac{\partial^2(\delta u_x)}{\partial x^2} \\ & + \frac{\partial}{\partial y}\left(\mu_L \frac{\partial(\delta u_y)}{\partial x}\right) + \lambda_L \left(\frac{\partial^2(\delta u_y)}{\partial x \partial y}\right) \\ & - \frac{\partial p}{\partial T}\Big|_L \frac{\partial(\delta T)}{\partial x}. \end{aligned} \tag{4.19}$$

Linearizing the force balance for the y-direction (4.7) yields:

$$\begin{aligned} mn_L\frac{\partial(\delta u_y)}{\partial t} = & - \left[mg+\frac{\partial}{\partial y}\left(\frac{\partial p}{\partial n}\Big|_L\right)\right]\delta n - \frac{\partial p}{\partial n}\Big|_L\frac{\partial(\delta n)}{\partial y} \\ & + \mu_L\frac{\partial^2(\delta u_x)}{\partial x\partial y}+\frac{\partial\lambda_L}{\partial y}\frac{\partial(\delta u_x)}{\partial x}+\lambda_L\frac{\partial^2(\delta u_x)}{\partial x\partial y} \\ & + 2\frac{\partial\mu_L}{\partial y}\frac{\partial(\delta u_y)}{\partial y}+2\mu_L\frac{\partial^2(\delta u_y)}{\partial y^2}+\mu_L\frac{\partial^2(\delta u_y)}{\partial x^2}+\frac{\partial\lambda_L}{\partial y}\frac{\partial(\delta u_y)}{\partial y} \\ & \qquad +\lambda_L\frac{\partial^2(\delta u_y)}{\partial y^2} \\ & - \frac{\partial}{\partial y}\left(\frac{\partial p}{\partial T}\Big|_L\right)\delta T - \frac{\partial p}{\partial T}\Big|_L\frac{\partial(\delta T)}{\partial y}. \end{aligned} \tag{4.20}$$

Finally, the energy balance of Eq. (4.8) reads in linearized form:

$$\begin{aligned} n_L\frac{\partial(\delta T)}{\partial t} = & \left[-\frac{\partial I}{\partial n}\Big|_L+\frac{\partial}{\partial y}\left(\frac{\partial\kappa}{\partial n}\Big|_L\right)\frac{\partial T_L}{\partial y}+\frac{\partial\kappa}{\partial n}\Big|_L\frac{\partial^2 T_L}{\partial y^2}\right]\delta n \\ & \qquad +\frac{\partial\kappa}{\partial n}\Big|_L\frac{\partial T_L}{\partial y}\frac{\partial(\delta n)}{\partial y} \\ & - p_L\frac{\partial(\delta u_x)}{\partial x} \\ & - n_L\frac{\partial T_L}{\partial y}\delta u_y - p_L\frac{\partial(\delta u_y)}{\partial y} \\ & + \left[\frac{\partial}{\partial y}\left(\frac{\partial\kappa}{\partial T}\Big|_L\right)\frac{\partial T_L}{\partial y}+\frac{\partial\kappa}{\partial T}\Big|_L\frac{\partial^2 T_L}{\partial y^2}-\frac{\partial I}{\partial T}\Big|_L\right]\delta T \\ & \qquad +\left(\frac{\partial\kappa_L}{\partial y}+\frac{\partial\kappa}{\partial T}\Big|_L\frac{\partial T_L}{\partial y}\right)\frac{\partial(\delta T)}{\partial y} \\ & \qquad +\kappa_L\frac{\partial^2(\delta T)}{\partial x^2}+\kappa_L\frac{\partial^2(\delta T)}{\partial y^2}. \end{aligned} \tag{4.21}$$

4.4.4 Boundary conditions

The linearized hydrodynamic equations are accompanied by boundary conditions for the perturbed density, velocities, and temperature. First, conservation of particles must apply:

$$\int_0^L dx\int_0^\infty dy\, n(x,y,t) = F\, n_c\, d \quad \rightarrow \quad \int_0^L dx\int_0^\infty dy\,\delta n(x,y,t) = 0. \tag{4.22}$$

Since the Leidenfrost density obeys $\int_0^\infty dy n_L(y) = N_{\text{total}}$, so the integral over the perturbed number density is zero. Here the number of layers F (already identified as a control parameter in the experiments) arises as a relevant control parameter also in the theoretical model. As we will see later, this integral relation will not be used directly in the mathematical solution of the model, but still reflects an essential feature of the system.

We assume that the velocity field in the x-direction has an extremum (either a maximum or a minimum) at the bottom of the container, so the derivative of δu_x should be zero here:

$$\frac{\partial(\delta u_x)}{\partial y}\Big|_{y=0} = 0. \tag{4.23}$$

The velocity component in the y-direction necessarily vanishes at the bottom, and consequently

$$\delta u_y(x,0,t) = 0. \tag{4.24}$$

For the boundary conditions at the top ($y \to \infty$) we assume that the velocity field vanishes altogether, leading to the following relations for the perturbed velocity fields:

$$\lim_{y\to\infty} \delta u_x(x,y,t) = 0, \tag{4.25}$$

$$\lim_{y\to\infty} \delta u_y(x,y,t) = 0. \tag{4.26}$$

As we impose a granular temperature T_0 at the bottom [with $T_0 \propto m(af)^2$ directly related to the kinetic energy imparted to the particles by the vibrating bottom], the boundary condition for the perturbed temperature should be zero:

$$\delta T(x,0,t) = 0. \tag{4.27}$$

Finally we have the boundary condition for the granular temperature at the top, which we assume to vanish just like the velocity field. So, the condition for perturbed temperature at the top becomes

$$\lim_{y\to\infty} \delta T(x,y,t) = 0. \tag{4.28}$$

As will be seen in Section 4.4.6 these seven boundary conditions are sufficient to describe the system.

4.4.5 Making the hydrodynamic equations dimensionless

The next step we take is to non-dimensionalize our linearized hydrodynamic equations and boundary conditions. To this end we first have to choose non-dimensional units. First, the density is made dimensionless by the number density n_c of a hexagonal close packing in 2-D:

$$n \mapsto \widetilde{n} = \frac{n}{n_c}, \quad \text{with} \quad n_c = \frac{2}{\sqrt{3}d^2}. \tag{4.29}$$

Secondly, the temperature field is made dimensionless by the imposed granular temperature at the bottom T_0:

$$T \mapsto \widetilde{T} = \frac{T}{T_0}. \tag{4.30}$$

For the dimensionless length scales in our system we can choose between the container length L and the particle diameter d. Since the latter one is kept constant throughout our study, and the first one not, we non-dimensionalize the length scales as follows:

$$x \mapsto \widetilde{x} = \frac{x}{d}, \tag{4.31}$$

$$y \mapsto \widetilde{y} = \frac{y}{d}, \tag{4.32}$$

and we do the same for the mean free path

$$\ell = \frac{1}{\sqrt{8}nd}\frac{n_c - n}{n_c - an} \mapsto \widetilde{\ell} = \frac{\ell}{d} = \sqrt{\frac{3}{32}}\left[\frac{1}{\widetilde{n}}\left(\frac{1-\widetilde{n}}{1-a\widetilde{n}}\right)\right], \tag{4.33}$$

with $a = 1 - \sqrt{3/8}$ [58].

To make the time t dimensionless we make use of the dimensionality of the granular temperature (energy), the mass of one particle m, and the diameter d:

$$t \mapsto \widetilde{t} = t\frac{\sqrt{T_0/m}}{d}, \tag{4.34}$$

and consequently the velocity fields u_x and u_y become in dimensionless form:

$$u_x \mapsto \widetilde{u}_x = \frac{u_x}{\sqrt{T_0/m}}, \tag{4.35}$$

$$u_y \mapsto \widetilde{u}_y = \frac{u_y}{\sqrt{T_0/m}}. \tag{4.36}$$

By inserting the dimensionless fields into the hydrodynamic equations we deduce the non-dimensional form of p, I and the transport coefficients of Eqs. (4.9)-(4.13). The equation of state then becomes:

$$p = nT\frac{n_c+n}{n_c-n} \mapsto \widetilde{p} = \frac{p}{n_c T_0} = \widetilde{n}\widetilde{T}\frac{1+\widetilde{n}}{1-\widetilde{n}}. \tag{4.37}$$

The dimensionless form of the energy dissipation rate I is:

$$I = \frac{\varepsilon}{\gamma\ell} nT\sqrt{\frac{T}{m}} \;\mapsto\; \widetilde{I} = \frac{Id}{n_c T_0\sqrt{T_0/m}} = \frac{\varepsilon}{\gamma}\frac{\widetilde{n}\widetilde{T}\sqrt{\widetilde{T}}}{\widetilde{\ell}}. \tag{4.38}$$

The first transport coefficient κ now reads:

$$\kappa = \frac{n(\alpha\ell+d)^2}{\ell}\sqrt{\frac{T}{m}} \;\mapsto\; \widetilde{\kappa} = \frac{\kappa}{n_c d\sqrt{T_0/m}} = \frac{\left(\alpha\widetilde{\ell}+1\right)^2}{\widetilde{\ell}}\widetilde{n}\sqrt{\widetilde{T}}. \tag{4.39}$$

Eq. (4.12) relates the shear viscosity μ to the thermal conductivity κ, so μ now reads in dimensionless form:

$$\mu = m\mathrm{Pr}\,\kappa \mapsto \widetilde{\mu} = \mathrm{Pr}\,\widetilde{\kappa}, \tag{4.40}$$

and from Eq. (4.13) the second viscosity λ follows immediately:

$$\lambda = -\frac{2}{3}\mu = -\frac{2}{3}m\mathrm{Pr}\,\kappa \mapsto \widetilde{\lambda} = -\frac{2}{3}\mathrm{Pr}\,\widetilde{\kappa}. \tag{4.41}$$

We can now write the hydrodynamic equations in dimensionless form, starting with the linearized continuity equation of Eq. (4.18):

$$\begin{aligned}\frac{\partial(\delta\widetilde{n})}{\partial\widetilde{t}} = \;& 0 \\ & - \;\widetilde{n}_L\frac{\partial(\delta\widetilde{u}_x)}{\partial\widetilde{x}} \\ & - \;\frac{\partial\widetilde{n}_L}{\partial\widetilde{y}}\delta\widetilde{u}_y - \widetilde{n}_L\frac{\partial(\delta\widetilde{u}_y)}{\partial\widetilde{y}} \\ & + \;0.\end{aligned} \tag{4.42}$$

The dimensionless form of the force balance in the x-direction [Eq. (4.19)] becomes:

$$\begin{aligned}\widetilde{n}_L\frac{\partial(\delta\widetilde{u}_x)}{\partial\widetilde{t}} = &- \frac{\partial\widetilde{p}}{\partial\widetilde{n}}\Big|_L\frac{\partial(\delta\widetilde{n})}{\partial\widetilde{x}}\\ &+ 2\widetilde{\mu}_L\frac{\partial^2(\delta\widetilde{u}_x)}{\partial\widetilde{x}^2}+\frac{\partial}{\partial\widetilde{y}}\left[\widetilde{\mu}_L\frac{\partial(\delta\widetilde{u}_x)}{\partial\widetilde{y}}\right]+\widetilde{\lambda}_L\frac{\partial^2(\delta\widetilde{u}_x)}{\partial\widetilde{x}^2}\\ &+ \frac{\partial}{\partial\widetilde{y}}\left[\widetilde{\mu}_L\frac{\partial(\delta\widetilde{u}_y)}{\partial\widetilde{x}}\right]+\widetilde{\lambda}_L\frac{\partial^2(\delta\widetilde{u}_y)}{\partial\widetilde{x}\partial\widetilde{y}}\\ &- \frac{\partial\widetilde{p}}{\partial\widetilde{T}}\Big|_L\frac{\partial(\delta\widetilde{T})}{\partial\widetilde{x}}.\end{aligned} \tag{4.43}$$

The force balance for the y-direction [Eq. (4.20)] takes the following dimensionless form:

$$\begin{aligned}\widetilde{n}_L\frac{\partial(\delta\widetilde{u}_y)}{\partial\widetilde{t}} = &- \frac{1}{S}\delta\widetilde{n}-\frac{\partial}{\partial\widetilde{y}}\left(\frac{\partial\widetilde{p}}{\partial\widetilde{n}}\Big|_L\right)\delta\widetilde{n}-\frac{\partial\widetilde{p}}{\partial\widetilde{n}}\Big|_L\frac{\partial(\delta\widetilde{n})}{\partial\widetilde{y}}\\ &+ \widetilde{\mu}_L\frac{\partial^2(\delta\widetilde{u}_x)}{\partial\widetilde{x}\partial\widetilde{y}}+\frac{\partial\widetilde{\lambda}_L}{\partial\widetilde{y}}\frac{\partial(\delta\widetilde{u}_x)}{\partial\widetilde{x}}+\widetilde{\lambda}_L\frac{\partial^2(\delta\widetilde{u}_x)}{\partial\widetilde{x}\partial\widetilde{y}}\\ &+ 2\frac{\partial\widetilde{\mu}_L}{\partial\widetilde{y}}\frac{\partial(\delta\widetilde{u}_y)}{\partial\widetilde{y}}+2\widetilde{\mu}_L\frac{\partial^2(\delta\widetilde{u}_y)}{\partial\widetilde{y}^2}+\widetilde{\mu}_L\frac{\partial^2(\delta\widetilde{u}_y)}{\partial\widetilde{x}^2}+\frac{\partial\widetilde{\lambda}_L}{\partial\widetilde{y}}\frac{\partial(\delta\widetilde{u}_y)}{\partial\widetilde{y}}\\ &\qquad +\widetilde{\lambda}_L\frac{\partial^2(\delta\widetilde{u}_y)}{\partial\widetilde{y}^2}\\ &- \frac{\partial}{\partial\widetilde{y}}\left(\frac{\partial\widetilde{p}}{\partial\widetilde{T}}\Big|_L\right)\delta\widetilde{T}-\frac{\partial\widetilde{p}}{\partial\widetilde{T}}\Big|_L\frac{\partial(\delta\widetilde{T})}{\partial\widetilde{y}}.\end{aligned} \tag{4.44}$$

In the first term on the right hand side appears the dimensionless shaking strength S:

$$S=\frac{T_0}{mgd}\quad\text{with}\quad T_0\propto m(af)^2. \tag{4.45}$$

This S was already introduced as the governing shaking parameter in the context of our experiments, see Eq. (4.1). In particular we did *not* use $\Gamma=a\omega^2/g$ the more familiar dimensionless acceleration. This choice is now justified by hydrodynamic theory.

Finally, the energy balance of Eq. (4.21) in dimensionless form becomes:

$$\begin{aligned}
\widetilde{n}_L \frac{\partial(\delta\widetilde{T})}{\partial\widetilde{t}} = \quad & \left[-\frac{\partial\widetilde{I}}{\partial\widetilde{n}}\Big|_L + \frac{\partial}{\partial\widetilde{y}}\left(\frac{\partial\widetilde{\kappa}}{\partial\widetilde{n}}\Big|_L\right)\frac{\partial\widetilde{T}_L}{\partial\widetilde{y}} + \frac{\partial\widetilde{\kappa}}{\partial\widetilde{n}}\Big|_L \frac{\partial^2\widetilde{T}_L}{\partial\widetilde{y}^2}\right]\delta\widetilde{n} \\
& + \frac{\partial\widetilde{\kappa}}{\partial\widetilde{n}}\Big|_L \frac{\partial\widetilde{T}_L}{\partial\widetilde{y}}\frac{\partial(\delta\widetilde{n})}{\partial\widetilde{y}} \\
- \quad & \widetilde{p}_L \frac{\partial(\delta\widetilde{u}_x)}{\partial\widetilde{x}} \\
- \quad & \widetilde{n}_L \frac{\partial\widetilde{T}_L}{\partial\widetilde{y}}\delta\widetilde{u}_y - \widetilde{p}_L\frac{\partial(\delta\widetilde{u}_y)}{\partial\widetilde{y}} \\
+ \quad & \left[\frac{\partial}{\partial\widetilde{y}}\left(\frac{\partial\widetilde{\kappa}}{\partial\widetilde{T}}\Big|_L\right)\frac{\partial\widetilde{T}_L}{\partial\widetilde{y}} + \frac{\partial\widetilde{\kappa}}{\partial\widetilde{T}}\Big|_L\frac{\partial^2\widetilde{T}_L}{\partial\widetilde{y}^2} - \frac{\partial\widetilde{I}}{\partial\widetilde{T}}\Big|_L\right]\delta\widetilde{T} \\
& + \left(\frac{\partial\widetilde{\kappa}_L}{\partial\widetilde{y}} + \frac{\partial\widetilde{\kappa}}{\partial\widetilde{T}}\Big|_L\frac{\partial\widetilde{T}_L}{\partial\widetilde{y}}\right)\frac{\partial(\delta\widetilde{T})}{\partial\widetilde{y}} \\
& + \widetilde{\kappa}_L\frac{\partial^2(\delta\widetilde{T})}{\partial\widetilde{x}^2} + \widetilde{\kappa}_L\frac{\partial^2(\delta\widetilde{T})}{\partial\widetilde{y}^2}
\end{aligned} \tag{4.46}$$

We now proceed with writing the boundary conditions in dimensionless form. We start with the conservation of particles relation of Eq. (4.22):

$$\int_0^{L/d} d\widetilde{x}\int_0^{\infty} d\widetilde{y}\,\delta\widetilde{n}(\widetilde{x},\widetilde{y},\widetilde{t}) = 0. \tag{4.47}$$

The boundary condition for the velocity fields in x- and y-direction at the bottom [Eqs. (4.23) and (4.24)] become:

$$\frac{\partial(\delta\widetilde{u}_x)}{\partial\widetilde{y}}\Big|_{\widetilde{y}=0} = 0, \tag{4.48}$$

$$\delta\widetilde{u}_y(\widetilde{x},0,\widetilde{t}) = 0, \tag{4.49}$$

and those for the velocity fields at the top [Eqs (4.25) and (4.26)] take the form:

$$\lim_{\widetilde{y}\to\infty}\delta\widetilde{u}_x(\widetilde{x},\widetilde{y},\widetilde{t}) = 0, \tag{4.50}$$

$$\lim_{\widetilde{y}\to\infty}\delta\widetilde{u}_y(\widetilde{x},\widetilde{y},\widetilde{t}) = 0. \tag{4.51}$$

Equation (4.27) for the imposed temperature at the bottom becomes in dimensionless form:

$$\delta\widetilde{T}(\widetilde{x},0,\widetilde{t}) = 0, \tag{4.52}$$

and finally, the temperature condition at the top [Eq. (4.28)] becomes:

$$\lim_{\widetilde{y}\to\infty} \delta\widetilde{T}(\widetilde{x},\widetilde{y},\widetilde{t}) = 0. \tag{4.53}$$

4.4.6 Formulation of the eigenvalue problem

Having brought the linearized hydrodynamic equations plus the accompanying boundary conditions in dimensionless form, we are now ready to formulate the eigenvalue problem. We start by applying the following Ansatz for the form of the perturbations:

$$\begin{aligned}
\delta\widetilde{n} &= N(\widetilde{y})e^{ik_x\widetilde{x}}e^{\gamma\widetilde{t}}, && (4.54)\\
\delta\widetilde{u}_x &= U(\widetilde{y})e^{ik_x\widetilde{x}}e^{\gamma\widetilde{t}}, && (4.55)\\
\delta\widetilde{u}_y &= V(\widetilde{y})e^{ik_x\widetilde{x}}e^{\gamma\widetilde{t}}, && (4.56)\\
\delta\widetilde{T} &= \Theta(\widetilde{y})e^{ik_x\widetilde{x}}e^{\gamma\widetilde{t}}. && (4.57)
\end{aligned}$$

Here $N(\widetilde{y})$, $U(\widetilde{y})$, $V(\widetilde{y})$, and $\Theta(\widetilde{y})$ are the vertical profiles of the perturbation fields. The terms with $e^{ik_x\widetilde{x}}$ contain the wave number k_x, expressing the periodicity in the x-direction, see for example Fig. 4.1. In the factor $e^{\gamma\widetilde{t}}$ we have $\gamma = \gamma_R + i\gamma_I$, where the real part γ_R denotes the growth/decay rate of the perturbation and the imaginary part γ_I indicates the frequency of the wave. In the current study the predicted instabilities are found to be stationary, i.e., $\gamma_I = 0$ and hence $\gamma = \gamma_R$. So when $\gamma < 0$ the Leidenfrost state is stable and when $\gamma > 0$ it is unstable. In the latter case the Leidenfrost state gives way to convection rolls for this specific value of γ, i.e., the *eigenvalue*.

This Ansatz is inserted in the four hydrodynamic equations, so the continuity equation of Eq. (4.42) then takes the following form:

$$\begin{aligned}
0 = \quad & \gamma N \\
+ \quad & \widetilde{n}_L k_x U \\
+ \quad & \frac{\partial\widetilde{n}_L}{\partial\widetilde{y}}V + \widetilde{n}_L V' \\
+ \quad & 0.
\end{aligned} \tag{4.58}$$

The force balance for the x-direction [Eq. (4.43)] transforms into:

$$\begin{aligned} 0 = & - \frac{\partial \widetilde{p}}{\partial \widetilde{n}}\Big|_L k_x N \\ & + \left[\widetilde{n}_L \gamma + \left(2\widetilde{\mu}_L + \widetilde{\lambda}_L\right) k_x^2\right] U - \frac{\partial \widetilde{\mu}_L}{\partial \widetilde{y}} U' - \widetilde{\mu}_L U'' \\ & + \frac{\partial \widetilde{\mu}_L}{\partial \widetilde{y}} k_x V + \left(\widetilde{\mu}_L + \widetilde{\lambda}_L\right) k_x V' \\ & - \widetilde{\frac{\partial p}{\partial \widetilde{T}}}\Big|_L k_x \Theta, \end{aligned} \tag{4.59}$$

and the force balance for the y-direction [Eq. (4.44)] becomes:

$$\begin{aligned} 0 = & \left[\frac{1}{S} + \frac{\partial}{\partial \widetilde{y}}\left(\frac{\partial \widetilde{p}}{\partial \widetilde{n}}\Big|_L\right)\right] N + \frac{\partial \widetilde{p}}{\partial \widetilde{n}}\Big|_L N' \\ & - \frac{\partial \widetilde{\lambda}_L}{\partial \widetilde{y}} k_x U - \left(\widetilde{\mu}_L + \widetilde{\lambda}_L\right) k_x U' \\ & + \left[\widetilde{n}_L \gamma + \widetilde{\mu}_L k_x^2\right] V - \left[2\frac{\partial \widetilde{\mu}_L}{\partial \widetilde{y}} + \frac{\partial \widetilde{\lambda}_L}{\partial \widetilde{y}}\right] V' - \left[2\widetilde{\mu}_L + \widetilde{\lambda}_L\right] V'' \\ & + \frac{\partial}{\partial \widetilde{y}}\left(\widetilde{\frac{\partial p}{\partial \widetilde{T}}}\Big|_L\right) \Theta + \widetilde{\frac{\partial p}{\partial \widetilde{T}}}\Big|_L \Theta'. \end{aligned} \tag{4.60}$$

Finally, the energy balance of Eq. (4.46) takes the form:

$$\begin{aligned} 0 = & \left[\frac{\partial \widetilde{I}}{\partial \widetilde{n}}\Big|_L - \frac{\partial}{\partial \widetilde{y}}\left(\frac{\partial \widetilde{\kappa}}{\partial \widetilde{n}}\Big|_L\right) \frac{\partial \widetilde{T}_L}{\partial \widetilde{y}} - \frac{\partial \widetilde{\kappa}}{\partial \widetilde{n}}\Big|_L \frac{\partial^2 \widetilde{T}_L}{\partial \widetilde{y}^2}\right] N - \widetilde{\frac{\partial \kappa}{\partial \widetilde{n}}}\Big|_L \frac{\partial \widetilde{T}_L}{\partial \widetilde{y}} N' \\ & + \widetilde{p}_L k_x U \\ & + \widetilde{n}_L \frac{\partial \widetilde{T}_L}{\partial \widetilde{y}} V + \widetilde{p}_L V' \\ & + \left[\widetilde{n}_L \gamma - \widetilde{\kappa}_L k_x^2 - \frac{\partial}{\partial \widetilde{y}}\left(\frac{\partial \widetilde{\kappa}}{\partial \widetilde{T}}\Big|_L\right) \frac{\partial \widetilde{T}_L}{\partial \widetilde{y}} - \frac{\partial \widetilde{\kappa}}{\partial \widetilde{T}}\Big|_L \frac{\partial^2 \widetilde{T}_L}{\partial \widetilde{y}^2} + \frac{\partial \widetilde{I}}{\partial \widetilde{T}}\Big|_L\right] \Theta \\ & \qquad - \left[\frac{\partial \widetilde{\kappa}}{\partial \widetilde{y}} + \frac{\partial \widetilde{\kappa}}{\partial \widetilde{T}}\Big|_L \frac{\partial \widetilde{T}_L}{\partial \widetilde{y}}\right] \Theta' + \widetilde{\kappa}_L \Theta''. \end{aligned} \tag{4.61}$$

These four equations (4.58)-(4.61) can be written as a 4×4 matrix problem for the column vector (N,U,V,Θ) and its first and second derivative:

$$\mathbf{A}\cdot\begin{pmatrix} N\\ U\\ V\\ \Theta\end{pmatrix}''+\mathbf{B}\cdot\begin{pmatrix} N\\ U\\ V\\ \Theta\end{pmatrix}'+\mathbf{C}\cdot\begin{pmatrix} N\\ U\\ V\\ \Theta\end{pmatrix}=0, \tag{4.62}$$

where the apostrophe denotes differentiation with respect to $\widetilde{y}$. The elements of the 4×4 matrices **A**, **B**, and **C** can be read from the hydrodynamic equations (4.58)-(4.61):

$$\mathbf{A}=\begin{pmatrix} 0 & 0 & 0 & 0\\ 0 & -\widetilde{\mu}_L & 0 & 0\\ 0 & 0 & -2\widetilde{\mu}_L-\widetilde{\lambda}_L & 0\\ 0 & 0 & 0 & \widetilde{\kappa}_L\end{pmatrix}, \tag{4.63}$$

$$\mathbf{B}=\begin{pmatrix} 0 & 0 & \widetilde{n}_L & 0\\ 0 & -\frac{\partial\widetilde{\mu}_L}{\partial\widetilde{y}} & (\widetilde{\mu}_L+\widetilde{\lambda}_L)k_x & 0\\ \frac{\partial\widetilde{p}}{\partial\widetilde{n}}\big|_L & -(\widetilde{\mu}_L+\widetilde{\lambda}_L)k_x & -2\frac{\partial\widetilde{\mu}_L}{\partial\widetilde{y}}-\frac{\partial\widetilde{\lambda}_L}{\partial\widetilde{y}} & \frac{\partial\widetilde{p}}{\partial\widetilde{T}}\big|_L\\ -\frac{\partial\widetilde{\kappa}}{\partial\widetilde{n}}\big|_L\frac{\partial\widetilde{T}_L}{\partial\widetilde{y}} & 0 & \widetilde{p}_L & -\frac{\partial\widetilde{\kappa}_L}{\partial\widetilde{y}}-\frac{\partial\widetilde{\kappa}}{\partial\widetilde{T}}\big|_L\frac{\partial\widetilde{T}_L}{\partial\widetilde{y}}\end{pmatrix}, \tag{4.64}$$

$$\mathbf{C}=\begin{pmatrix} \gamma & \widetilde{n}_Lk_x & ; & \frac{\partial\widetilde{n}_L}{\partial\widetilde{y}} & 0\\ -\frac{\partial\widetilde{p}}{\partial\widetilde{n}}\big|_Lk_x & \widetilde{n}_L\gamma+(2\widetilde{\mu}_L+\widetilde{\lambda}_L)k_x^2 & ; & \frac{\partial\widetilde{\mu}_L}{\partial\widetilde{y}}k_x & -\frac{\partial\widetilde{p}}{\partial\widetilde{T}}\big|_Lk_x\\ \frac{1}{S}+\frac{\partial}{\partial\widetilde{y}}\left(\frac{\partial\widetilde{p}}{\partial\widetilde{n}}\big|_L\right) & -\frac{\partial\widetilde{\lambda}_L}{\partial\widetilde{y}}k_x & ; & \widetilde{n}_Lk_x^2 & \frac{\partial}{\partial\widetilde{y}}\left(\frac{\partial\widetilde{p}}{\partial\widetilde{T}}\big|_L\right)\\ -\frac{\partial}{\partial\widetilde{y}}\left(\frac{\partial\widetilde{\kappa}}{\partial\widetilde{n}}\big|_L\right)\frac{\partial\widetilde{T}_L}{\partial\widetilde{y}} & \widetilde{p}_Lk_x & ; & \widetilde{n}_L\frac{\partial\widetilde{T}_L}{\partial\widetilde{y}} & \widetilde{n}_L\gamma-\frac{\partial}{\partial\widetilde{y}}\left(\frac{\partial\widetilde{\kappa}}{\partial\widetilde{T}}\big|_L\right)\frac{\partial\widetilde{T}_L}{\partial\widetilde{y}}\\ +\frac{\partial\widetilde{I}}{\partial\widetilde{n}}\big|_L-\frac{\partial\widetilde{\kappa}}{\partial\widetilde{n}}\big|_L\frac{\partial^2\widetilde{T}_L}{\partial\widetilde{y}^2} & & & & -\widetilde{\kappa}_Lk_x^2-\frac{\partial\widetilde{\kappa}}{\partial\widetilde{T}}\big|_L\frac{\partial^2\widetilde{T}_L}{\partial\widetilde{y}^2}+\frac{\partial\widetilde{I}}{\partial\widetilde{T}}\big|_L\end{pmatrix}. \tag{4.65}$$

The matrices **A**, **B** and **C** are functions of the height $\widetilde{y}$ through their dependence on the unperturbed Leidenfrost state $\widetilde{n}_L(\widetilde{y})$, $\widetilde{T}_L(\widetilde{y})$. To calculate the matrices **A**, **B** and **C** we need the constitutive relations and their various derivatives (pressure $\widetilde{p}$, energy dissipation rate $\widetilde{I}$, thermal conductivity $\widetilde{\kappa}$, shear viscosity $\widetilde{\mu}$, and second viscosity $\widetilde{\lambda}$). These are all given in Appendix B.

Note that the first equation in Eq. (4.62) is of first order, whereas the other three are of second order, such that the seven boundary conditions from Section 4.4.4 completely determine the solution.

4.4.7 Linear stability analysis using spectral methods

To solve the eigenvalue problem of Eq. (4.62), which is a matrix problem consisting of four coupled ordinary differential equations, standard methods for linear equations can be applied.

The goal is to locate the onset of convection by finding the eigenvalues γ for which the Leidenfrost state becomes unstable (i.e., $\gamma > 0$). The wave number k_x corresponding to the most unstable mode (maximal γ-value) determines the dominant perturbation that will start the convection for this particular Leidenfrost state.

We use the spectral-collocation method to perform the linear stability analysis. Spectral methods find their origin in the 1940s and were revived by Orszag [61] in the 1970s, after which they gradually became mainstream in scientific computation [62]. These methods are designed to solve differential equations, making use of trial functions (also known as expansion or approximating functions) and the so-called test or weight functions.

The trial functions represent the approximate solution of the differential equations. They are linear combinations of a suitable family of basis functions, e.g., trigonometric (Fourier) polynomials; these functions are global in contrast to the basis functions used for instance in finite-element or finite-difference methods, which are local. The test functions guarantee that the differential equations and the boundary conditions are satisfied at the collocation points.

Thanks to the linearity of the problem we have various options for the trial basis functions, namely trigonometric or Fourier polynomials, Chebyshev polynomials, Legendre polynomials, and many more. In the y-direction our system of equations is non-periodic, so Fourier polynomials are not suitable as trial basis functions along the y-direction. We will therefore use Chebyshev polynomials, which have been widely used in many stability problems [62, 63] and turn out to

be convenient for our current stability analysis of the Leidenfrost state.

The Chebyshev polynomials $T_k(y)$ are defined as follows on the $y = [-1,1]$ domain [62]:

$$T_k(y) = \cos\left(k\cos^{-1} y\right), \quad k = 0,1,2\ldots \tag{4.66}$$

A particular convenient choice for the collocation points y_j in the case of Chebyshev polynamials is the Gauss-Lobatto choice, which fixes the trial functions at the points:

$$y_j = \cos\left(\frac{\pi j}{N}\right), \quad j = 0,\ldots,N, \tag{4.67}$$

and this transforms the basis functions into:

$$T_k(y_j) = \cos\left(\frac{\pi jk}{N}\right), \quad j = 0,\ldots,N, \;\; k = 0,1,2\ldots \tag{4.68}$$

The Gauss-Lobatto points (4.67) are used to collocate the momentum and energy equations plus the corresponding boundary conditions.

To collocate the continuity equation we use the so-called Gauss points:

$$y_j = \cos\left(\pi\frac{(2j+1)}{2N+2}\right), \quad j = 0,\ldots,N, \tag{4.69}$$

which brings the corresponding basis functions into the following form:

$$T_k(y_j) = \cos\left(\frac{\pi(2j+1)k}{2N+2}\right), \quad j = 0,\ldots,N, \;\; k = 0,1,2\ldots \tag{4.70}$$

One may note that the Gauss points do not include the boundary points, whereas the Gauss-Lobatto points *do* describe the boundaries. The reason for this is that we do not want to collocate the density at the boundary, because we do not have actual boundary conditions for $\delta\widetilde{n}$. [Instead for $\delta\widetilde{n}$ we have the integral constraint of the particle conservation over the whole system, Eq. (4.47).] This is no problem, since we can reduce the set of four hydrodynamic equations through elimination of the number density $\delta\widetilde{n}$ by making use of the continuity equation, which is of first order, as already remarked in the context of Eq. (4.62). We then get a system of three coupled equations for the velocity fields $\delta\widetilde{u}_x$ and $\delta\widetilde{u}_y$, and the granular temperature $\delta\widetilde{T}$. Therefore we do not need a boundary condition for $\delta\widetilde{n}$ [64], but only boundary conditions (at the bottom and the top) for $\delta\widetilde{u}_x$, $\delta\widetilde{u}_y$, and $\delta\widetilde{T}$, i.e., the conditions (4.48)-(4.53).

The matrix problem defined by Eqs. (4.62)-(4.65) and the boundary conditions of Eqs. (4.48)-(4.53) are then translated from the physical domain $\widetilde{y} = [0, H_{\max}]$ (with $H_{\max}$ the truncated height of the system in particle diameters) to the $y = [-1, 1]$ domain (on which the trial functions are defined) via the following transformation:

$$y = \lim_{H \to H_{\max}} \frac{2\widetilde{y}}{H} - 1. \tag{4.71}$$

We have used a truncated physical domain up to $y = H_{\max}$ where we have also applied the boundary conditions. The value of $H_{\max}$ ranges from 30 to 80 particle diameters depending on the parameters. Using the grid formed by the Gauss and Gauss-Lobatto points the linear stability analysis of the hydrodynamic model is performed using the spectral-collocation method as described in detail in the book by Canuto, Hussaini, Quarteroni, and Zang [62].

4.4.8 Solution

As an example of a state on which we have performed the stability analysis we show in Fig. 4.5(a) the Leidenfrost state for $F = 11$ layers at a shaking strength

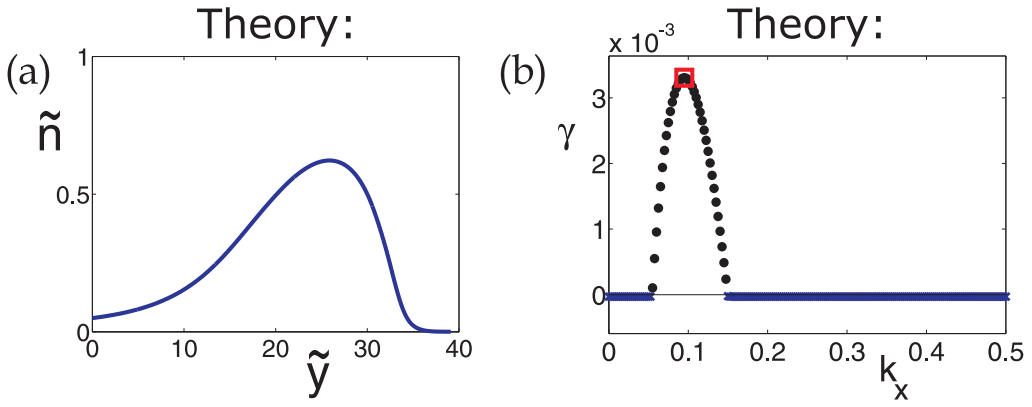

Figure 4.5: Theory: (a) The density profile $\widetilde{n}(\widetilde{y})$ for the Leidenfrost state for $F = 11$ layers and shaking strength $S = 200$, used as a base state for the linear stability analysis. (b) The growth rate γ as a function of the wave number k_x for the Leidenfrost solution depicted in (a). For all blue crosses $\gamma < 0$, meaning that the Leidenfrost state is stable. The black dots indicate the unstable modes corresponding to $\gamma > 0$. The most unstable mode, marked by the red square, defines the dominant wave number ($k_{x,\max} = 0.095$) and hence the length of the convection cell: $\Lambda = 2\pi/k_{x,\max} = 66$ particle diameters.

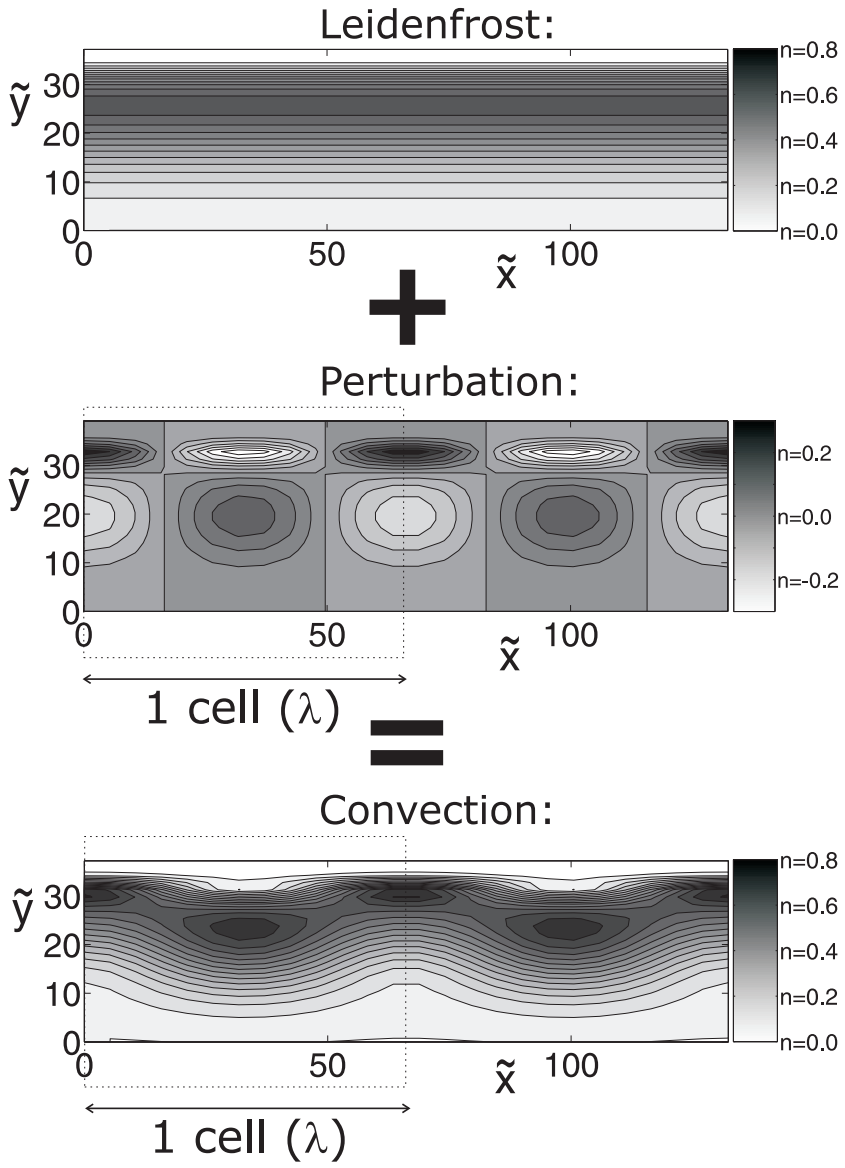

Figure 4.6: Theory: The construction of the density profile of the convective state for $F = 11$ and $S = 200$ by adding the perturbation (obtained from the linear stability analysis) to the corresponding Leidenfrost state. From the stability analysis of Fig. 4.5 we know that the cell length is $\Lambda = 66$ particle diameters; two cell lengths are depicted here. Dark colors indicate regions of high density.

$S = 200$. Since this base state is a numerical solution, the matrices **A**, **B** and **C** necessary to solve Eq. (4.62) are generated numerically. The growth rate γ obtained from the solution of Eq. (4.62), using the spectral-collocation method, is depicted in Fig. 4.5(b). It shows an interval of k_x-values for which γ is positive (i.e., the Leidenfrost state is unstable); The convection mode that will manifest itself for this particular Leidenfrost state is associated with the wave number $k_{x,\max} = 0.095$, for which the growth rate is maximal (marked by the red square). Thus, hydrodynamic theory predicts a cell length (consisting of a pair of counter-rotating convection rolls) of $\Lambda = 2\pi/k_{x,\max} = 66$ particle diameters.

From this dominant perturbation mode we can determine the density profile of the corresponding convection pattern as illustrated by Fig. 4.6: It is the sum of the Leidenfrost density profile and the perturbation profile.

This linear stability analysis has been performed on a large number of Leidenfrost states obtained from the hydrodynamic model, where we systematically varied the number of layers F and the shaking strength S. This ultimately leads to the phase diagram of Fig. 4.9 in which we compare hydrodynamic theory with the experimental observations, as will be discussed in detail in the next Section.

4.5 Comparing Experiment, Numerics, and Theory

We now have the results of the experiments, Molecular Dynamics simulations, and theory, and in this Section we will check how they compare. We will start with the convection threshold and then look into the three hydrodynamic continuum fields: density, velocity, and temperature.

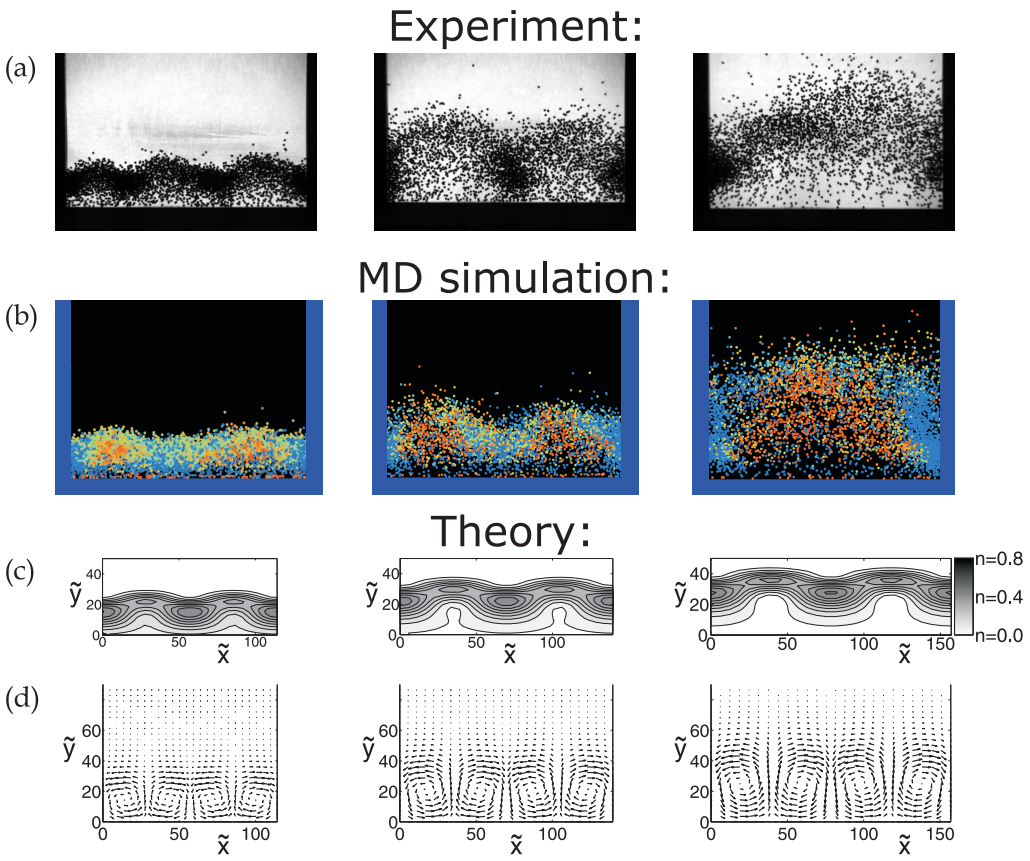

Figure 4.7: Experiment, MD simulation, and Theory: (a) Convection patterns for $F = 6.2$ particle layers in a container of length $L/d = 101$ at three consecutive shaking strengths: $S = 58$, $S = 130$, and $S = 202$. (b) Snapshots of MD simulations for $F = 6$ layers in a container of length $L/d = 200$ for $S = 173$, $S = 561$, and $S = 839$. (c,d) Two cell lengths ($2\Lambda/d$) of the theoretical density and velocity profiles for $F = 6$ layers shaken at $S = 60$, $S = 130$, and $S = 200$. The respective cell lengths are $\Lambda/d = 57$, 70, and 79.

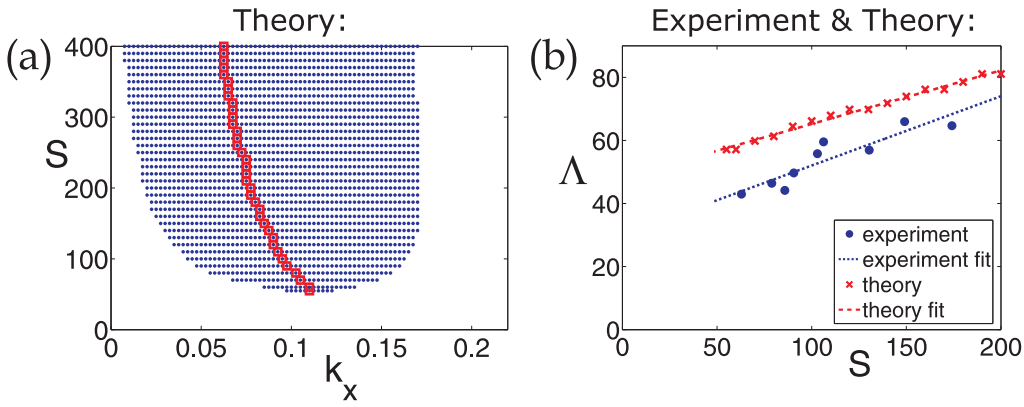

Figure 4.8: (a) Shaking strength S vs. wave number k_x for $F = 6$ layers. The blue dots correspond to the unstable modes k_x as determined by the linear stability analysis of our hydrodynamic model. The smallest S-value for which an unstable mode is found defines the onset of convection: $S_{\mathrm{conv}} = 55$. The red squares mark the most unstable mode at each shaking strength and determines the theoretical length of a convective cell: $\Lambda = 2\pi/k_{x,\mathrm{max}}$. (b) Experiment vs. Theory: Cell length Λ as a function of shaking strength S. The blue dots indicate the experiments with $F = 6.2$ particle layers, where Λ is determined from a plot such as depicted in Fig. 4.4(e). The dotted blue line is a linear fit through the experimental data. The red crosses are theoretical data obtained from the instability region depicted in (a), and the dashed red line is a linear fit through these theoretical points.

4.5.1 Cell length Λ vs. Shaking strength S

The comparison of experiment, MD simulation, and theory of Fig. 4.7 reveals that if the shaking strength S is increased the convective cells expand and consequently the number of convection rolls fitting the container becomes smaller. This dependence is studied in more detail in Fig. 4.8 for the experiments and hydrodynamic theory.

Figure 4.8(a) shows which Leidenfrost states for $F = 6$ layers are stable (corresponding to an eigenvalue $\gamma < 0$, white region), and which ones are unstable ($\gamma > 0$, dotted region) and thus give way to convection. The region of instability defines the critical shaking strength $S_{\mathrm{conv}} = 55$ required for the onset of convection for this number of layers F. When the shaking strength is increased beyond this critical value, the instability region is seen to widen and at the same time the dominant wave number $k_{x,\mathrm{max}}$ [marked by the red squares in Fig. 4.8(a)] becomes smaller. This means that the cell length $\Lambda = 2\pi/k_{x,\mathrm{max}}$ increases with S.

Comparing with experiment, Fig. 4.8(b), we see that the theoretically pre-

dicted cell length ($\Lambda = 2\pi/k_{x,\max}$) consistently overestimates the experimentally observed cell lengths. Both show a linear dependence though, and the theoretical prediction becomes better for stronger fluidization.

The comparison of experiment and theory culminates in the (S,F)-phase diagram of Fig. 4.9 showing the onset of convection for various number of layers [65]. Experiment and theory are seen to be in excellent agreement. The only fit parameter we have used is the Prandtl number of Eq. (4.12), the value of which we have fixed to $\mathrm{Pr} = 1.7$.

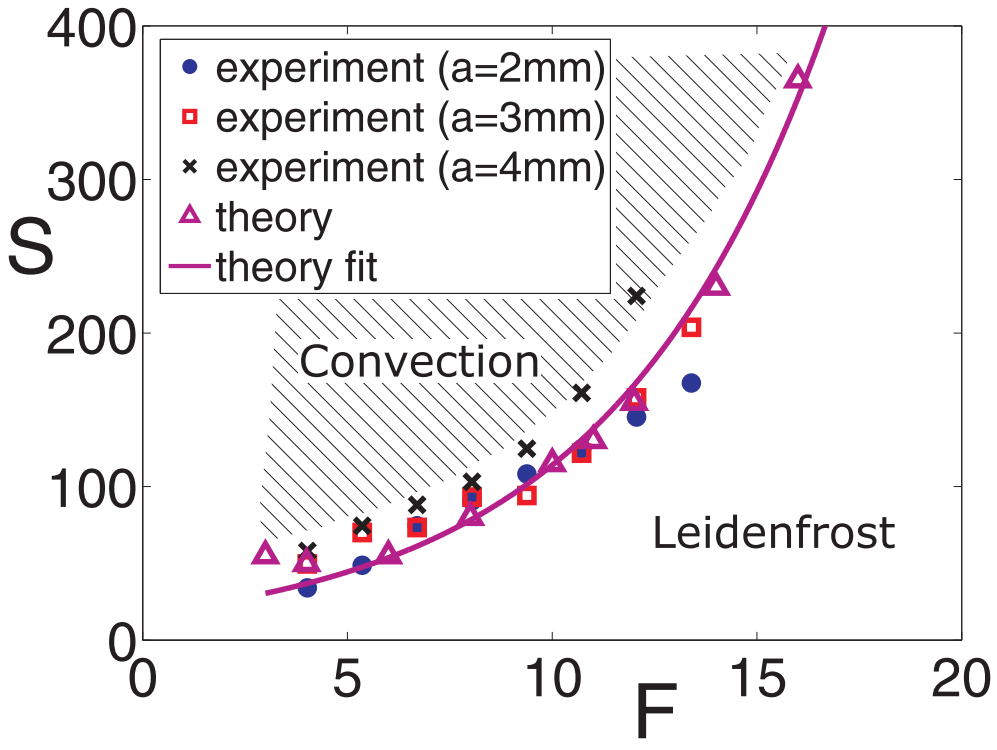

Figure 4.9: Experiment and Theory: The convection threshold in (S,F)-phase diagram. The experiments are performed with $d = 1$ mm glass beads, with shaking amplitude $a =$ 2.0 mm (blue dots), $a = 3.0$ mm (red squares), and $a = 4.0$ mm (black crosses). The shaking strength S is varied via the frequency f. The theoretical data points (indicated by magenta triangles) depend sensitively on the expression used for the viscosity: Here we have taken $\widetilde{\mu}(\widetilde{n},\widetilde{T}) = \mathrm{Pr}\,\widetilde{\kappa}(\widetilde{n},\widetilde{T})$ with the dimensionless Prandtl number $\mathrm{Pr} = 1.7$. The magenta line is a fit through these theoretical points.

4.5.2 Density profile

In Fig. 4.10 we compare the density profiles for experiment, MD simulation, and theory. The experimental density profile [Fig. 4.10(a)] is determined by averaging over 250 high-speed snapshots. Because the density is estimated from the projection of our quasi 2-D system, the density is slightly overestimated. The simulation profile [Fig. 4.10(b)] is based on a single snapshot, averaged over the depth of the container.

The density profiles of Fig. 4.10 are seen to agree closely. The only mismatch is the shaking strength S of the MD simulation compared to the experimental and theoretical value. This is probably due to the relatively high roll friction the colliding particles experience, thereby making the total dissipation artificially large, as explained in Section 4.3.

In Fig. 4.7 we have shown how the experiments, simulations, and theory depend on the shaking strength S. The increasing cell length Λ for stronger fluidization has already been treated in the previous subsection. Besides, the cells also expand in height, which is an indication of the approaching transition from convection rolls to a granular gas.

In the theoretical density and velocity profiles, Fig. 4.7(c,d), we have plotted two cell lengths Λ, determined by the value of $k_{x,\max}$ of the dominant perturbation mode. If we translate these cell lengths to the experimental and numerical container length of $L/d = 101$, theory predicts that the container should contain $k = 2$, 2, and 1 convective cells respectively (against $k = 3$, 2, 1 in experiment and MD simulations). So, the linear stability analysis of the hydrodynamic model is in reasonable quantitative agreement with the experiments and MD simulations.

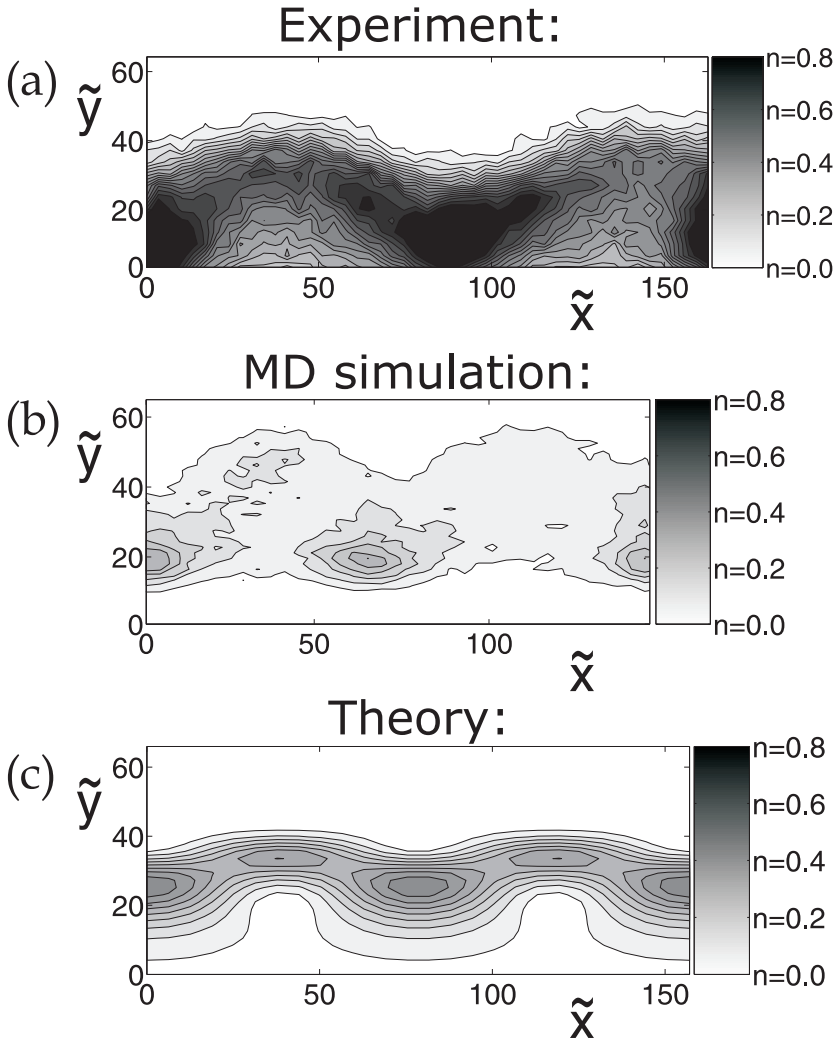

Figure 4.10: Comparing Experiment, MD simulation, and Theory: (a) The density profile (averaged over 250 high-speed snapshots) of $F = 6.2$ layers of steel beads in a container of length $L/d = 164$, shaken at $a = 4.0$ mm and $f = 52$ Hz ($S = 174$). This experimental profile shows 2 convective cells, where the color coding indicates the regions with high density (black) and low density (white). (b) Averaged density profile of a MD simulation showing three convective cells for $F = 6$ layers in a container of length $L/d = 200$, with shaking amplitude $a = 4.0$ mm and frequency $f = 83$ Hz ($S = 444$). (c) The theoretical density profile for $F = 6$ and $S = 170$ plotted for two cell lengths: $2\Lambda/d = 158$.

4.5.3 Velocity profile

The velocity field cannot be extracted in a straightforward way from the experiment, because the particles overlap in the high-speed pictures of the quasi 2-D setup. We therefore compare only the MD simulations with hydrodynamic theory, see Fig. 4.11. Disregarding the mismatch of the shaking strength S, as discussed in Section 4.3, the velocity fields are very similar and display nearly the same cell length Λ. A particularly fine point of correspondence is that both in simulation and in theory the rolls are tilted a bit.

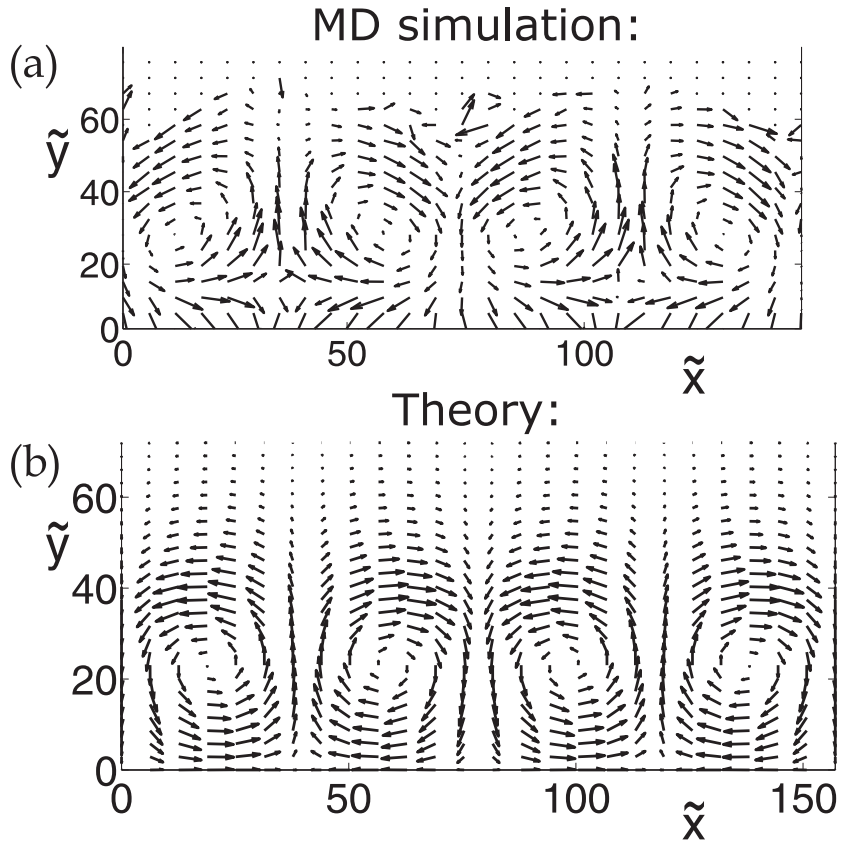

Figure 4.11: MD simulation vs. Theory: (a) Velocity profile based on a snapshot from a MD simulation with $F = 6$ layers in a container of length $L/d = 200$, shaken with an amplitude $a = 4.0$ mm and frequency $f = 83$ Hz ($S = 444$). (b) The theoretical velocity profile plotted for two cell lengths ($2\Lambda/d = 158$) for $F = 6$ layers and shaking strength $S = 170$.

4.5.4 Temperature profile

The granular temperature profile can be determined from the velocity field and because this data is only available for the MD simulations and hydrodynamic theory we compare these two in Fig. 4.12.

The theoretical temperature profile of Fig. 4.12(b) is determined in a similar manner as the theoretical density profile [Fig. 4.6]: The perturbed temperature profile determined from the linear stability analysis is added to the temperature profile of the Leidenfrost state. The small scale structures present in the numerical convective cells [Fig. 4.12(a)] are due to the fact that this plot is based on one

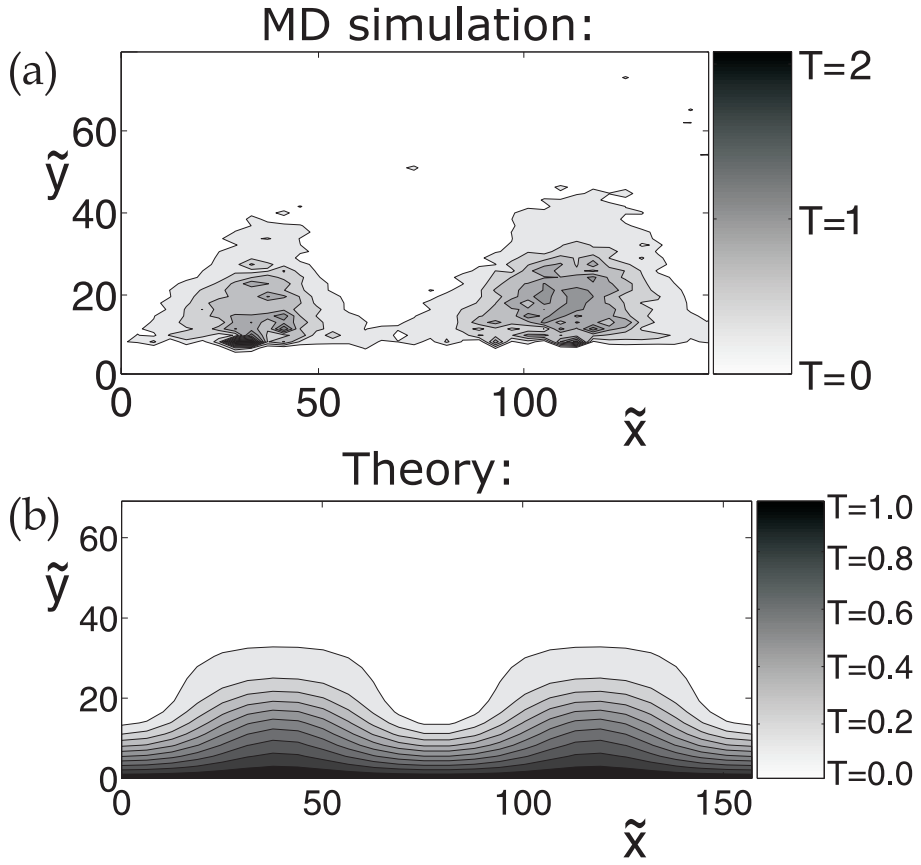

Figure 4.12: MD simulation vs. Theory: (a) Temperature profile based on a snapshot from a MD simulation with $F = 6$ layers in a container of length $L/d = 200$, shaken at $a = 4.0$ mm and $f = 83$ Hz ($S = 444$). (b) Two cell lengths ($2\Lambda/d = 158$) of the theoretical temperature profile with $F = 6$ layers and shaking strength $S = 170$.

single snapshot and the white region near the bottom is simply due to the fact that this layer is evacuated by the vibrating bottom. Apart from these two features, hydrodynamic theory and MD simulations match well.

4.6 Conclusion

We have studied buoyancy driven convection in vertically shaken granular matter, exploiting experiment, numerics, and hydrodynamic theory. At strong shaking strength counter-rotating convection rolls are formed and this phenomenon is found to be analogous to Rayleigh-Bénard convection for ordinary fluids with a free surface. Special features in our case are that the convection originates not from a homogeneous fluid, but from the inhomogeneous Leidenfrost state (with a dense cluster floating on a gaseous region) and the specific granular properties of the system expressed by the constitutive relations.

In analogy with the theory of Rayleigh-Bénard convection in ordinary fluids [57] we have performed a linear stability analysis of the hydrodynamic model for this Leidenfrost state [42]. The results of this continuum description are found to be in good overall agreement with the experimental observations, and in particular the threshold in the (S,F)-phase diagram for the onset of convection (Fig. 4.9) shows a perfect match between experiment and theory. This is a great success for granular hydrodynamics and stresses its applicability to collective phenomena in strongly shaken granular matter.

4.7 Appendix A

There is quite some discussion on the shear viscosity μ in granular systems and consequently various expressions have been proposed in the literature. Brey *et al.* [60] give the following relation for two dimensions and for a dilute granular gas:

$$\mu(T) = \frac{1}{2d}\sqrt{\frac{mT}{\pi}}\mu^*(e), \tag{4.72}$$

where $\mu^*(e)$ is a function of the restitution coefficient e.

Ohtsuki and Ohsawa [35] deduce an expression for μ including a dependence on the density n to account for excluded volume effects:

$$\mu(n,T) = \left\{\frac{1}{4}n^2d^3 + \frac{1}{2\pi d}\left(1+\frac{\pi}{4}nd^2\right)^2\right\}\sqrt{\pi mT}. \tag{4.73}$$

He *et al.* [31] propose that the shear viscosity should be equal to the thermal conductivity κ:

$$\mu(n,T) = \kappa(n,T), \tag{4.74}$$

i.e., they took the dimensionless Prandtl number to be $\mathrm{Pr} = \mu/\kappa = 1$. In the present paper we have found good correspondence between experiment and theory using a more general form:

$$\mu(n,T) = m\mathrm{Pr}\,\kappa(n,T), \tag{4.75}$$

where Pr is the dimensionless Prandtl number. We used it as a fit parameter for the phase diagram of Fig. 4.9 and found that $\mathrm{Pr} = 1.7$ gave excellent agreement.

Figure 4.13 shows the influence of μ on the resulting growth rate $\gamma(k_x)$, comparing the results obtained if one uses the expression by Brey *et al.* [Eq. (4.72)] with those obtained for expression Eq. (4.75). It is seen that the viscosity definition of Eq. (4.75) has a stabilizing effect on the Leidenfrost state with increasing number of particle layers F, in agreement with the experimental observations, whereas Eq. (4.72) has a destabilizing effect. We show in the (S,F)-phase diagram of Fig. 4.9 that Eq. (4.75) yields qualitative *and* quantitative agreement with the experimental results.

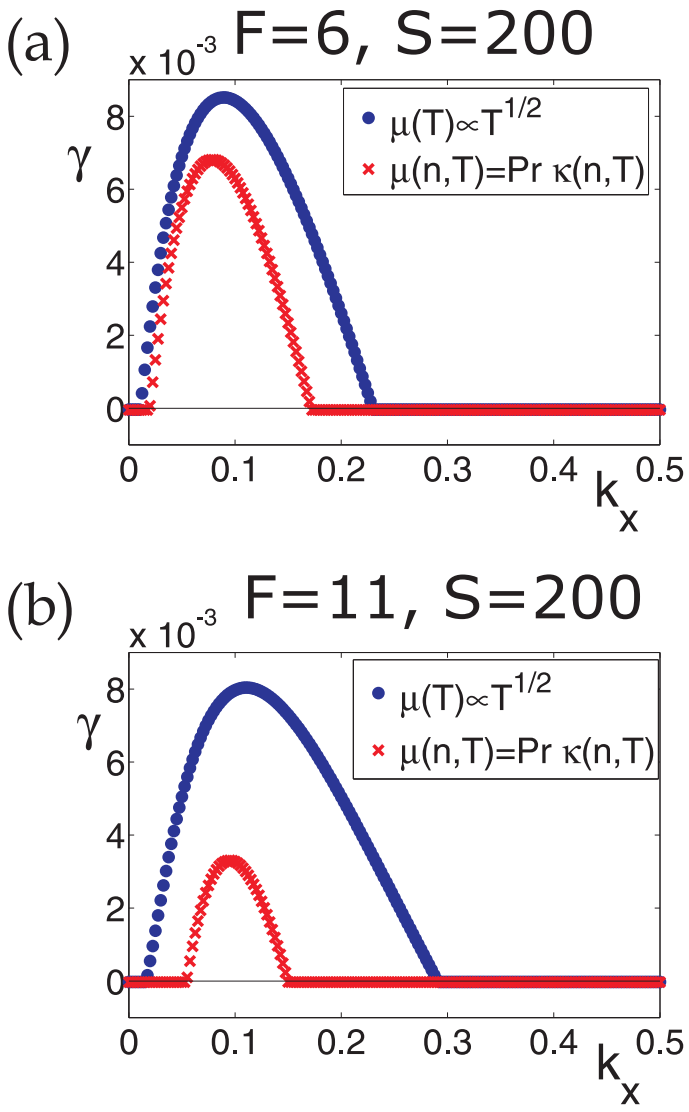

Figure 4.13: Theory: Influence of the choice for the shear viscosity μ on the growth rate $\gamma(k_x)$ for two Leidenfrost states at the same shaking strength $S = 200$: (a) For $F = 6$ layers the region of instability of the Leidenfrost state is significantly reduced by going from the expression for $\mu(T)$ by Brey *et al.* [Eq. (4.72), blue dots] to $\mu(n,T)$ as defined by Eq. (4.75) with Pr $= 1.7$ [red crosses]. (b) For $F = 11$ layers the stabilizing effect is even stronger. Note that the range of unstable k_x-values for the blue dots has increased compared to the $F = 6$ Leidenfrost state, whereas the opposite is true for red crosses.

4.8 Appendix B

For the matrix problem of Eq. (4.62) we need to specify the elements of the matrices **A**, **B**, and **C** of Eqs. (4.63)-(4.65), which contain p, I, and the transport coefficients and their derivatives. These are given below:
First of all, we have the equation of state for the pressure $\widetilde{p}$ and its derivatives:

$$\widetilde{p}_L = \widetilde{n}_L \widetilde{T}_L \frac{1+\widetilde{n}_L}{1-\widetilde{n}_L}, \tag{4.76}$$

$$\frac{\partial \widetilde{p}}{\partial \widetilde{n}}\Big|_L = \widetilde{T}_L \frac{1+2\widetilde{n}_L-\widetilde{n}_L^2}{(1-\widetilde{n}_L)^2}, \tag{4.77}$$

$$\frac{\partial}{\partial \widetilde{y}}\left(\frac{\partial \widetilde{p}}{\partial \widetilde{n}}\Big|_L\right) = \frac{(1-\widetilde{n}_L)(1+2\widetilde{n}_L-\widetilde{n}_L^2)\frac{\partial \widetilde{T}_L}{\partial \widetilde{y}} + 4\widetilde{T}_L \frac{\partial \widetilde{n}_L}{\partial \widetilde{y}}}{(1-\widetilde{n}_L)^3}, \tag{4.78}$$

$$\frac{\partial \widetilde{p}}{\partial \widetilde{T}}\Big|_L = \widetilde{n}_L \frac{1+\widetilde{n}_L}{1-\widetilde{n}_L}, \tag{4.79}$$

$$\frac{\partial}{\partial \widetilde{y}}\left(\frac{\partial \widetilde{p}}{\partial \widetilde{T}}\Big|_L\right) = \left[\frac{1+2\widetilde{n}_L-\widetilde{n}_L^2}{(1-\widetilde{n}_L)^2}\right]\frac{\partial \widetilde{n}_L}{\partial \widetilde{y}} \tag{4.80}$$

The expressions for the energy dissipation rate $\widetilde{I}$ read as follows:

$$\widetilde{I} = \frac{\varepsilon}{\gamma}\frac{\widetilde{n}\widetilde{T}^{3/2}}{\widetilde{\ell}}, \tag{4.81}$$

$$\frac{\partial \widetilde{I}}{\partial \widetilde{n}}\Big|_L = \frac{\varepsilon}{\gamma}\widetilde{T}^{3/2}\left(\frac{\widetilde{\ell}-\widetilde{n}\frac{\partial \widetilde{\ell}}{\partial \widetilde{n}}}{\widetilde{\ell}^2}\right), \tag{4.82}$$

$$\frac{\partial \widetilde{I}}{\partial \widetilde{T}}\Big|_L = \frac{3\varepsilon}{2\gamma}\frac{\widetilde{n}\sqrt{\widetilde{T}}}{\widetilde{\ell}}. \tag{4.83}$$

The mean free path $\widetilde{\ell}$ and its derivatives are given by:

$$\widetilde{\ell} = \sqrt{\frac{3}{32}}\left[\frac{1}{\widetilde{n}}\left(\frac{1-\widetilde{n}}{1-a\widetilde{n}}\right)\right], \tag{4.84}$$

$$\frac{\partial \widetilde{\ell}}{\partial \widetilde{n}} = \sqrt{\frac{3}{32}}\left(\frac{-a\widetilde{n}^2+2a\widetilde{n}-1}{\widetilde{n}^2(1-a\widetilde{n})^2}\right), \tag{4.85}$$

$$\frac{\partial^2 \widetilde{\ell}}{\partial \widetilde{n}^2} = 2\sqrt{\frac{3}{32}}\left(\frac{-a^2\widetilde{n}^3+3a^2\widetilde{n}^2-3a\widetilde{n}+1}{\widetilde{n}^3(1-a\widetilde{n})^3}\right). \tag{4.86}$$

We continue with the transport coefficient for the thermal conductivity $\widetilde{\kappa}$ and its derivatives:

$$\widetilde{\kappa}_L = \frac{\left(\alpha\widetilde{\ell}+1\right)^2}{\widetilde{\ell}}\widetilde{n}\sqrt{\widetilde{T}}, \tag{4.87}$$

$$\frac{\partial\widetilde{\kappa}_L}{\partial\widetilde{y}} = \frac{\partial\widetilde{\kappa}_L}{\partial\widetilde{n}}\frac{\partial\widetilde{n}}{\partial\widetilde{y}}+\frac{\partial\widetilde{\kappa}_L}{\partial\widetilde{T}}\frac{\partial\widetilde{T}}{\partial\widetilde{y}}, \tag{4.88}$$

$$\frac{\partial\widetilde{\kappa}}{\partial\widetilde{n}}\Big|_L = \sqrt{T}\left[\frac{(\alpha\widetilde{\ell}+1)^2}{\widetilde{\ell}}+\widetilde{n}\frac{\alpha^2\widetilde{\ell}^2-1}{\widetilde{\ell}^2}\frac{\partial\widetilde{\ell}}{\partial\widetilde{n}}\right], \tag{4.89}$$

$$\frac{\partial}{\partial\widetilde{y}}\left(\frac{\partial\widetilde{\kappa}}{\partial\widetilde{n}}\Big|_L\right) = \frac{\partial}{\partial\widetilde{n}}\left(\frac{\partial\widetilde{\kappa}}{\partial\widetilde{n}}\Big|_L\right)\frac{\partial\widetilde{n}}{\partial\widetilde{y}}+\frac{\partial}{\partial\widetilde{T}}\left(\frac{\partial\widetilde{\kappa}}{\partial\widetilde{n}}\Big|_L\right)\frac{\partial\widetilde{T}}{\partial\widetilde{y}}, \tag{4.90}$$

$$\frac{\partial}{\partial\widetilde{n}}\left(\frac{\partial\widetilde{\kappa}}{\partial\widetilde{n}}\Big|_L\right) = \sqrt{\widetilde{T}}\left[\frac{2(\alpha^2\widetilde{\ell}^2-1)\frac{\partial\widetilde{\ell}}{\partial\widetilde{n}}+\frac{2\widetilde{n}}{\widetilde{\ell}}\left(\frac{\partial\widetilde{\ell}}{\partial\widetilde{n}}\right)^2+\widetilde{n}(\alpha^2\widetilde{\ell}^2-1)\frac{\partial^2\widetilde{\ell}}{\partial\widetilde{n}^2}}{\widetilde{\ell}^2}\right] \tag{4.91}$$

$$\frac{\partial}{\partial\widetilde{T}}\left(\frac{\partial\widetilde{\kappa}}{\partial\widetilde{n}}\Big|_L\right) = \frac{1}{2\sqrt{\widetilde{T}}}\left[\frac{(\alpha\widetilde{\ell}+1)^2}{\widetilde{\ell}}+\widetilde{n}\frac{\alpha^2\widetilde{\ell}^2-1}{\widetilde{\ell}^2}\frac{\partial\widetilde{\ell}}{\partial\widetilde{n}}\right], \tag{4.92}$$

$$\frac{\partial\widetilde{\kappa}}{\partial\widetilde{T}}\Big|_L = \frac{1}{2\sqrt{\widetilde{T}_L}}\widetilde{n}\frac{(\alpha\widetilde{\ell}+1)^2}{\widetilde{\ell}}, \tag{4.93}$$

$$\frac{\partial}{\partial\widetilde{y}}\left(\frac{\partial\widetilde{\kappa}}{\partial\widetilde{T}}\Big|_L\right) = \frac{\partial}{\partial\widetilde{n}}\left(\frac{\partial\widetilde{\kappa}}{\partial\widetilde{T}}\Big|_L\right)\frac{\partial\widetilde{n}}{\partial\widetilde{y}}+\frac{\partial}{\partial\widetilde{T}}\left(\frac{\partial\widetilde{\kappa}}{\partial\widetilde{T}}\Big|_L\right)\frac{\partial\widetilde{T}}{\partial\widetilde{y}}, \tag{4.94}$$

$$\frac{\partial}{\partial\widetilde{n}}\left(\frac{\partial\widetilde{\kappa}}{\partial\widetilde{T}}\Big|_L\right) = \frac{1}{2\sqrt{\widetilde{T}}}\left[\frac{(\alpha\widetilde{\ell}+1)^2}{\widetilde{\ell}}+\widetilde{n}\frac{\alpha^2\widetilde{\ell}^2-1}{\widetilde{\ell}^2}\frac{\partial\widetilde{\ell}}{\partial\widetilde{n}}\right], \tag{4.95}$$

$$\frac{\partial}{\partial\widetilde{T}}\left(\frac{\partial\widetilde{\kappa}}{\partial\widetilde{T}}\Big|_L\right) = -\frac{1}{4\widetilde{T}\sqrt{\widetilde{T}}}\widetilde{n}\frac{(\alpha\widetilde{\ell}+1)^2}{\widetilde{\ell}}. \tag{4.96}$$

Finally, we have the constitutive relation for the shear viscosity $\widetilde{\mu}$, which is related to κ via the Prandtl number Pr:

$$\widetilde{\mu}_L = \mathrm{Pr}\,\widetilde{\kappa}_L, \tag{4.97}$$

$$\frac{\partial\widetilde{\mu}_L}{\partial\widetilde{y}} = \mathrm{Pr}\frac{\partial\widetilde{\kappa}_L}{\partial\widetilde{y}}, \tag{4.98}$$

and the second viscosity $\widetilde{\lambda}$:

$$\widetilde{\lambda}_L = -\frac{2}{3}\mathrm{Pr}\,\widetilde{\kappa}_L, \tag{4.99}$$

$$\frac{\partial\widetilde{\lambda}_L}{\partial\widetilde{y}} = -\frac{2}{3}\mathrm{Pr}\,\frac{\partial\widetilde{\kappa}_L}{\partial\widetilde{y}}. \tag{4.100}$$

Acknowledgment: We would like to thank Robert Bos for performing many of the experiments presented in this paper.

References

[1] C. Normand, Y. Porneau, and M. G. Velarde, *Convective instability: A physicist's approach*, Rev. Mod. Phys. **49**, 581 (1977).

[2] J. Swift and P. C. Hohenberg, *Hydrodynamic fluctuations at the convective instability*, Phys. Rev. E **15**, 319 (1977).

[3] E. Bodenschatz, W. Pesch, and G. Ahlers, *Recent developments in Rayleigh-Bénard convection*, Annu. Rev. Fluid Mech **32**, 709 (2000).

[4] J. L. Rogers, M. F. Schatz, J. L. Bougie, and J. B. Swift, *Rayleigh-Bénard convection in a vertically oscillated fluid layer*, Phys. Rev. Lett. **84**, 87 (2000).

[5] A. S. Bormann, *The onset of convection in the Rayleigh-Bénard problem for compressible fluids*, Cont. Mech. Thermodyn. **13**, 9 (2001).

[6] J. Oh and G. Ahlers, *Thermal-noise effect on the transition to Rayleigh-Bénard convection*, Phys. Rev. Lett. **91**, 094501 (2003).

[7] I. Mutabazi, E. Guyon, and J. E. Wesfreid, *Dynamics of Spatio-Temporal Cellular Structures, Henri Bénard Centenary Review*, vol. 207 (Springer, New York, 2006).

[8] P. Eshuis, K. van der Weele, D. van der Meer, R. Bos, and D. Lohse, *Phase diagram of vertically shaken granular matter*, Phys. Fluids **19**, 123301 (2007).

[9] Y. Du, H. Li, and L. P. Kadanoff, *Breakdown of hydrodynamics in a one-dimensional system of inelastic particles*, Phys. Rev. Lett. **74**, 1268 (1995).

[10] L. P. Kadanoff, *Built upon sand: Theoretical ideas inspired by granular flows*, Rev. Mod. Phys. **71**, 435 (1999).

[11] J. Duran, *Sand, Powders and Grains: An Introduction to the Physics of Granular Materials* (Springer-Verlag, New-York, 1999).

[12] I. Goldhirsch, *Rapid granular flows*, Annu. Rev. Fluid Mech. **35**, 267 (2003).

[13] I. S. Aranson and L. S. Tsimring, *Patterns and collective behavior in granular media: Theoretical concepts*, Rev. Mod. Phys. **78**, 641 (2006).

[14] E. Clément and J. Rajchenbach, *Fluidization of a bidimensional powder*, Europhys. Lett. **16**, 133 (1991).

[15] J. A. C. Gallas, H. J. Herrmann, and S. Sokolowski, *Convection cells in vibrating granular media*, Phys. Rev. Lett. **69**, 1371 (1992).

[16] Y.-h. Taguchi, *New origin of a convective motion: Elastically induced convection in granular materials*, Phys. Rev. Lett. **69**, 1367 (1992).

[17] J. B. Knight, H. M. Jaeger, and S. R. Nagel, *Vibration-induced size separation in granular media: The convection connection*, Phys. Rev. Lett. **70**, 3728 (1993).

[18] S. Luding, E. Clément, A. Blumen, J. Rajchenbach, and J. Duran, *The onset of convection in molecular dynamics simulations of grains*, Phys. Rev. E **50**, R1762 (1994).

[19] H. Hayakawa, S. Yue, and D. C. Hong, *Hydrodynamic description of granular convection*, Phys. Rev. Lett. **75**, 2328 (1995).

[20] E. E. Ehrichs, H. M. Jaeger, G. S. Karczmar, J. B. Knight, V. Y. Kuperman, and S. R. Nagel, *Granular convection observed by magnetic resonance imaging*, Science **267**, 1632 (1995).

[21] M. Bourzutschky and J. Miller, *Granular convection in a vibrated fluid*, Phys. Rev. Lett. **74**, 2216 (1995).

[22] K. M. Aoki, T. Akiyama, Y. Maki, and T. Watanabe, *Convective roll patterns in vertically vibrated beds of granules*, Phys. Rev. E **54**, 874 (1996).

[23] J. B. Knight, E. E. Ehrichs, V. Y. Kuperman, J. K. Flint, H. M. Jaeger, and S. R. Nagel, *Experimental study of granular convection*, Phys. Rev. E **54**, 5726 (1996).

[24] Y. Lan and A. D. Rosato, *Convection related phenomena in granular dynamics simulations of vibrated beds*, Phys. Fluids **9**, 3615 (1997).

[25] K. M. Aoki and T. Akiyama, *Control parameter in granular convection*, Phys. Rev. E **58**, 4629 (1998).

[26] C. Bizon, M. D. Shattuck, J. B. Swift, W. D. McCormick, and H. L. Swinney, *Patterns in 3d vertically oscillated granular layers: Simulation and experiment*, Phys. Rev. Lett. **80**, 57 (1998).

[27] R. Ramírez, D. Risso, and P. Cordero, *Thermal convection in fluidized granular systems*, Physical Review Letters **85**, 1230 (2000).

[28] S. S. Hsiau and C. H. Chen, *Granular convection cells in a vertical shaker*, Powder Technology **111**, 210 (2000).

[29] R. D. Wildman, J. M. Huntley, and D. J. Parker, *Convection in highly fluidized three-dimensional granular beds*, Phys. Rev. Lett. **86**, 3304 (2001).

[30] P. Sunthar and V. Kumaran, *Characterization of the stationary states of a dilute vibrofluidized granular bed*, Phys. Rev. E **64**, 041303 (2001).

[31] X. He, B. Meerson, and G. Doolen, *Hydrodynamics of thermal granular convection*, Phys. Rev. E **65**, 030301 (2002).

[32] A. Garcimartin, D. Maza, J. L. Ilquimiche, and I. Zuriguel, *Convective motion in a vibrated granular layer*, Phys. Rev. E **65**, 031303 (2002).

[33] J. Talbot and P. Viot, *Wall-enhanced convection in vibrofluidized granular systems*, Phys. Rev. Lett. **89**, 064301 (2002).

[34] S. S. Hsiau, P. C. Wang, and C. H. Tai, *Convection cells and segregation in a vibrated granular bed*, AIChE J. **48**, 1430 (2002).

[35] T. Ohtsuki and T. Ohsawa, *Hydrodynamics for convection in vibrating beds of cohesionless granular materials*, J. Phys. Soc. Jpn. **72**, 1963 (2003).

[36] P. Cordero, R. Ramirez, and D. Risso, *Buoyancy driven convection and hysteresis in granular gases: Numerical solution*, Physica A **327**, 82 (2003).

[37] G. Miao, K. Huang, Y. Yun, and R. Wei, *Active thermal convection in vibrofluidized granular systems*, Eur. Phys. J. B **40**, 301 (2004).

[38] C. H. Tai and S. S. Hsiau, *Dynamics behaviors of powders in a vibrating bed*, Powder Technology **139**, 221 (2004).

[39] D. Risso, R. Soto, S. Godoy, and P. Cordero, *Friction and convection in a vertically vibrated granular system*, Phys. Rev. E **72**, 011305 (2005).

[40] D. Paolotti, A. Barrat, U. M. B. Marconi, and A. Puglisi, *Thermal convection in monodisperse and bidisperse granular gases: A simulations study*, Phys. Rev. E **69**, 061304 (2004).

[41] E. Khain and B. Meerson, *Onset of thermal convection in a horizontal layer of granular gas*, Phys. Rev. E **67**, 021306 (2003).

[42] P. Eshuis, K. van der Weele, D. van der Meer, and D. Lohse, *Granular Leidenfrost effect: Experiment and theory of floating particle clusters*, Phys. Rev. Lett. **95**, 258001 (2005).

[43] M. P. Allen and D. J. Tildesley, *Computer Simulation of Liquids* (Oxford University Press, Oxford, 1987).

[44] D. C. Rapaport, *The Art of Molecular Dynamics Simulation* (Cambridge University Press, Cambridge, 1995).

[45] H. J. Herrmann, J.-P. Hovi, and S. Luding (Eds.), *Physics of dry granular media - NATO ASI Series E 350* (Kluwer Academic Publishers, Dordrecht, 1998).

[46] P. A. Vermeer, S. Diebels, W. Ehlers, H. J. Herrmann, S. Luding, and E. Ramm (Eds.), *Continuous and Discontinuous Modelling of Cohesive Frictional Materials* (Springer, Berlin, 2001), Lecture Notes in Physics 568.

[47] M. Lätzel, S. Luding, H. J. Herrmann, D. W. Howell, and R. P. Behringer, *Comparing simulation and experiment of a 2D granular Couette shear device*, Eur. Phys. J. E **11**, 325 (2003).

[48] S. Luding, *Micro-macro transition for anisotropic, frictional granular packings*, Int. J. Sol. Struct. **41**, 5821 (2004).

[49] S. Luding, *Molecular dynamics simulations of granular materials*, in *The Physics of Granular Media*, edited by H. Hinrichsen and D. E. Wolf, 299–324 (Wiley VCH, Weinheim, Germany, 2004).

[50] S. Luding, *About contact force-laws for cohesive frictional materials in 2D and 3D*, in *Behavior of Granular Media*, edited by P. Walzel, S. Linz, Ch. Krülle, and R. Grochowski, 137–147 (Shaker Verlag, 2006), Band 9, Schriftenreihe Mechanische Verfahrenstechnik, ISBN 3-8322-5524-9.

[51] S. Luding, *Cohesive frictional powders: Contact models for tension*, Granular Matter **10**, in press (2008), accepted.

[52] Determining the number of layer F for the MD simulations from the number of particles in the system N depends on the particle configuration used for the calculation: Assuming a square-lattice configuration one finds $F_{\text{square}} = Nd^2/(LD) = 7.4$ and 11.1 for $N = 7467$ and $N = 11200$ respectively. For a perfect hexagonal close-packing the corresponding F-values will be smaller. Therefore we will refer to these

situations as $F = 6$ and $F = 11$ evn though the determination of F from the simulations is not straightforward or unique. This arbitrary choice for the number of layers maybe a reason for the qualitative difference between numerics and experiment, but does not explain the extent of the deviation.

[53] T. Pöschel and T. Schwager, *Computational Granular Dynamics* (Springer, Berlin, 2005).

[54] S. Luding, *Collisions & contacts between two particles*, in *Physics of dry granular media - NATO ASI Series E350*, edited by H. J. Herrmann, J.-P. Hovi, and S. Luding, 285 (Kluwer Academic Publishers, Dordrecht, 1998).

[55] S. F. Foerster, M. Y. Louge, H. Chang, and K. Allia, *Measurements of the collision properties of small spheres*, Phys. Fluids **6**, 1108 (1994).

[56] N. V. Brilliantov, F. Spahn, J. M. Hertzsch, and T. Pöschel, *Model for collisions in granular gases*, Phys. Rev. E **53**, 5382 (1996).

[57] S. Chandrasekhar, *Hydrodynamic and Hydromagnetic Stability* (Dover, New-York, 1981).

[58] E. L. Grossman, T. Zhou, and E. Ben-Naim, *Towards granular hydrodynamics in two-dimensions*, Phys. Rev. E **55**, 4200 (1997).

[59] B. Meerson, T. Pöschel, and Y. Bromberg, *Close-packed floating clusters: Granular hydrodynamics beyond the freezing point?*, Phys. Rev. Lett. **91**, 024301 (2003).

[60] J. J. Brey, M. J. Ruiz-Montero, and F. Moreno, *Hydrodynamics of an open vibrated granular system*, Phys. Rev. E **63**, 061305 (2001).

[61] S. A. Orszag, *Accurate solution of the Orr-Sommerfeld stability equation*, J. Fluid Mech. **50**, 689 (1971).

[62] C. Canuto, M. Y. Hussaini, A. Quarteroni, and T. A. Zang, *Spectral methods: Fundamentals in single domains* (Springer, 2006).

[63] M. Alam and P. R. Nott, *Stability of plane Couette flow of a granular material*, J. Fluid Mech. **377**, 99 (1998).

[64] One can also collocate the continuity equation at Gauss-Lobatto points, but that calls for using artificial boundary conditions for the density field that may lead to one spurious eigenvalue [63].

[65] The results of Fig. 4.9 represent experiments with glass beads of $d = 1$ mm. Also for $F = 6.2$ layers of steel beads we found the onset of convection (at $S_{\mathrm{conv}} = 62$) to match the theoretical prediction very well.

5

Granular Hydrodynamics at its Edge: A Horizontal Array of Inelastic Particles

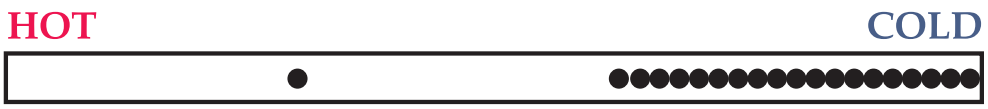

Peter Eshuis, Ko van der Weele, Enrico Calzavarini, Devaraj van der Meer, and Detlef Lohse, *preprint* (2007).

*The one-dimensional granular system introduced by Du, Li, and Kadanoff [Phys. Rev. Lett. **74**, 1268 (1995)] is shown to mark the exact edge of granular hydrodynamics. The density profile of the characteristic steady state, in which a single particle commutes between the driving wall and a dense cluster, is well captured by a hydrodynamic description provided that the finite size of the particles is incorporated. The temperature, however, is not well-described: Since all energy exchange is located at the border of the cluster, it is precisely for this quantity that the continuum approach breaks down.*

(See also the two flip books printed on the bottom of every page, for more details see the beginning of this thesis.)

5.1 Introduction

One of the central themes in the field of granular matter today is the question to what extent the rich variety of experimental phenomena can be captured by hydrodynamic continuum theory. Such a theory can hardly be expected to cover all observed effects [1], the main obstacle being the lack of separation of scales: The size of the granular particles is not negligible compared to the system size. This is a serious limitation to any continuum theory, especially for the small-scale phenomena. For large-scale collective effects, however, hydrodynamic modelling is a natural approach [2, 3] and has been successfully applied to a large number of phenomena ranging from cluster formation in various granular gases [4–6] to convection rolls in a vibrated granular bed [7], the fluid-like impact of a steel ball on sand [8], and the granular Leidenfrost effect [9], see Ch. 3 of this thesis.

A very illustrative example in this context was introduced in 1995 by Du, Li, and Kadanoff [10]. It consists of N inelastically colliding particles confined to a horizontal tube [Fig. 5.1(a)] driven at the left wall: A random velocity is given to the leftmost particle every time it hits this wall. The right wall is insulating, i.e., the collisions of the rightmost particle with this wall are fully elastic.

Starting out from a homogeneous distribution, the particles are seen to cluster at the right wall [Fig. 5.1(b)]. All particles get caught in the cluster, except the leftmost particle, which keeps travelling back and forth between the hot wall and the cluster [10, 11]. Clearly, there is no equipartition of energy: A dilute region consisting of one fast particle coexists with a dense region of slow particles. A typical time-averaged density and temperature distribution are shown

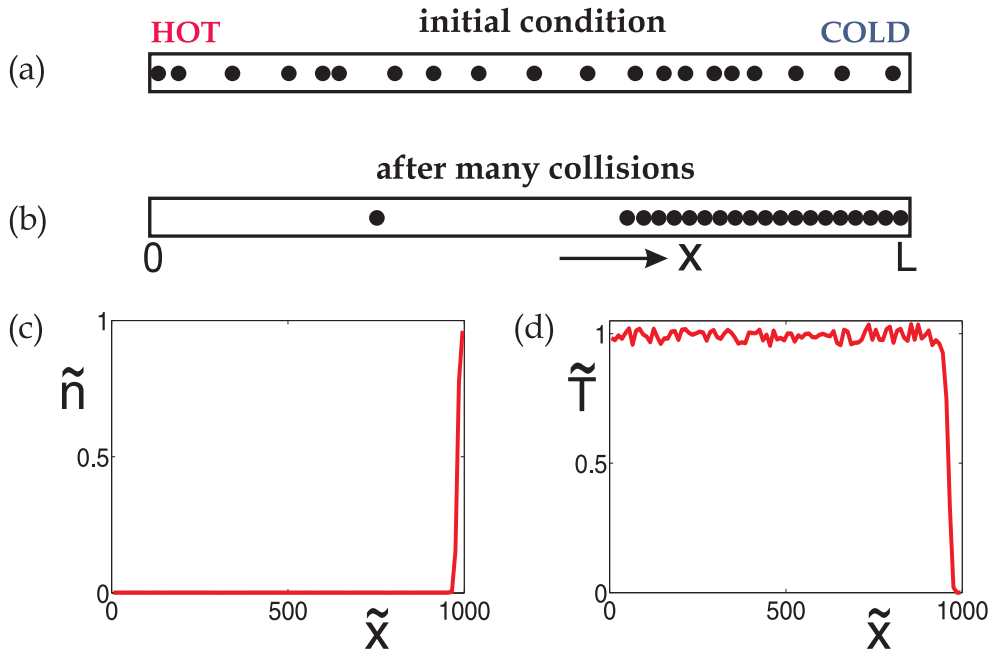

Figure 5.1: (a) Initial condition of a Molecular Dynamics (MD) simulation with $N = 20$ identical particles, diameter d, randomly distributed over the tube length L. Every time the leftmost particle hits the left wall it is given a random velocity. The collisions of the rightmost particle with the right wall are elastic. (b) After many inelastic collisions: A cluster of slow particles is kept close to the right wall by one relatively fast particle commuting between the hot wall and the cluster. (c) Time-averaged number density $\widetilde{n}(\widetilde{x})$ of the steady state and (d) the corresponding granular temperature $\widetilde{T}(\widetilde{x})$ for $L = 1000d$. (The tilde above $\widetilde{x}$, $\widetilde{n}$ and $\widetilde{T}$ indicates that these are dimensionless quantities that will be introduced in Sec. 5.3.)

in Fig. 5.1(c) and 5.1(d). Du *et al.* [10] demonstrated that the "simplest hydrodynamic approach", treating the system as an ideal gas of sizeless particles with energy dissipation (from the particle collisions), fails to correctly describe this state.

What is the reason for this failure? As it turns out, the crucial point is that the individual left particle has no way of establishing a continuous energy exchange along its path. It therefore does not form a gas in the hydrodynamic sense, but rather a Knudsen gas, which is so dilute that the particle collisions within the gas can be ignored in comparison with the collisions with the boundaries.

We will show that hydrodynamics is able to capture the density throughout

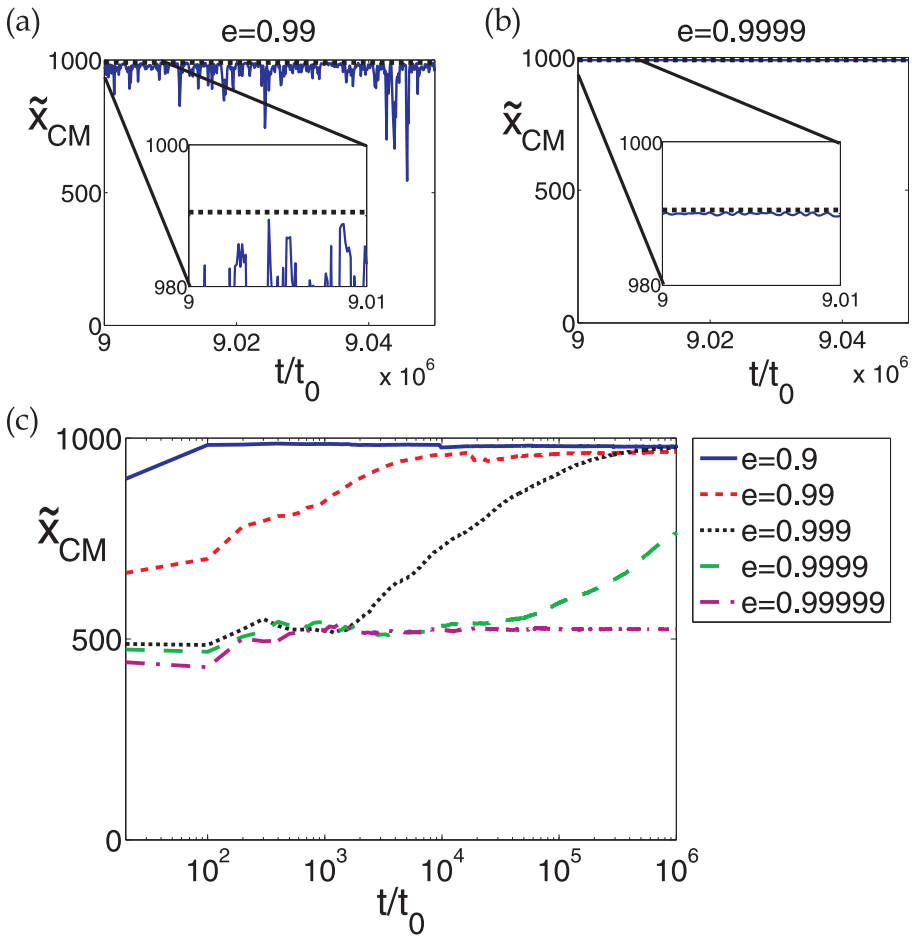

Figure 5.2: (a) Position of the cluster's center of mass, $\widetilde{x}_{\rm CM}(t) = x_{\rm CM}/d$, as a function of time (normalized by $t_0 = L\sqrt{m/T_0}$) for a MD simulation with $N = 20$ particles and a restitution coefficient $e = 0.99$. The cluster occasionally expands and re-compacts; the expansions occur when the left particle picks up a particularly small velocity from the hot wall. The dotted line (see also inset) marks the maximal value of $x_{\rm CM} = L - d(N-1)/2$ corresponding to a close-packed cluster in a tube of length $L = 1000d$. (b) For a higher restitution coefficient, $e = 0.9999$, $x_{\rm CM}$ stays much closer to this maximal value. (c) The running average of the cluster's center of mass position, sampled every 100 time units, for a series of MD simulations with $N = 20$ particles starting out from the same initial conditions. The curves correspond to various restitution coefficients, showing the transient time the system needs to reach the steady state in which the commuting particle keeps the cluster of particles at the right wall.

the system (if the excluded volume is properly accounted for), but *not* the energy profile. Therefore this one-dimensional system indicates the exact point where the continuum theory breaks down and, moreover, the reason why. This greatly enhances the significance of this system: It is not just an example in which hydrodynamics fails, but it actually marks the *precise edge* of granular hydrodynamics.

The individual behavior of the leftmost particle does not only cause the breakdown of hydrodynamics in this region, but also triggers an interesting phenomenon [Fig. 5.2(a)]: Once in a while this particle gets a particularly small velocity from the hot wall, giving the cluster time to expand. The extent of the expansion is controlled by the restitution coefficient e, see Fig. 5.2(b). Approaching the elastic limit ($e \to 1$) means that the time needed to get a converged simulation increases rapidly as shown by Fig. 5.2(c). In fact, in the limit $e = 1$ the system never develops a cluster and $\widetilde{x}_{\mathrm{CM}}$ keeps fluctuating around its mean value 500 $(= L/2)$ forever.

When the steady state is eventually reached for $e < 1$, the cluster consists of particles moving only slowly. For increasing restitution coefficient the particles in the cluster become slower, causing the amplitude of the occasional expansions to decrease [see Fig. 5.2(b)].

After each expansion, it takes a large number of collisions to force the cluster back to its ordinary size and density again. This intermittent expansion of the cluster has been treated in detail in Refs. [10, 12]; in our time-averaged continuum description it only shows up as a slight smoothening of the density profile around the boundary between the dilute region and the cluster, as demonstrated in Fig. 5.3(c). This boundary region for the theoretical density profiles becomes wider when $e \to 1$, whereas for the MD simulations of Fig. 5.3(a,b) the boundary region becomes narrower. This behavior of the MD simulations can be understood as follows: The inelasticity causes the velocity distribution of the cluster particles to show some spread, which decreases when the system becomes more elastic [13]. This dispersion in the particle velocities accounts for the smaller amplitude of the occasional expansions mentioned above and thereby also for the fact that the transition region becomes smaller in the MD simulations as $e \to 1$. In the elastic limit ($e = 1$) the profiles for the density and temperature are uniform both in MD and in the hydrodynamic model. For the MD simulations this means that the limit $e \to 1$ shows a distinct discontinuity. By contrast, in the hydrodynamic model the behavior for this limit is a gradual one; the effect of dispersion in particle velocities (which causes the discontinuity in the MD limit) is not described by the model.

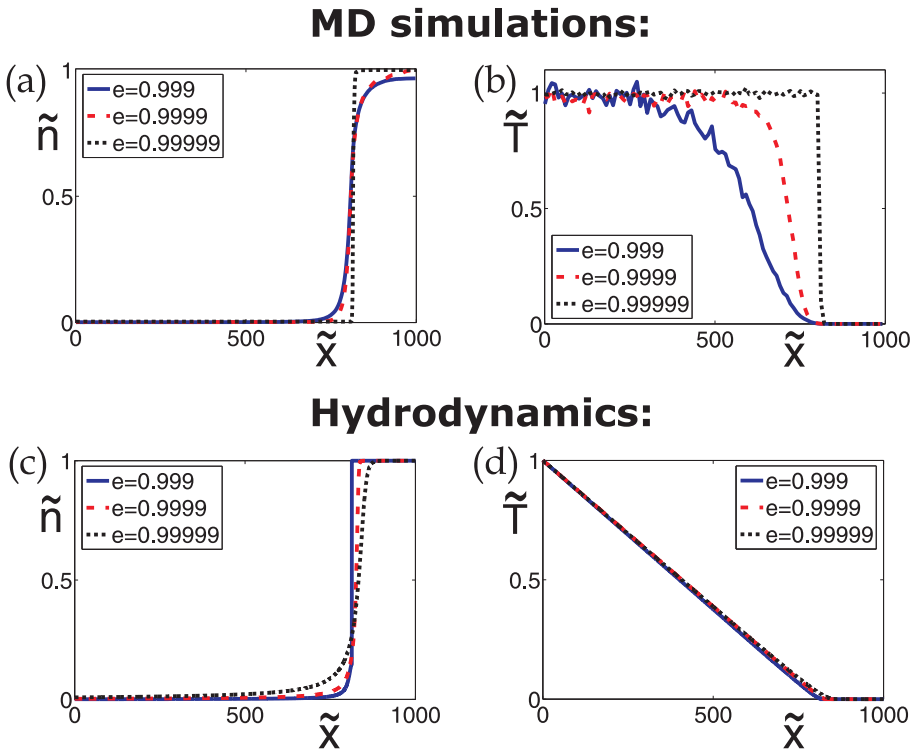

Figure 5.3: MD vs. Hydrodynamics in the near elastic limit for $N = 187$ particles in a tube of length $L = 1000d$: (a,b) The time-averaged dimensionless number density $\widetilde{n}(\widetilde{x})$ and granular temperature $\widetilde{T}(\widetilde{x})$ obtained from MD simulations (in the steady state) for three different values of restitution coefficient e. The total duration of the simulations was $t/t_0 = 5 \cdot 10^7$ and we sampled every 100 time units. (c,d) The density $\widetilde{n}(\widetilde{x})$ and temperature $\widetilde{T}(\widetilde{x})$ from hydrodynamic theory (see Sec. 5.3).

5.2 Molecular Dynamics simulations

We use an event-driven Molecular Dynamics (MD) code, in which N identical particles of diameter d and unit mass m collide inelastically [14]. The velocities after each collision are related to those before the collision (see Fig. 5.4) by the following two rules:

$$v_1' = \frac{1}{2}[v_1(1-e)+v_2(1+e)] \tag{5.1}$$

$$v_2' = \frac{1}{2}[v_1(1+e)+v_2(1-e)] \tag{5.2}$$

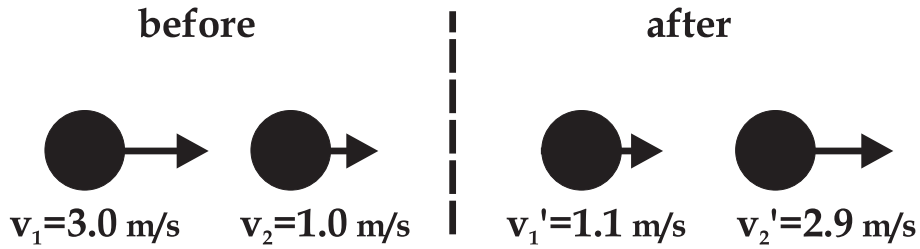

Figure 5.4: Inelastic collision of two identical particles. The initial and final velocities are indicated: Their sum is constant ($v_1 + v_2 = v_1' + v_2'$), expressing momentum conservation, whereas the difference becomes smaller and defines the restitution coefficient $e = -(v_2' - v_1')/(v_2 - v_1) = 0.9$.

They are derived from the conservation of momentum ($v_1' + v_2' = v_1 + v_2$) together with the definition of e, the coefficient of restitution: $v_1' - v_2' = -e(v_1 - v_2)$. If $e = 1$ the collisions are fully elastic, but we will consider only the inelastic case $e < 1$, in which the particles lose a fraction $\varepsilon = (1 - e^2)$ of their kinetic energy in every collision. In order to avoid inelastic collapse (an infinite number of collisions in a finite time [10, 15]) we choose $N\varepsilon < 1$.

The left wall is hot: It drives the leftmost particle by giving it a random velocity from a linearly corrected Gaussian distribution $v_0 \exp(-v_0^2/2T_0)$ [16]. The linear pre-factor v_0 corrects for the fact that a very small velocity lives longer in the system than a fast one (and thus has a larger influence on the time average); it ensures that the ensemble of all N particles acquires a time-averaged velocity distribution that is purely Gaussian in the elastic case ($e = 1$). In order to minimize the transient time before this distribution establishes itself, we initially put the particles at random positions in the tube and give each of them a random velocity picked from the same distribution as we use at the hot wall.

The value of T_0 (the granular temperature of the hot wall) gives the width of the velocity distribution offered to the leftmost particle, i.e., the strength of the driving. The temperature is defined by $\frac{1}{2}k_B T = \frac{1}{2}m(\langle v^2\rangle - \langle v\rangle^2)$ with $k_B = 1$ (the standard choice for granular systems, giving T the dimensions of energy) and unit mass m.

The right wall is insulating: The collisions of the rightmost particle with this wall are perfectly elastic, so no energy is dissipated here.

Figure 5.1 shows the result of a typical MD simulation with $N = 20$ particles. Steady state profiles for higher values of N are depicted in Fig. 5.3 and 5.5. The density and the temperature profiles immediately reveal the inelastic nature of the

collisions. In the elastic case ($e = 1$) both would simply be constant throughout the tube as mentioned above.

The qualitative features of the system are not too sensitive to the precise values of the control parameters N and the inelasticity ε, provided that $N \geq 2$, $\varepsilon > 0$, and $N\varepsilon < 1$. Even for $N = 2$, the steady state is found to consist of one commuting particle and one particle that remains close to the right wall [12]. With respect to the third control parameter T_0 (the driving strength), one may anticipate that above some critical value $T_{0,\mathrm{crit}}$ (depending on N and ε) the dissipation due to the collisions in the system will be overpowered and the cluster is fluidized [17]. Here we do not consider such high T_0-values; our system always shows a coexistence of 1 travelling particle and $N-1$ cluster particles.

5.3 Hydrodynamics of the steady state

We consider the steady state of the system. This means that the full hydrodynamic problem [which would involve a number density $n(x,t)$, velocity field $u(x,t)$, and granular temperature $T(x,t)$] here reduces to finding the two time-independent quantities $n = n(x)$ and $T = T(x)$, while $u \equiv 0$. To achieve this, we use three hydrodynamics equations plus boundary conditions.

We go beyond the ideal-gas description by incorporating the finite size of the particles (via the constitutive relations [18]) and also the dissipation due to the collisions. This is in the same spirit as we did for the granular Leidenfrost effect [9], see Ch. 3, an analogous clustering phenomenon in a 2D vertical system.

The first hydrodynamic equation is the *momentum balance* [19]:

$$\frac{dp}{dx} = 0, \tag{5.3}$$

where p is the pressure. It immediately follows that p is constant throughout the tube. Its value is determined by the second equation in our model, the *equation of state*:

$$p = \frac{nT}{1-nd} = \frac{nT}{1-n/n_c}. \tag{5.4}$$

Here n_c is the maximal number density (i.e., the number of particles per unit length in the close-packed case, $n_c = 1/d$). In Eq. (5.4) one recognizes the ideal gas law $p = NT/L = nT$ with a VanderWaals correction for the excluded length due to the finite size of the particles, i.e., the free space within the tube is not L but $L - Nd$. This 1D equation of state [20] is slightly different from the one we

used for the granular Leidenfrost effect, which was especially designed for a 2D system [9, 21]. It also differs from the ideal gas law used as the equation of state by Du *et al.* [10], since they used sizeless particles.

The third hydrodynamic equation is the *energy balance*, expressing the steady state equilibrium between the heat flux through the array of particles and the dissipation due to the inelastic collisions:

$$-\frac{d\Phi(x)}{dx} = I(x). \tag{5.5}$$

Here $\Phi(x) = -\kappa(x)dT/dx$ is the heat flux (from high to low temperatures, hence the minus sign), with $\kappa(x)$ the thermal conductivity allowing for finite size effects:

$$\kappa(x) = C_1\frac{T^{1/2}(x)}{n(x)\ell(x)} = C_1\frac{T^{1/2}(x)}{1-n(x)/n_c}. \tag{5.6}$$

Here C_1 is a constant and $\ell(x)$ denotes the local mean free path, which is related to the number density as $n(x) = 1/[d+\ell(x)]$, or equivalently $\ell(n(x)) = [1-n(x)/n_c]/n(x)$. The dimensionless mean free path $\ell(x)/d = [1-n(x)/n_c]/[n(x)/n_c]$, called the Knudsen number, is very large in the dilute region and vanishingly small within the cluster. Note that Du *et al.* used $\kappa(x) \propto T^{1/2}(x)$ for the thermal conductivity [10].

In Eq. (5.5) the dissipation rate I (per unit length and per unit time) is given by:

$$I(x) = C_2\varepsilon\frac{n(x)}{\ell(x)}T^{3/2}(x) = C_2\varepsilon\frac{n^2(x)T^{3/2}(x)}{1-n(x)/n_c}, \tag{5.7}$$

with C_2 a constant. The expression for I is equal to the energy loss in one collision ($\propto \varepsilon T$) multiplied by the total number of collisions per unit time taking into account excluded volume ($\propto n\sqrt{T}/\ell$) [21]. Du *et al.* used the low density limit of Eq. (5.7) for the dissipation rate, i.e., $I(x) \propto \varepsilon n^2(x)T^{3/2}(x)$ [10].

The set of three hydrodynamic equations (5.3)-(5.5) is complemented by three boundary conditions: (i) The imposed granular temperature at the hot wall $T(0) = T_0$, (ii) vanishing heat flux at the insulating wall $\Phi(L) = 0$, and (iii) conservation of particles $\int_0^L n(x)dx = N$.

Now let us introduce dimensionless variables:

$$\widetilde{n} = \frac{n}{n_c}, \quad \widetilde{T} = \frac{T}{T_0}, \quad \widetilde{x} = \frac{x}{d}. \tag{5.8}$$

The force balance (5.3) and the equation of state (5.4), combined into one, then read:

$$\widetilde{p} = \frac{\widetilde{n}\widetilde{T}}{1-\widetilde{n}} = \text{constant} = \widetilde{p}_0, \tag{5.9}$$

the energy balance (5.5) becomes (with $C = C_2/C_1$):

$$-\frac{d\widetilde{\Phi}}{d\widetilde{x}} = C\varepsilon\frac{\widetilde{n}^2\widetilde{T}^{3/2}}{1-\widetilde{n}}\ , \text{ where } \widetilde{\Phi} = \frac{-\widetilde{T}^{1/2}}{(1-\widetilde{n})}\frac{d\widetilde{T}}{d\widetilde{x}}, \tag{5.10}$$

and the dimensionless boundary conditions are:

$$\widetilde{T}(0) = 1, \quad \widetilde{\Phi}(L/d) = 0, \quad \int_0^{L/d} \widetilde{n} d\widetilde{x} = N. \tag{5.11}$$

One thus arrives at a problem consisting of two first-order differential equations [see Eq. (5.10)] and three unknown quantities $\widetilde{n}$, $\widetilde{T}$ and $\widetilde{\Phi}$. We use Eq. (5.9) to express $\widetilde{n}$ in terms of $\widetilde{T}$ [22]:

$$\widetilde{n}(\widetilde{T}) = \frac{1}{1-\widetilde{T}(\widetilde{x})[1-1/\widetilde{n}(0)]}, \tag{5.12}$$

and with this the two differential equations to be solved take the form:

$$\frac{d\widetilde{T}}{d\widetilde{x}} = -\frac{[1-\widetilde{n}(\widetilde{T})]\,\widetilde{\Phi}}{\widetilde{T}^{1/2}}, \tag{5.13}$$

$$\frac{d\widetilde{\Phi}}{d\widetilde{x}} = -C\,\varepsilon\,\frac{\widetilde{n}^2(\widetilde{T})\,\widetilde{T}^{3/2}}{1-\widetilde{n}(\widetilde{T})}, \tag{5.14}$$

supplemented by the boundary conditions $\widetilde{T}(0) = 1$ and $\widetilde{\Phi}(L/d) = 0$ [23]. We solve this numerically, varying the shooting parameter $\widetilde{\Phi}(0)$ to fulfill the second boundary condition.

In the process of solving Eqs. (5.13)-(5.14) we find that the heat flux $\widetilde{\Phi}(\widetilde{x})$ vanishes already *before* the right wall. Let us call this point $\widetilde{x} = \widetilde{x}_1$. The temperature $\widetilde{T}(\widetilde{x})$ becomes zero here, and [via Eq. (5.12)] the density $\widetilde{n}(\widetilde{x})$ becomes 1, giving a singularity in the equations (5.13)-(5.14). As a result, the heat flux $\widetilde{\Phi}(\widetilde{x})$ gets negative beyond $\widetilde{x}_1$, as if energy would flow from the cold right side into the system. For our time-averaged quantities this makes no physical sense. So beyond $\widetilde{x}_1$ we fix the heat flux to $\widetilde{\Phi}(\widetilde{x}) = 0$, and hence also the values $\widetilde{T}(\widetilde{x}) = 0$ and $\widetilde{n}(\widetilde{x}) = 1$, which means that the interval between $\widetilde{x}_1$ and the right wall is an immobile, close-packed cluster.

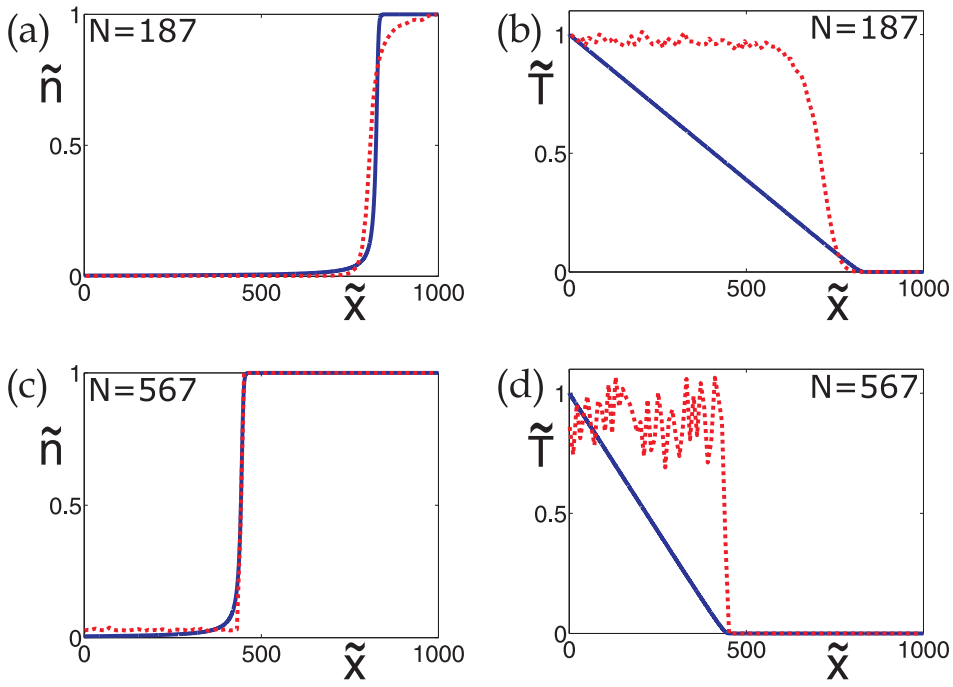

Figure 5.5: Density $\widetilde{n}(\widetilde{x})$ and temperature $\widetilde{T}(\widetilde{x})$ along a tube of length $L = 1000d$ for various numbers of particles: (a,b) $N = 187$ and (c,d) $N = 567$. The restitution coefficient is fixed at $e = 0.9999$. Dashed red curves represent our MD simulations (total duration was $t/t_0 = 5 \cdot 10^7$ with sampling every 100 time units), and solid blue lines the hydrodynamic model (5.13)-(5.14).

Apart from the heat flux itself, also its derivative $d\widetilde{\Phi}/d\widetilde{x}$ is zero at $\widetilde{x}_1$, which means that the transition from the dilute region to the cluster occurs smoothly.

The resulting density and temperature profiles are shown in Fig. 5.3 and 5.5. The agreement with the corresponding MD simulations [exploiting the only fit parameter in our theory, namely the constant C in Eq. (5.14)] is seen to be good regarding the density $\widetilde{n}$. However, the temperature $\widetilde{T}$ is not reproduced well in the dilute region. The model predicts a linear decrease of $\widetilde{T}$, whereas the actual temperature is constant: This is a consequence of the fact that this region contains just *one particle*, which has no way of exchanging energy with other particles until it meets the cluster at $\widetilde{x}_1$. It has a constant velocity (and hence $\widetilde{T}$) along its whole path.

The fact that the energy exchange takes place only at the boundary between the

dilute region and the cluster is illustrated by Fig. 5.6, where we plot the thermal conductivity obtained from the hydrodynamic model:

$$\widetilde{\kappa}(\widetilde{x}) = \frac{\widetilde{T}^{1/2}(\widetilde{x})}{1-\widetilde{n}(\widetilde{T})} = \widetilde{T}^{1/2}(\widetilde{x}) + \frac{\widetilde{n}(0)}{1-\widetilde{n}(0)}\widetilde{T}^{-1/2}(\widetilde{x}) \tag{5.15}$$

versus the mean energy exchange between the particles, $E_{\rm exch}(\widetilde{x})$, determined from the MD simulation. The thermal conductivity shows a pronounced upswing at the boundary $\widetilde{x}_1$. It is also non-zero to the left of this boundary ($\propto \widetilde{T}^{1/2}$, i.e., the ideal-gas behavior for $\widetilde{n} \ll 1$), but this should now be recognized as an artefact of the continuum description: The dilute region is treated as a *hydrodynamic gas*, which - even at low density - is by definition supposed to consist of an ensemble of particles with energy exchange. The actual $\widetilde{\kappa}$ consists of the upswing only. That is, we are dealing with a *Knudsen gas*, i.e., a gas in which only the collisions with the boundaries count. This is confirmed by $E_{\rm exch}(\widetilde{x})$ in the simulations, which in the dilute region shows no energy exchange at all, and a pronounced maximum at the boundary of the cluster $\widetilde{x}_1$. The density inside the cluster steadily grows, see Fig. 5.5(a), and as a result the number of collisions increases in the cluster.

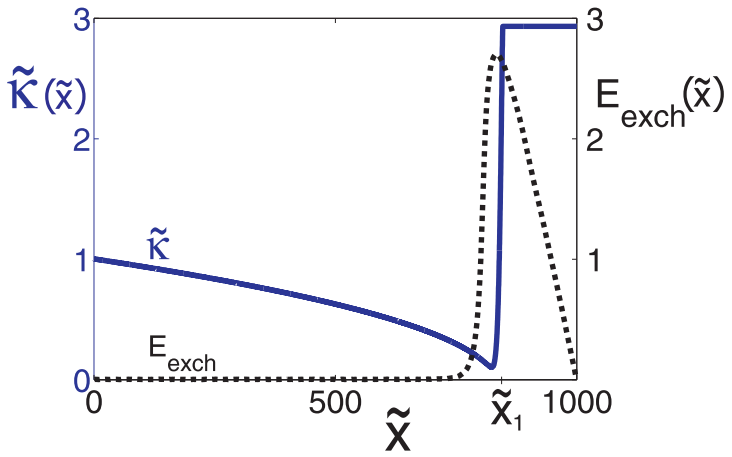

Figure 5.6: Energy transport through the system: Hydrodynamics vs. MD. The energy transport according to the hydrodynamic model is represented by the thermal conductivity $\widetilde{\kappa}(\widetilde{x})$ [solid blue line]; it is calculated via Eq. (5.15) from the hydrodynamic temperature profile for $N = 187$ particles of Fig. 5.5(a,b). The energy transport for the MD simulations is reflected by $E_{\rm exch}(\widetilde{x})$ [dotted black line]. The (mean) energy exchange $E_{\rm exch}(\widetilde{x})$ is determined by keeping track of the energy gain or loss of the right particle for every colliding pair of particles within a region of size d around the position $\widetilde{x}$.

However, the energy involved in every collision drops drastically here and causes the energy exchange to decay linearly [13]. At the right wall the energy exchange vanishes, since the collisions of the rightmost particle with the wall are elastic.The hydrodynamic model does not predict the gradual growth of the density in the cluster, so $\widetilde{\kappa}(\widetilde{x})$ does not decrease but stays constant all the way up to the right wall.

5.4 Localized-energy-exchange model

Treating the $\widetilde{\kappa}$ as a step function, the temperature drops from 1 to zero in one step at $\widetilde{x}_1$:

$$\widetilde{T}(\widetilde{x}) = \begin{cases} 1 & \text{for } 0 < \widetilde{x} < \widetilde{x}_1 \ , \\ 0 & \text{for } \widetilde{x}_1 < x < \frac{L}{d}. \end{cases} \tag{5.16}$$

Here the value of $\widetilde{x}_1$ is determined from the fact that the cluster contains $N-1$ immobile particles, closely packed against the right wall: $\widetilde{x}_1 = \frac{L}{d} - (N-1)$. The corresponding number density is:

$$\widetilde{n}(\widetilde{x}) = \begin{cases} \left[\frac{L}{d} - (N-1)\right]^{-1} & \text{for } 0 < \widetilde{x} < \widetilde{x}_1 \ , \\ 1 & \text{for } \widetilde{x}_1 < x < \frac{L}{d}. \end{cases} \tag{5.17}$$

It jumps from a small value, representing the commuting particle in the left part of the tube [length $\frac{L}{d} - (N-1)$], at once to the close-packed value 1.

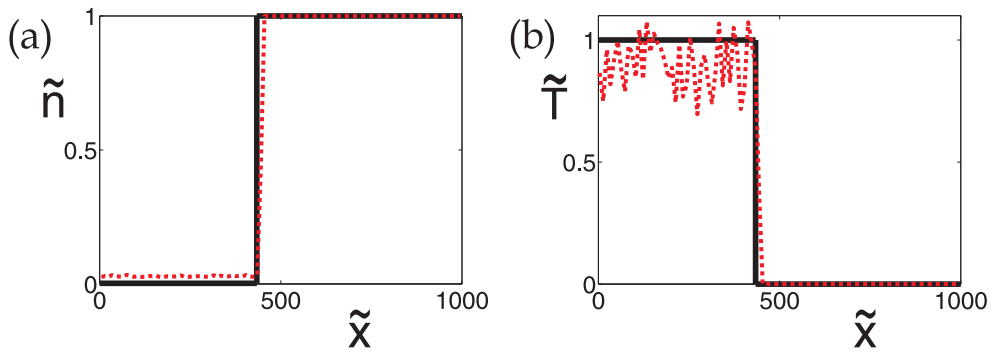

Figure 5.7: The localized-energy-exchange model of Eqs. (5.16)-(5.17) [solid black lines] vs. MD simulations [dashed red lines] for $N = 567$ particles. Both the density $\widetilde{n}(\widetilde{x})$ and the temperature $\widetilde{T}(\widetilde{x})$ show good agreement.

In this hybrid model, in which hydrodynamics is blended with the individual behavior of the leftmost particle, the force balance $d\widetilde{p}/d\widetilde{x} = 0$ still holds throughout the system (so the pressure is constant). Also the equation of state Eq. (5.9) has not been altered (in the dilute part it determines the constant value of $\widetilde{p}$, while in the solid part it gives an indeterminate result). The only adjustment has taken place in the energy balance (5.10): The exchange of energy, which in the pure hydrodynamic model was supposed to occur along the whole length of the tube, has been condensed to $\widetilde{x}_1$.

The density and temperature according to the localized model are compared with the MD results in Fig. 5.7. Not only the density profiles match well, as in the case of the purely hydrodynamic model, but also the temperature $\widetilde{T}(\widetilde{x})$ shows good agreement.

5.5 Conclusion

So we have answered the question to what extent hydrodynamics works in this granular system: It successfully captures the density, with its sharp division in a dilute and a clustered region, but *not* the temperature. This can be traced back to the basic assumption of the continuum approach, that the dilute region - even when the density gets very low - is supposed to consist of a sufficiently large number of particles to justify its treatment as a continuous medium. In the present system this assumption is incorrect, since the dilute region contains only *one* particle. It is at the level of the energy exchange that the discrepancy really makes a difference: Where the continuum view would have an energy exchange throughout the dilute region (and a corresponding decrease in the granular temperature), the energy of the commuting particle remains in fact constant until it meets the cluster [24].

We introduced a localized-energy-exchange model which keeps the good points of the hydrodynamic description (the force balance, and the equation of state incorporating excluded volume effects) mixed with the one-particle feature that all energy exchange takes place at the cluster boundary. This model gives an accurate description of both the density and the temperature.

Thus, the horizontal array of inelastic particles proves to be a prime example of granular hydrodynamics at its edge. Du *et al.* [10] introduced it as a system for which hydrodynamics simply breaks down, but there is more to it than that: It identifies the exact point at which the continuum description starts to fail and, on top of this, the reason why.

References

[1] L. P. Kadanoff, *Built upon sand: Theoretical ideas inspired by granular flows*, Rev. Mod. Phys. **71**, 435 (1999).

[2] J. T. Jenkins and M. W. Richman, *Kinetic theory for plane flows of a dense gas of identical, rough, inelastic, circular disks*, Phys. Fluids **28**, 3485 (1985).

[3] S. Luding, *Global equation of state of two-dimensional hard sphere systems*, Phys. Rev. E **63**, 042201 (2001).

[4] I. Goldhirsch and G. Zanetti, *Clustering instability in dissipative gases*, Phys. Rev. Lett. **70**, 1619 (1993).

[5] J. Eggers, *Sand as Maxwell's demon*, Phys. Rev. Lett. **83**, 5322 (1999).

[6] J. J. Brey, F. Moreno, R. García-Rojo, and M. J. Ruiz-Montero, *Hydrodynamic Maxwell demon in granular systems*, Phys. Rev. E **65**, 011305 (2001).

[7] E. Khain and B. Meerson, *Onset of thermal convection in a horizontal layer of granular gas*, Phys. Rev. E **67**, 021306 (2003).

[8] D. Lohse, R. Bergmann, R. Mikkelsen, C. Zeilstra, D. van der Meer, M. Versluis, K. van der Weele, M. van der Hoef, and H. Kuipers, *Impact on soft sand: Void collapse and jet formation*, Phys. Rev. Lett. **93**, 198003 (2004).

[9] P. Eshuis, K. van der Weele, D. van der Meer, and D. Lohse, *Granular Leidenfrost effect: Experiment and theory of floating particle clusters*, Phys. Rev. Lett. **95**, 258001 (2005).

[10] Y. Du, H. Li, and L. P. Kadanoff, *Breakdown of hydrodynamics in a one-dimensional system of inelastic particles*, Phys. Rev. Lett. **74**, 1268 (1995).

[11] E. L. Grossman and B. Roman, *Density variations in a one-dimensional granular system*, Phys. Fluids **8**, 3218 (1996).

[12] J. Yang, *Dynamics of a one-dimensional inelastic particle system*, Phys. Rev. E **61**, 2920 (2000).

[13] This spread originates from the collision of the hot, leftmost particle with velocity U with a cluster-particle having a negligible velocity in which the latter obtains a velocity of the order of $U(1-e)/2$. One can show that after the momentum of the hot particle has been transferred through the cluster towards the elastic wall and back again, this leads to a velocity difference of $(1-e)^2(N-2)U/4$ between the leftmost particle of the cluster and the rightmost particle of the cluster. Note that this spread

decreases with decreasing dissipation and becomes vanishingly small in the limit $e \to 1$, thus explaining the decrease of the fluctuations of the center of mass of the cluster as the system becomes more elastic.

[14] An interesting variation is to consider particles of unequal mass, see J.J. Wylie and Q. Zhang, *Periodic orbits of a one-dimensional inelastic particle system*, C.R. Acad. Sci. Paris, Ser. **I**, 339 (2004); *Collapse of periodic orbits in a driven inelastic particle system*, Phys. Rev. E **74**, 011305 (2006).

[15] S. McNamara and W. R. Young, *Inelastic collapse and clumping in a one-dimensional granular medium*, Phys. Fluids A **4**, 496 (1992).

[16] This type of forcing is called stochastic by K. Geisshirt, P. Padilla, E. Præstgaard, and S. Toxvaerd, *Controlling the temperature of one-dimensional systems composed of elastic and inelastic particles*, Phys. Rev. E **57**, 1929 (1998).

[17] J. M. Pasini and P. Cordero, *Clustering and fluidization in a one-dimensional granular system: Molecular dynamics and direct-simulation Monte Carlo method*, Phys. Rev. E **63**, 041302 (2001).

[18] C. Vamoş, N. Suciu, and A. Georgescu, *Hydrodynamic equations for one-dimensional systems of inelastic particles*, Phys. Rev. E **55**, 6277 (1997).

[19] For the granular Leidenfrost effect [9], see Ch. 3, this balance had the form $dp/dx = -mgn$, but since we now deal with a horizontal system the gravity term is absent.

[20] F. Cecconi, F. Diotallevi, U. M. B. Marconi, and A. Puglisi, *Fluid-like behavior of a one-dimensional granular gas*, J. Chem. Phys. **120**, 35 (2004).

[21] E. L. Grossman, T. Zhou, and E. Ben-Naim, *Towards granular hydrodynamics in two-dimensions*, Phys. Rev. E **55**, 4200 (1997).

[22] From Eq. (5.9) one finds $\widetilde{n} = \widetilde{p}_0/(\widetilde{p}_0 + \widetilde{T})$, and with $\widetilde{p}_0 = \widetilde{n}(0)/[1 - \widetilde{n}(0)]$ (since $\widetilde{T}(0) = 1$) this yields Eq. (5.12).

[23] Once $\widetilde{T}(\widetilde{x})$ and $\widetilde{\Phi}(\widetilde{x})$ have been found, the number density $\widetilde{n}(\widetilde{x})$ is given by Eq. (5.12). Next, we turn to the third boundary condition of Eq. (5.11): Integrating $\widetilde{n}(\widetilde{x})$ over the tube length yields the total number of particles N.

[24] It is instructive to contrast this with the analogous case of the granular Leidenfrost effect in a 2D setup [9], see Ch. 3, where the dilute region contained numerous particles and could therefore be successfully described as a gas.

6

Granular Realization of the Smoluchowski-Feynman Ratchet

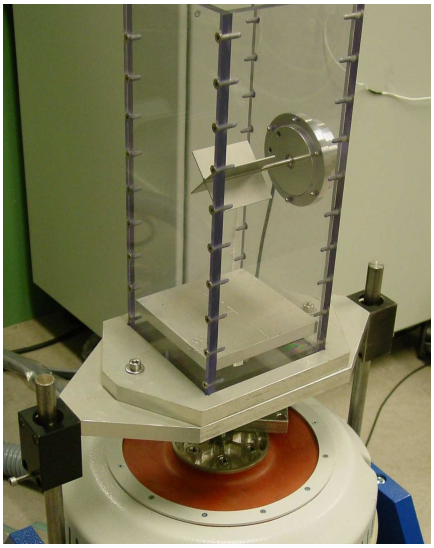

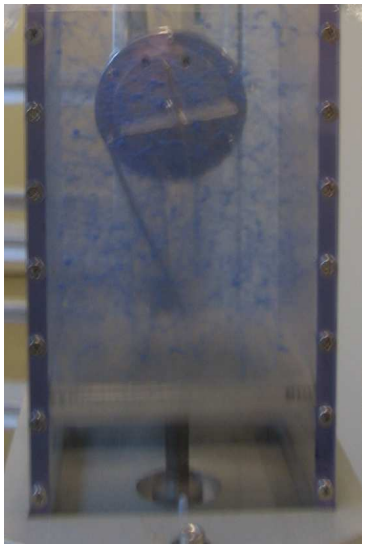

Peter Eshuis, Devaraj van der Meer, Ko van der Weele, and Detlef Lohse, *preprint* (2007).

We construct a working Smoluchowski-Feynman ratchet consisting of four vanes that are allowed to rotate freely in a vibrofluidized granular gas. The two sides of the vanes are coated differently to induce a preferential direction of rotation, i.e., the ratchet effect. Above a critical shaking strength, the probability distribution function of the angular velocity develops a double maximum, due to the positive feedback the vanes get from the convective rotation they induce in the granular gas.

6.1 Introduction

The importance of Brownian motors, which extract useful work from a noisy environment, can hardly be overstated. Examples are ubiquitous, ranging from the motor proteins in our bodies to self-winding wristwatches. And with nanotechnology strongly developing, there is a growing demand for tiny devices that are able to convert stochastic energy (heat for instance) into directed motion [1, 2]. To circumvent the second law of thermodynamics, which states that no work can be extracted from a system in thermodynamic equilibrium, these motors must operate under non-equilibrium conditions.

In order to get directed motion (i.e., a ratchet effect), some kind of symmetry breaking is necessary, either spatially or temporally. Usually this is accomplished by an asymmetry in the geometry of the motor. An especially appealing Brownian motor was thought of in 1912 by Smoluchowski [3] and made famous in the Feynman lectures [4]. It consists of four vanes (reminiscent of a windmill) and a pawl (an asymmetric toothed wheel), as shown in Fig. 6.1(a). The device is submerged in a heat bath.

If the bath is in thermodynamic equilibrium there is no ratchet effect: Although at first glance it seems that the wheel can turn in only one direction (and might lift the attached weight), Smoluchowski and Feynman showed that this is actually not the case, since both the vanes *and* the pawl are subject to collisions with the gas molecules. This makes the pawl bounce off the toothed wheel, thus enabling the device to rotate randomly in either direction. Indeed, if it were possible to lift the weight under equilibrium conditions, the engine would violate the second law of thermodynamics.

If the gas is out of thermal equilibrium, however, the Smoluchowski-Feynman ratchet may work. This has partly been realized by various chemical motors on a molecular scale [5–12]. We now present a continuously rotating Smoluchowski-

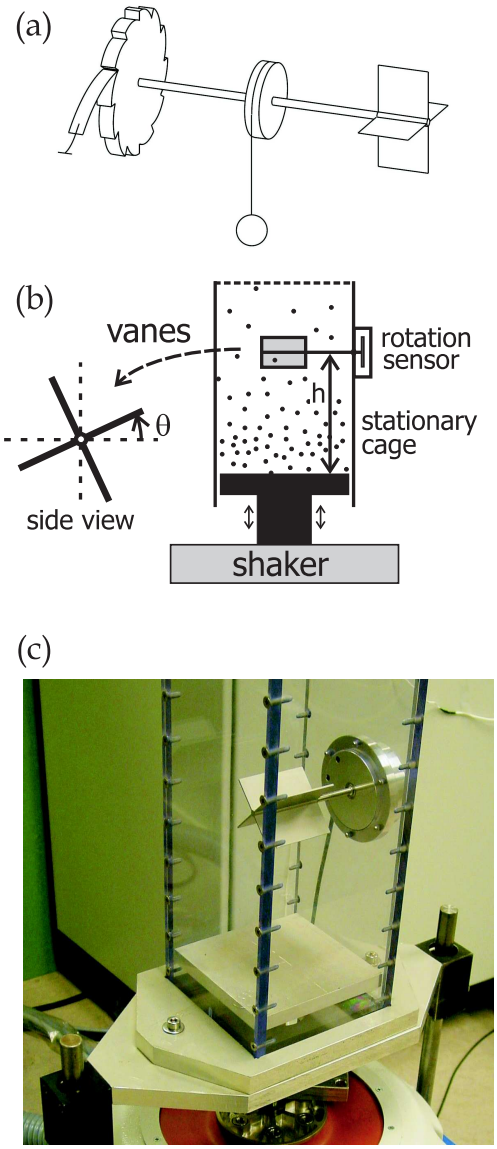

Figure 6.1: (a) The Gedankenexperiment of Smoluchowski [3] as envisaged by Feynman [4]. (b) Our granular version of the Smoluchowski-Feynman ratchet. The vanes are able to rotate in both directions when hit by the granular particles, and their angle $\theta(t)$ is recorded by the rotation sensor. The height h (between the null-position of the vibrating bottom and the vanes) can be varied. (c) The actual setup.

Feynman ratchet, using a granular gas as a heat bath. This type of gas is out-of-equilibrium: To keep it in motion, it needs a constant energy input, which is constantly dissipated by the inelastically colliding particles.

Our setup is shown in Fig. 6.1(b) and 6.1(c). The four vanes (25×60 mm each) are made from stainless steel and they are constructed out of one piece to make the construction optimally balanced. The axis of the vanes is attached to the container wall by a low-friction ball bearing. The angle $\theta(t)$ is measured (at a frequency of 1000 Hz) by an optical angle encoder, with an accuracy of $1.9 \cdot 10^{-4}$ rad. Thanks to the very small moment of inertia of this sensor ($I = 7.2 \cdot 10^{-5}$ kgm^2), single collisions of the particles with the vanes can easily be detected. The granular particles in our setup are glass beads of diameter $d = 4.0$ mm ($\rho = 2600$ kg/m^3). They are brought into a gas-like state by the vibrating bottom, which is mounted on a shaker with tuneable frequency f and amplitude a. The container is not connected to this bottom: It is a stationary plexiglass cage ($140 \times 140 \times 400$ mm) with a meshed top in order to keep the particles inside and the air pressure within the setup constant.

The system is carefully balanced via a series of test experiments. The balancing is an essential feature of the setup, since any unbalance would induce an unintended directed motion and obscure the ratchet effect.

The natural dimensionless control parameters for this system are: (i) The number of particles N, which we vary from 500 to 2000; (ii) The dimensionless height h/d of the vanes above the vibrating bottom (in our experiments we choose either $h = 51$ mm or $h = 75$ mm, i.e., $h/d = 12.75$ or 18.75); (iii) The shaking strength parameter,

$$S = \frac{4\pi^2 (af)^2}{gh}, \tag{6.1}$$

which is the ratio of the typical kinetic energy given to the particles by the vibrating bottom and their potential energy at the height of the vanes (this is the parameter which we will vary systematically); and (iv) the coefficient of normal restitution e of the particle-particle collisions (we do not vary this last parameter, using glass spheres with $e \approx 0.95$ throughout).

6.2 Symmetrically coated vanes

We first study the symmetric (non-ratchet) version of the system, in which the two sides of each vane are identical. In each experiment we start out from the same

configuration with the vanes forming an upright cross (+). Figure 6.2 shows the results at four different values of the shaking strength S:

(a) At mild shaking, the bulk of the granular gas remains close to the bottom and only rarely does a particle jump high enough to hit the vanes. The first one will unbalance the + configuration and move the vanes towards an $\times$ position, which is stabilized through the following mechanism: The particles coming from the vibrating bottom mainly have a velocity in the vertical direction and when hitting the vanes in an $\times$ position they are reflected towards the neighboring lower vane; the collision with this vane redirects them back to the vibrating bottom. These two collisions have an opposite effect on the rotation of the vanes and overall they add up to only a negligible net rotation. This stabilizing effect is absent for the + position, since here the particles usually collide only once with the vanes.

In the $\times$ configuration, the two top vanes act as a particle trap as sketched. This means that the vanes now and again have to turn sideways to unload the trapped particles, and afterwards re-assume an $\times$ configuration again. For growing shaking strength the system has to unload more frequently, because more particles are caught per second when the center of mass of the gas is located close to the vanes.

(b) Above a critical value S_{cr}, this rocking motion turns into an unbiased random walk between the four equivalent $\times$ positions. That is, the vanes now explore a widening range of angles following the diffusion law $\langle \theta^2(t) \rangle = 2Dt$, where D is the diffusion coefficient [13]. The value of D grows with increasing shaking strength. The distribution of the angle $\theta(t)$ (mod 2π) over time still shows a preference for the $\times$ positions (see inset); this feature diminishes gradually with increasing S until at very strong shaking the distribution becomes uniform.

(c) In Fig. 6.2(c) we encounter a second transition: The probability distribution function (PDF) of the angular velocity $d\theta/dt$ develops a *double* maximum. This can be traced back to the fact that the rotating vanes induce a convective motion of the granular gas in the same direction. Thus, the vanes experience more kicks in that direction, causing them to persist in their rotation. Only a sufficiently large statistical fluctuation will reverse the direction, and then the same argument applies to the opposite rotation.

(d) At vigorous shaking, Fig. 6.2(d), the double maximum is evident: The angular velocity is either strongly positive or negative, but rarely close to zero anymore.

In Fig. 6.3 we plot the diffusion coefficient D as a function of the shaking strength parameter. It is zero up to the critical value S_{cr}, and then starts to rise continuously: $D \propto (S - S_{\mathrm{cr}})^{\alpha}$. The critical exponent $\alpha \approx 1.7$, determined from a best fit to the data around this point, confirms the observed smooth transition from

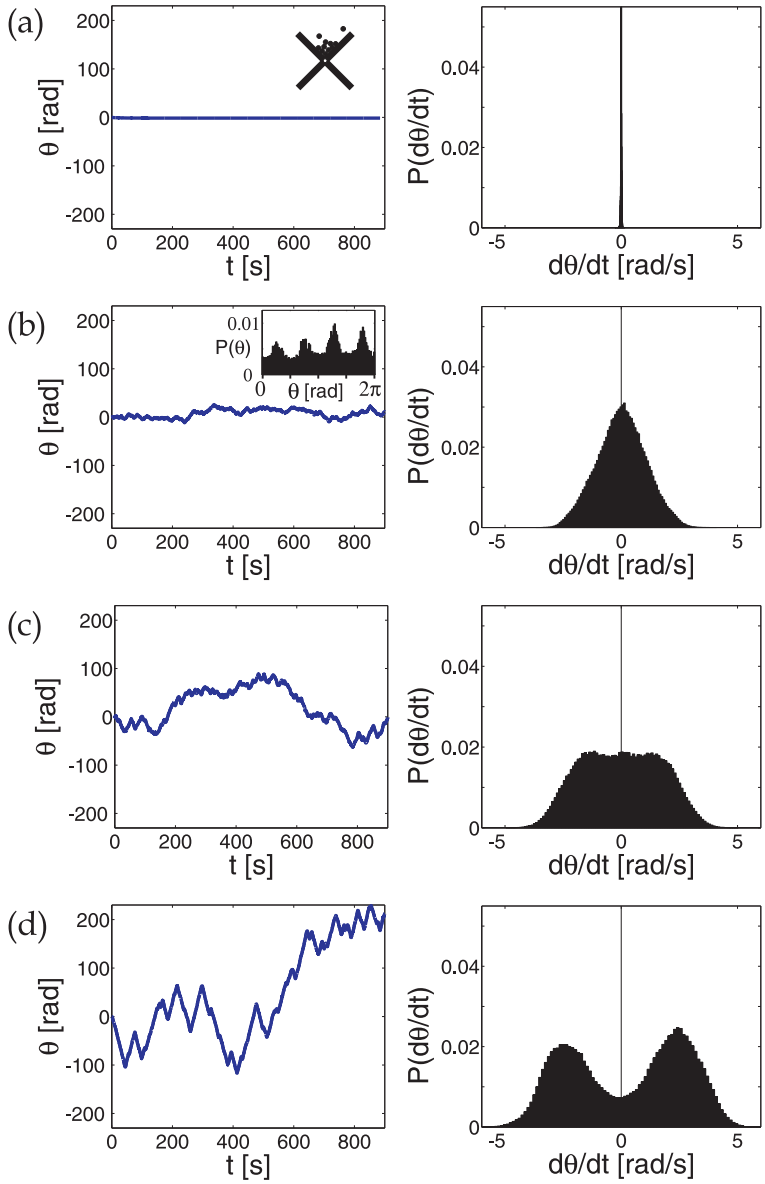

Figure 6.2: Symmetrically coated vanes. The angle $\theta(t)$ as a function of time and the PDF of the angular velocity, $P(d\theta/dt)$, for $N = 2000$ particles and $h = 51$ mm at four different shaking strengths: (a) amplitude $a = 1.5$ mm, frequency $f = 50$ Hz [i.e., $S = 0.44$], (b) $a = 1.5$ mm, $f = 110$ Hz [$S = 2.15$], (c) $a = 3.5$ mm, $f = 55$ Hz [$S = 2.92$], (d) $a = 3.5$ mm, $f = 65$ Hz [$S = 4.08$].

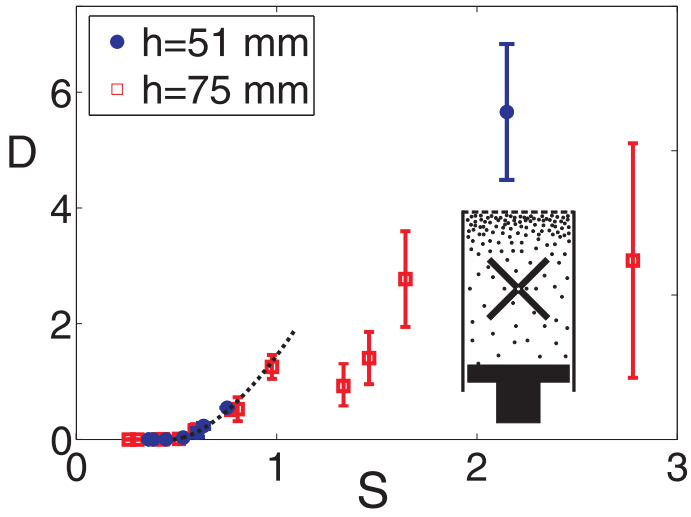

Figure 6.3: Symmetrically coated vanes. Diffusion coefficient D of the unbiased random walk performed by the vanes as a function of S, showing the onset of diffusion at $S_{\mathrm{cr}} = 0.48$. The dots (blue) are data for $h = 51$ mm, the squares (red) for $h = 75$ mm, always with $N = 1000$ particles. The error bars denote the standard deviation of the three experiments associated with each point. The dotted line (black) represents the best fit to the data around the onset: $D \propto (S - S_{\mathrm{cr}})^{\alpha}$, with critical exponent $\alpha \approx 1.7$. The sketched setup (for large S) shows that the granular gas has expanded far beyond the vanes, which is the reason for the decrease of D at strong shaking.

the rocking motion to the random walk between the four $\times$ positions.

For values well beyond the transition value S_{cr}, the diffusion coefficient D increases less steeply than predicted by the critical behavior, and at very strong shaking it is even seen to decrease. This is because the granular gas is shaken so vigorously here that the bulk of its mass is located *above* the vanes, see the inset in Fig. 6.3. The resulting reduction in the number of particle-vane collisions outweighs the fact that the impact per collision is stronger: Thus the total amount of energy imparted to the vanes (and hence D) is reduced.

6.3 Asymmetrically coated vanes: Ratchet

In order to turn the system into a ratchet, we now introduce a slight asymmetry. This is done by coating the left hand side of each vane with rubber tape, which makes this side considerably softer and changes the coefficient of normal restitu-

tion to $e \approx 0.5$. So here the kinetic energy from the colliding particles is dissipated more than on the other side, or stated differently, the collisions at the soft side are less effective in moving the vane. As a result the vanes will preferentially rotate in the counter-clockwise direction.

Figure 6.4, the asymmetric counterpart of Fig. 6.2, indeed shows a clear preference for the counter-clockwise motion (the positive θ direction): The Smoluchowski-Feynman ratchet has been achieved.

At very low shaking strengths [Fig. 6.4(a)], when there is hardly any interaction yet with the granular gas, the vanes flutter around the $\times$ position just as in the symmetric case. It takes a certain threshold value $S_{\rm cr}$ to establish the ratchet effect: In Fig. 6.4(b) the vanes are seen to rotate in the counter-clockwise direction with an average angular velocity $\langle d\theta/dt\rangle = 0.45$ rad/s. The maximum of the velocity distribution lies somewhat higher than this average value, and the inset shows the reason why: Despite its preference for the counter-clockwise direction, the system occasionally also moves in the other direction, when (due to a fluctuation) the collective particle collisions on the soft side of the vanes happen to overcome those on the uncoated side. These reversals are a characteristic feature of the ratchet and remain present also at higher shaking intensities.

In Fig. 6.4(c) we witness how the velocity distribution has acquired a shoulder, indicating the formation of a double maximum just as in the symmetric case, but now skewed. The fully developed double peak is seen in Fig. 6.4(d). The corresponding persistence of the rotational direction is also visible in the $\theta(t)$ plot: The duration of the velocity reversals is now much longer than in Fig. 6.4(b).

Figure 6.5 shows the mean ratchet speed $\langle d\theta/dt\rangle$ as a function of the shaking parameter S. The experimental data for $h = 51$ mm and $h = 75$ mm collapse onto a single curve, confirming that the shaking strength S is indeed the relevant shaking parameter for our ratchet. The onset of the ratchet effect takes place via a continuous phase transition at the critical value $S_{\rm cr} = 0.51$ (very close to the value 0.48 found in the symmetric case). Here the mean speed $\langle d\theta/dt\rangle$ becomes non-zero and starts to grow as

$$\langle d\theta/dt\rangle \propto (S - S_{\rm cr})^{\beta}, \tag{6.2}$$

with the critical exponent $\beta \approx 1.4$.

Just like the diffusion coefficient D for the symmetric system (Fig. 6.3), the ratchet speed $\langle d\theta/dt\rangle$ will not follow Eq. (6.2) indefinitely. When the shaking strength is increased to such an extent that the bulk of the granular gas is lifted above the vanes, the ratchet will become less efficient. This means that the highest

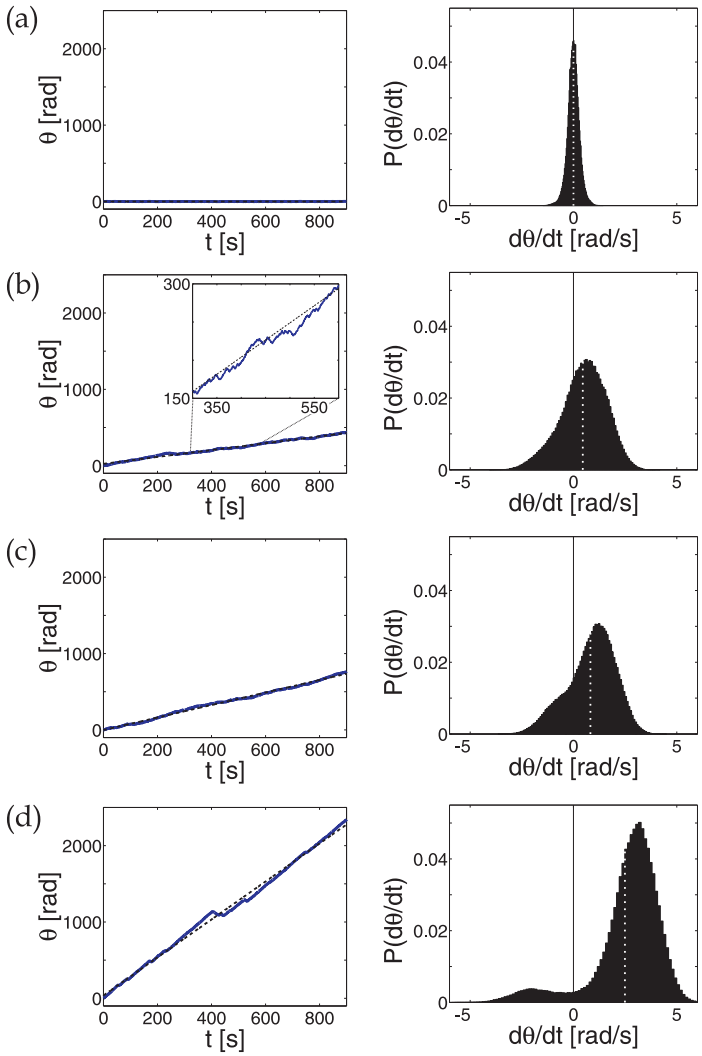

Figure 6.4: Asymmetrically coated vanes: ratchet. The angle $\theta(t)$ and the angular velocity distribution, for $N = 2000$ and $h = 51$ mm at four different shaking strengths. The ratchet effect (i.e., a non-zero average velocity $\langle d\theta/dt \rangle$) starts in situation (b). The dashed vertical lines give $\langle d\theta/dt \rangle$. (a) Shaking amplitude $a = 1.5$ mm, frequency $f = 60$ Hz [i.e., $S = 0.64$], $\langle d\theta/dt \rangle = 0.00$ rad/s, (b) $a = 1.5$ mm, $f = 110$ Hz [$S = 2.15$], the inset shows typical velocity reversals around the average $\langle d\theta/dt \rangle = 0.45$ rad/s, (c) $a = 3.5$ mm, $f = 55$ Hz [$S = 2.92$], $\langle d\theta/dt \rangle = 0.82$ rad/s, (d) $a = 3.5$ mm, $f = 65$ Hz [$S = 4.08$], $\langle d\theta/dt \rangle = 2.49$ rad/s.

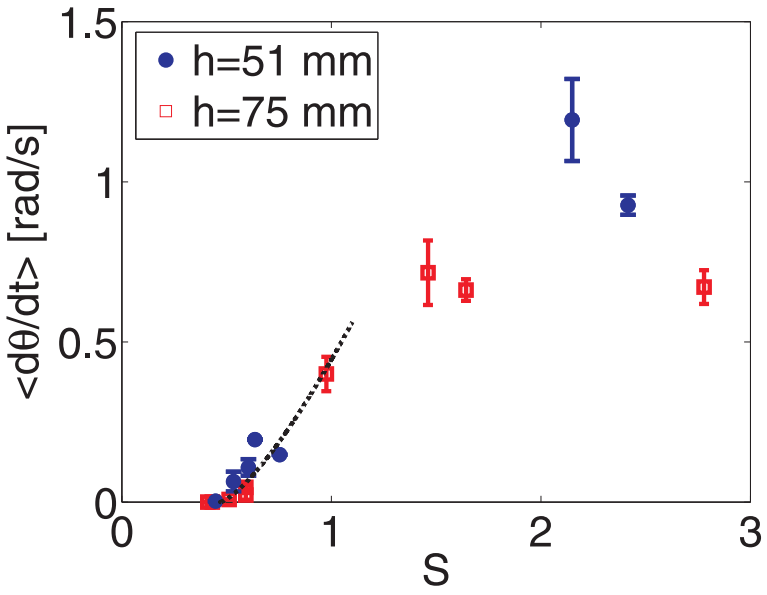

Figure 6.5: Asymmetrically coated vanes: ratchet. Ratchet speed $\langle d\theta/dt \rangle$ vs. S, showing the onset of the ratchet effect at $S_{\mathrm{cr}} = 0.51$. The dots (blue) are experimental data for $h = 51$ mm, the squares (red) for $h = 75$ mm, always with $N = 1000$ particles. The error bars denote the standard deviation of the three experiments associated with each point. The dotted line is the best fit to the data around the onset, $\langle d\theta/dt \rangle \propto (S - S_{\mathrm{cr}})^{\beta}$, with $\beta \approx 1.4$. The ratchet speed is seen to decrease for strong shaking, which is due to the expansion of the granular gas beyond the vanes, similar to the case of symmetrically coated vanes shown in Fig. 6.3.

efficiency is reached at some intermediate S-value, which depends on the number of particles: For small N (when the granular gas is lifted more easily) the optimal shaking strength lies lower than for large N.

6.4 Conclusion

We have constructed a continuously working Smoluchowski-Feynman ratchet, immersed in a granular gas. The inherent non-equilibrium properties of this gas are of fundamental importance for the ratchet, which otherwise (in a heat bath in thermodynamic equilibrium) would not be able to function [4].

The second important ingredient for the ratchet effect, the breaking of the symmetry, is introduced into the system by giving the two sides of each vane a

different coating. This immediately triggers a preferential direction of rotation, i.e., the ratchet effect. For symmetrically coated vanes the system performs an unbiased random walk, with no preference for either direction.

The onset of the ratchet effect takes place at a critical shaking strength S_{cr} via a continuous, smooth phase transition. Beyond this point, at vigorous shaking, a second critical phenomenon is observed: The velocity distribution develops a double maximum. Here the rotating vanes and the induced convection roll in the granular gas reinforce each other: They make the motion of the system more persistent, not only if this motion is in the preferential ratchet direction, but also in the case when (by a statistical fluctuation) the system happens to rotate in the opposite direction.

Acknowledgments: We would like to thank Gert-Wim Bruggert, Jean Walter, and Stijn Klaassen for setting up the experiment and Ralph Eichhorn, Peter Reimann, and Janneke Giele for stimulating discussions.

References

[1] P. Reimann, *Brownian motors: Noisy transport far from equilibrium*, Phys. Reports **361**, 57 (2002).

[2] R. D. Astumian and P. Hänggi, *Brownian motors*, Phys. Today **11**, 33 (2002).

[3] M. Smoluchowski, *Experimentell nachweisbare, der üblichen thermodynamik widersprechende Molekularphänomene*, Physik. Zeitschr. **13**, 1069 (1912).

[4] R. P. Feynman, R. B. Leighton, and M. Sands, *The Feynman Lectures on Physics*, Vol. **1**, Ch. 46 (Addison-Wesley, Reading, MA, 1963).

[5] T. R. Kelly, I. Tellitu, and J. P. Sestelo, *In search of molecular ratchets*, Angew. Chem. Int. Ed. Engl. **36**, 1866 (1997).

[6] A. P. Davis, *Tilting at windmills? The second law survives*, Angew. Chem. Int. Ed. Engl. **37**, 909 (1998).

[7] J. K. Gimzewski, C. Joachim, R. R. Schlittler, V. Langlais, H. Tang, and I. Johannsen, *Rotation of a single molecule within a supramolecular bearing*, Science **281**, 531 (1998).

[8] N. Koumura, R. W. J. Zijlstra, R. A. van Delden, N. Harada, and B. L. Feringa, *Light-driven monodirectional molecular motor*, Nature **401**, 152 (1999).

[9] K. L. Sebastian, *Molecular ratchets: Verification of the principle of detailed balance and the second law of dynamics*, Phys. Rev. E **61**, 937 (2000).

[10] R. A. van Delden, M. K. J. ter Wiel, M. M. Pollard, J. Vicario, N. Koumura, and B. L. Feringa, *Unidirectional molecular motor on a gold surface*, Nature **437**, 1337 (2005).

[11] D. Y. Petrov, R. Mallik, G. T. Shubeita, M. Vershinin, S. P. Gross, and C. C. Yu, *Studying molecular motor-based cargo transport: What is real and what is noise?*, Biophys. J. **92**, 2953 (2007).

[12] T. R. Kelly, X. Cai, F. Damkaci, S. B. Panicker, B. Tu, S. M. Bushell, I. Cornella, M. J. Piggott, R. Salives, M. Cavero, Y. Zhao, and S. Jasmin, *Progress toward a rationally designed, chemically powered rotary molecular motor*, J. Am. Chem. Soc. **129**, 376 (2007).

[13] See e.g. L.E. Reichl, *A Modern Course in Statistical Physics*, (2nd Ed., Wiley, New York, 1998).

7

Oscillations of Leidenfrost Stars

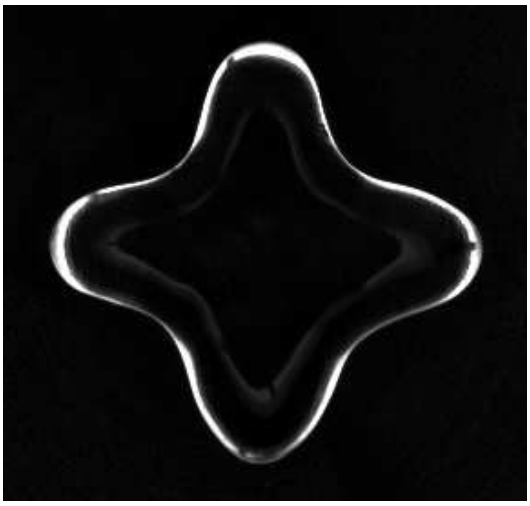

Peter Eshuis, Benjamin Dollet, Olivier Texier, and Devaraj van der Meer, *preprint* (2007).

When a drop of water is put on a hot plate held above the Leidenfrost temperature $T_L \approx 220\,^\circ$C, it will float on its own vapor layer for a long time. Above a critical plate temperature $T_{star} \approx 320\,^\circ$C this Leidenfrost drop shows star-like shape oscillations, i.e., Leidenfrost stars. We show that the oscillation frequency is well described by the capillary eigenfrequency irrespective of the exact geometry of the drop. Particle tracking within the drop reveals that these lateral shape oscillations form just one of the possible modes of motion in which the symmetry of the floating Leidenfrost drop is broken. The observed transitions between these motion modes correspond to a complete transfer of kinetic energy. We discuss the possible mechanisms triggering symmetry breaking.

7.1 The Leidenfrost effect

In 1732 the renowned Dutch researcher Hermann Boerhaave (1668-1738) wrote in his "Elementa Chemiae" that to his surprise a drop of alcohol put on a hot plate did not ignite, but started floating over the plate. This effect was thoroughly investigated by Johann Gottlob Leidenfrost (1715-1794) in "De Aquae Communis Nonnullis Qualitatibus Tractatus" (A Tract About Some Qualities of Common Water) published in 1756 [1], see Fig. 7.1. The Tractatus is a very detailed study of 175 pages in Latin, of which 39 deal with the experiment we now refer to as the "Leidenfrost effect": A drop of liquid deposited on a sufficiently hot surface will

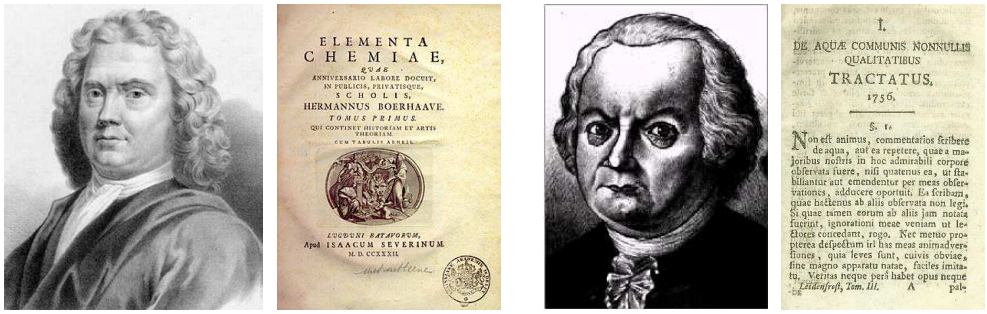

Figure 7.1: Hermann Boerhaave was the first to report the effect we now know as the "Leidenfrost effect" in his *Elementa Chemiae* of 1732: A drop can float on a sufficiently hot plate. Johann Gottlob Leidenfrost, Professor at the University of Duisburg (Germany), published his *Tractatus* in 1756, in which he reports the thorough research he performed.

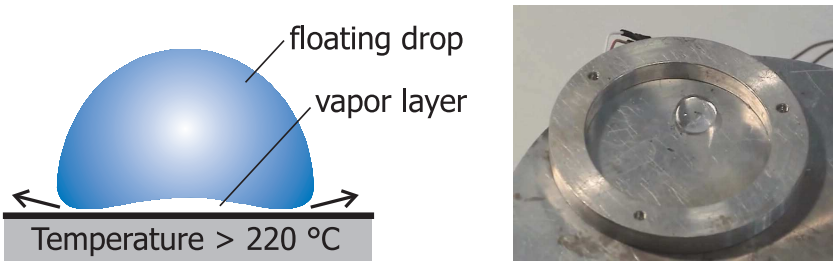

Figure 7.2: The Leidenfrost effect of a water drop hovering over a hot plate on its vapor layer.

hover over the surface for minutes instead of vaporizing instantly, see Fig. 7.2.

Leidenfrost started his experiments by carefully putting a drop of water into an iron spoon ("well polished and without rust") that was heated red-hot in a fireplace. Using a pendulum he then timed how long the drop survived, after which he deposited another drop. He observed that on the spot where the drop had been the spoon turned dull, whereas the surroundings were still red-hot. He noticed that the lifetime of the consecutive drops decreased rapidly.

How can this behavior be understood? When the drop hits the hot spoon the

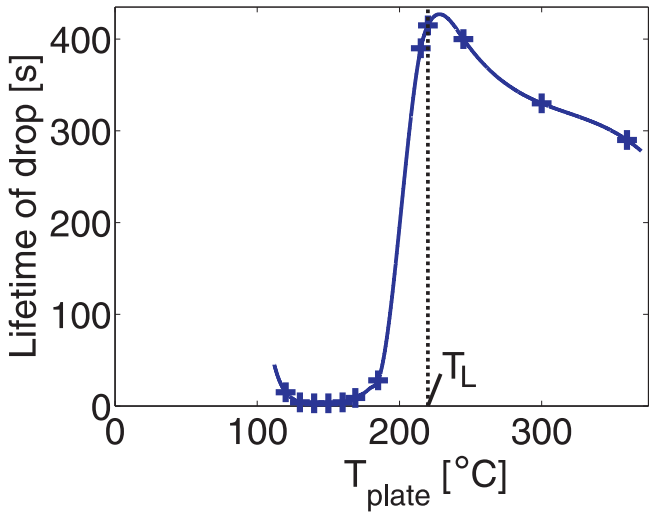

Figure 7.3: The lifetime of a drop of water (volume $V = 0.4$ ml) as a function of the plate temperature. The temperature for which the lifetime is maximal defines the Leidenfrost temperature T_L.

bottom layer vaporizes immediately. From this moment on the vapor layer prevents direct contact of the drop with the hot surface. Heat is still transferred *indirectly* through the vapor cushion, but this is far less effective since water vapor is a poor heat conductor and therefore the Leidenfrost drop evaporates only slowly.

The Leidenfrost effect is observed for drops of water if the temperature of the hot surface is held above the so-called Leidenfrost temperature, which is $T_L \approx 220\,^{\circ}\mathrm{C}$ for water. At this temperature the drop lives longest, which can easily be 7 minutes under ideal circumstances. Figure 7.3 shows that for temperatures below the Leidenfrost temperature the lifetime of the drop diminishes rapidly. This is due to the fact that the vapor layer shrinks until direct contact with the hot surface can instantly vaporize the drop. It was exactly this process that was observed by Leidenfrost by adding drops to the spoon causing it to cool down far below the Leidenfrost temperature.

The Leidenfrost effect, also known as film-boiling, is important in many industries where liquid comes into contact with a hot surface. Professional cooks utilize the Leidenfrost effect to check whether their pan is hot enough, by putting a drop of water on a pan. If it becomes a floating Leidenfrost drop the temperature is high enough to bake pancakes for example.

7.2 Leidenfrost stars

As the temperature of the hot surface is increased far above the Leidenfrost temperature, the drop starts to show star-like shape oscillations. To our knowledge this phenomenon has been reported for the first time by Holter and Glasscock in 1952 [2] and a small number of experimental studies have been reported since [3–7]. Here we present a study on the dynamics of and the process to these lateral shape oscillations, which we call "Leidenfrost stars" similar to the "nitrogen stars" reported by Strier *et al.* for freely evaporating drops of liquid nitrogen [8].

Closely related to these Leidenfrost stars are the drops subjected to vertical vibrations that show contour oscillations when shaken above a critical shaking strength [9, 10]. Similar oscillation modes have been reported for drops levitated aerodynamically or magnetically [11–14].

Our setup consists of a stainless steel disk (diameter 13 cm) with a concave top surface with radius of curvature of 0.7 m. This shape ensures that the drop is centered by gravity such that the drop can float smoothly over the disk without wandering off. The disk is placed on an accurate heater such that the spatiotemporal temperature fluctuations remain below $2\,^{\circ}\mathrm{C}$. The plate temperature T is

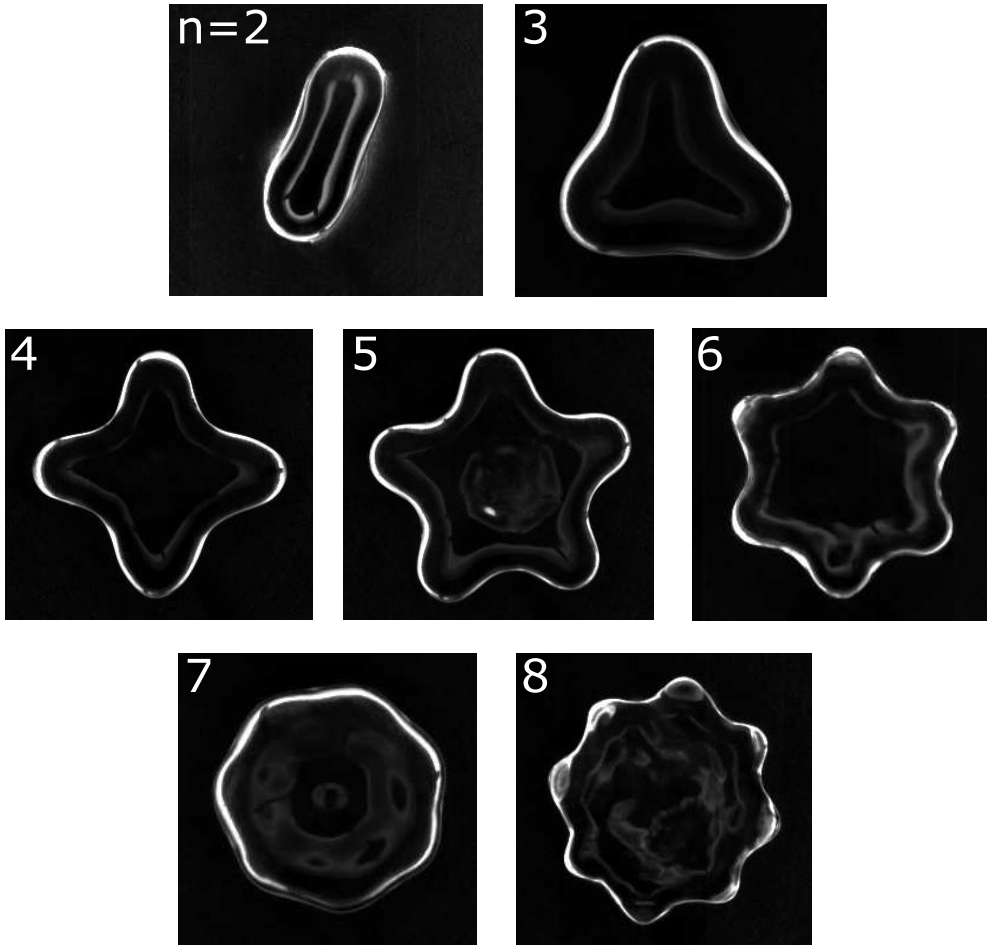

Figure 7.4: High-speed pictures of Leidenfrost star modes $n = 2-8$ (with n the number of lobes), that establish spontaneously during the evaporation process when the plate temperature is above $T_{\text{star}} \approx 320\,^{\circ}\text{C}$. The highest mode numbers, $n = 7$ and $n = 8$, are rarely observed and can be induced by poking the drop. We focus on freely evolving Leidenfrost drops only, which most commonly show the $n = 4$ and $n = 6$ mode.

measured by a thermocouple incorporated in the hot plate.

A ring light (diameter 18 cm) consisting of white LED's was placed 5 cm above the plate. It provided the oblique, continuous illumination to capture the entire contour of the rapidly oscillating drop using a high-speed camera recording the top view at 1000 fps. Besides, a normal-speed camera (30 fps) filmed all experiments from above to study the dynamics of the Leidenfrost drop on longer

time scales. Due to the concave shape of the plate we were not able to record the drop from aside, so we focus on the top view only.

Every experiment is initialized by depositing a drop of ultra pure water (Millipore) in the center of the hot plate by a syringe. To optimize reproducibility, water is injected in excess, such that the initial drop experiences a Rayleigh–Taylor instability of its bottom interface [7]: In the center of the drop a pocket of vapor accumulates and eventually bursts when the top surface is met. This instability is present until the evaporating drop has reached a radius of $r \approx 10$ mm, which defines a common starting point of our experiments.

During the evaporation process we often witness the spontaneous formation of a Leidenfrost star, provided that the plate is above the critical temperature $T_{\text{star}} = 320 \pm 5\,^{\circ}\text{C}$. Figure 7.4 shows several examples of Leidenfrost star modes n, where n is defined by the number of lobes of the star. We observed that if the plate temperature is well above T_{star} the probability for observing a Leidenfrost star increases considerably and becomes 1 for $T = 360\,^{\circ}\text{C}$.

Another observation was that for a fixed plate temperature and at a fixed drop size significant variations were found in the presence of a given mode. To obtain enough statistics we performed the experiment 20 times for a given plate temperature. It turns out that the Leidenfrost drop favors the even modes over the odd modes and especially the $n = 4$ and $n = 6$ mode are observed. In general, Leidenfrost stars are only observed for drops in the radius range $r = 3 - 8$ mm. More specifically, the probability distribution for the $n = 4$ mode shows two maxima, which are located at $r = 5$ mm and $r = 7$ mm. The $n = 6$ mode finds its single maximum at the intermediate drop radius of $r = 6$ mm. The studied range of plate temperatures ($T = 300 - 370^{\circ}\text{C}$) is too limited to determine the significance of these preferential drop sizes.

7.3 Drop morphology and particle tracking

Now that we have determined the conditions for the spontaneous formation of Leidenfrost stars, the route towards this phenomenon will be studied by visualizing the internal motion of the droplet. Therefore we tracked hydrophobic, polyamide particles of diameter 50 μm using a mass concentration of 0.02%. Although these particles remain at the surface, we experienced that the motion shown by the hydrophobic particles is a good indication for the flow within the drop. These experiments revealed that there are three morphologies possible during the evaporation process and they correspond to the following three modes of drop motion:

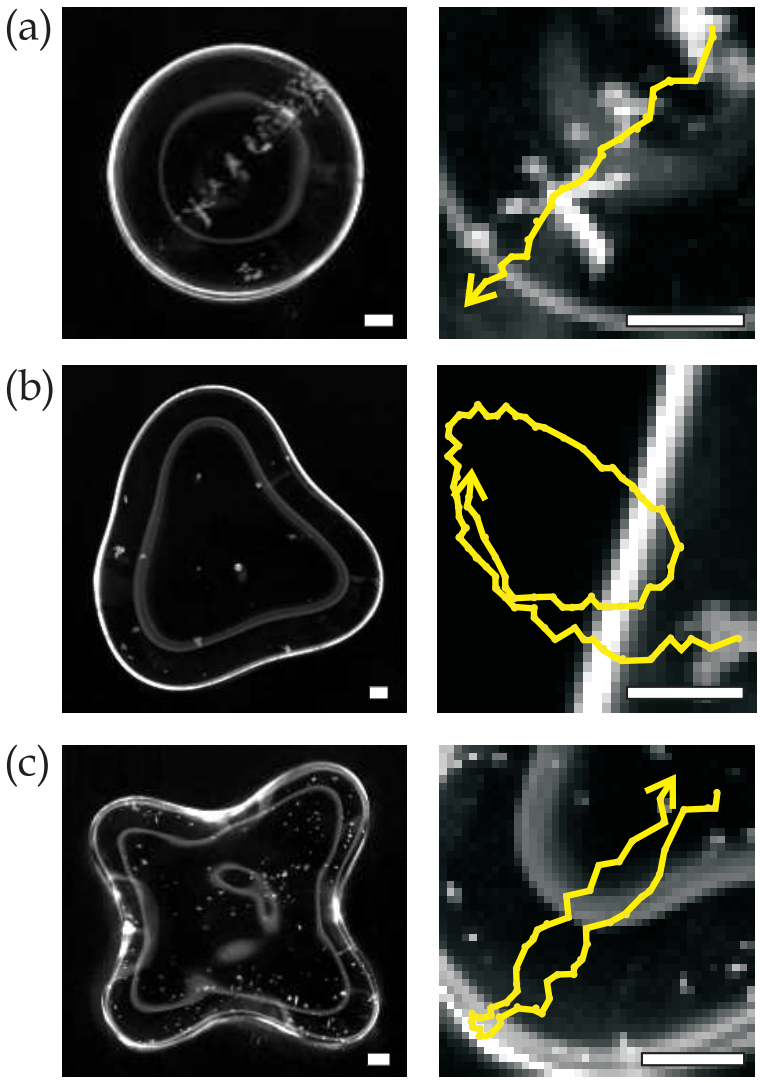

Figure 7.5: The three possible drop morphologies (white bars denote 1 mm): (a) A smooth, axisymmetric shape showing a large-scale *roll* running over the whole drop. In the zoom picture on the right the motion within the drop is visualized by particle tracking and is indicated by the solid, yellow line. (b) The non-axisymmetric shape is a result of a travelling *wave* along the surface, since the particle trajectory (solid, yellow line) in the zoom picture is a closed path. (c) A Leidenfrost *star* showing the $n = 4$ mode. The right image shows a tracked particle, which reflects the oscillation along a fixed axis directed towards the center of the drop.

(i) *Roll*: Figure 7.5(a) shows an axisymmetric shape with a circular top view that has a smooth surface. The surface can also be corrugated corresponding to axisymmetric surface modes developing along any cross-section of the drop. These vertical oscillation modes have been studied extensively for drops on vibrating hydrophobic substrates [9, 10]. We do occasionally observe this effect by eye, but cannot study it in detail due to our concave steel disk and therefore we focus on the case in which the drop has a smooth surface. At first glance this drop seems still, but the seeding particles reveal that in this axisymmetric shape an overall circulation is present.

(ii) *Wave*: The second morphology is the non-axisymmetric shape of Fig. 7.5(b), which at first seems to be a rigid rotating drop. Particle tracking however reveals that a travelling wave propagates along the drop contour without a significant rotation of the drop.

(iii) *Star*: The star-like shape of the Leidenfrost star is well approximated by the following contour equation:

$$r(\theta,t) = R + a_n \cos(2\pi f_n t)\ \cos(n\theta), \tag{7.1}$$

where R is the mean drop radius, a_n the amplitude of mode n and f_n the oscillation frequency for that mode. Fig. 7.5(c) shows the trajectory for a particle located close to the contour and demonstrates that it is passively transported back and forth by the shape oscillations. We did not observe any significant drop rotation on the timescale of these oscillations.

7.4 Capillary eigenfrequency

We now focus on the frequency f_n of the various Leidenfrost star modes recorded with the high-speed camera. By following the drop contour in the high-speed pictures as a function of time, the frequency of the mode is determined for all experiments. Figure 7.6 shows that the frequency of the $n = 4$ mode decreases for an increasing drop radius. This behavior indicates that the shape oscillations are a capillary phenomenon and we expect from dimensional analysis that the frequency scales as $f_n \propto \sqrt{\sigma/\rho L^3}$, with $\sigma = 59$ mN/m the surface tension for boiling water at 100 °C, $\rho = 960$ kg/m^3 the density of boiling water, and L the relevant length scale of the drop.

We now determine this relevant length scale L. Since our range of drop sizes lies above the capillary length $\ell_c = \sqrt{\sigma/\rho g} = 2.5$ mm (with $g = 9.81$ m/s^2 the

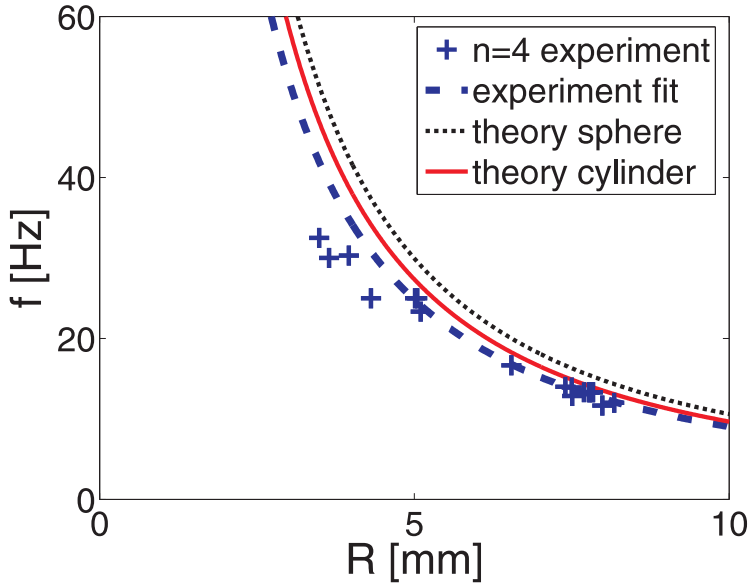

Figure 7.6: Frequency f of the $n = 4$ Leidenfrost star vs. the drop radius R. The $+$ signs (blue) represent experimental data and the dashed (blue) line is the fit for $R > 5$ mm yielding a power law exponent of -1.46. The dotted (black) line is based on Eq. (7.2) for the spherical geometry and the solid (red) line for the cylindrical prediction of Eq. (7.3), both with the theoretical value for $\sigma = 59$ mN/m for boiling water.

gravitational acceleration), the drops are flattened by gravity and have puddle-like shapes [7]. Hence their height does not vary much from the saturation value $2\ell_c$ [15] and therefore we expect the mean radius R to be the relevant length scale. This is confirmed by the fit for $R > 2\ell_c$ shown in Fig. 7.6 yielding a power law exponent of -1.46, which is close to the theoretical exponent $-3/2$ found above. For drop radii below $R = 2\ell_c = 5.0$ mm (i.e., when the height of the drop starts to play a role as the relevant length scale), the deviations from the experimental fit are observed to remain small. These deviations are probably caused by surfactants unavoidably picked up during the experiments, causing the surface tension to be reduced below the theoretical value of 59 mN/m for boiling water. Surfactants become more effective for smaller drop sizes [15], hence the observed small deviations from the experimental fit for $R < 5.0$ mm in Fig. 7.6.

So the experimental data and their fit presented in Fig. 7.6, indicate that the precise geometry of the drop is not of major influence on the frequency of the star oscillations. To make this argument more quantitative, we now compare the

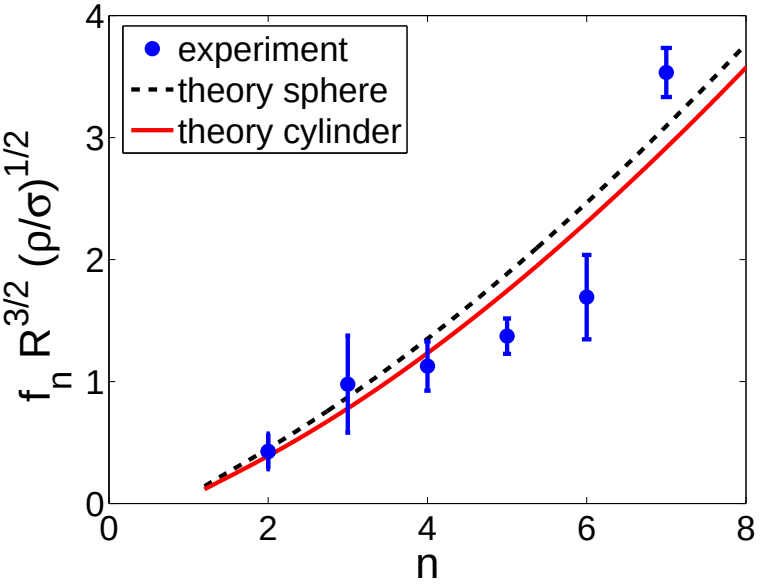

Figure 7.7: Dimensionless frequency $f_n R^{3/2}(\rho/\sigma)^{1/2}$ as a function of mode number n. The dots (blue) represent the averaged experimental data and the error bars denote the standard deviation. The dashed (black) line is based on the spherical geometry of Eq. (7.2) and the solid (red) line is for the cylindrical prediction of Eq. (7.3), both with $\sigma = 59$ mN/m.

measured frequency to the capillary eigenfrequency of two simple geometries; the sphere, and the cylinder. For a distorted sphere of shape $r(\theta,\varphi) = R + \varepsilon Y_{n,m}(\theta,\varphi)$, where $Y_{n,m}$ is a spherical harmonic, the eigenfrequency depends only on the mode number n as [16]:

$$f_n^2 = \frac{1}{(2\pi)^2}(n-1)n(n+2)\frac{\sigma}{\rho R^3}. \tag{7.2}$$

For a distorted cylinder of shape $r(\theta) = R + \varepsilon\cos\theta$, the eigenfrequency takes form [17, 18]:

$$f_n^2 = \frac{1}{(2\pi)^2}(n-1)n(n+1)\frac{\sigma}{\rho R^3}. \tag{7.3}$$

The predictions for the capillary eigenfrequency of Eq. (7.2) and Eq. (7.3) are in good agreement with the experimental data of Fig. 7.6, but show a small overestimation due to a slightly reduced surface tension σ caused by surfactants as mentioned above. Using σ of Eq. (7.2) as a fit parameter we obtain the effective surface tension for a spherical drop shape including surfactants:

$\sigma_{\text{sphere}} = 41$ mN/m. For the cylindrical shape, Eq. (7.3), we find an effective surface tension of $\sigma_{\text{cylinder}} = 50$ mN/m. These values are reasonably close to the theoretical one of 59 mN/m (for boiling water at 100 °C), such that we can conclude that the amount of surfactants involved in the experiments is very tiny, since only a minuscule concentration of surfactants changes the surface tension of water dramatically [11].

In order to compare the oscillation frequency for various mode numbers, we consider the *dimensionless* frequency $f_n R^{3/2}(\rho/\sigma)^{1/2}$ in Fig. 7.7. It is seen to grow with the mode number n and this trend is, again, well-described by the prediction for a capillary oscillation for a sphere and a cylinder, see Eqs. (7.2) and (7.3).

Figures 7.6 and 7.7 confirm that the capillary eigenfrequency shown by the Leidenfrost star is independent of the exact geometry of the drop.

7.5 Transfer of kinetic energy

In Fig. 7.5 we have identified three possible drop morphologies and particle tracking revealed that there is a close relation between the drop shape and its internal motion. We now show that the transitions between these motion modes conserve the total kinetic energy of the drop:

(i) For the axisymmetric drop with a smooth surface of Fig. 7.5(a), the internal motion is a single *roll* around the whole drop. All tracked particles show no significant velocity difference along their straight paths. The relative velocity variations for different particles across the drop are less than 10%. Since we do not know the velocity profile within the drop, a uniform velocity v_0 is assumed inside the whole drop. Thereby we slightly overestimate the kinetic energy, because in the middle of the roll, i.e., in the central part of the drop, the velocity should vanish. This leads to the following approximation for the total kinetic energy of a roll:

$$E_{roll} \approx \frac{1}{2}\rho V v_0^2, \tag{7.4}$$

where the drop volume is roughly $V \approx \pi R^2 h \approx 2\pi R^2 \ell_c$, since the drop is puddle-like as discussed in the previous section.

(ii) Figure 7.5(b) shows the non-axisymmetric, rotating shape, which corresponds to the motion mode of a travelling *wave* along the contour. Since the shape deformation remains small, the drop profile can be described by $r(\theta,t) = R + a_n(\theta - \omega t)$, with a_n the profile of the wave being a function of $\theta - \omega t$, with

Motion mode	**E** (μ**J**)
roll	0.76 $\pm$ 0.13
wave	0.85 $\pm$ 0.18
star ($n = 4$)	0.73 $\pm$ 0.23
star ($n = 6$)	0.71 $\pm$ 0.13

Table 7.1: The kinetic energy ($\pm$ standard deviation) based on Eqs. (7.4), (7.5) and (7.6) for the three motion modes: (1) An overall roll, (2) a travelling wave along the contour and (3) a Leidenfrost star. The kinetic energy for the $n = 6$ Leidenfrost star is a combination of two motion modes; star-like oscillations (0.48 ± 0.06 μJ) and an overall convective roll (0.22 ± 0.06 μJ).

θ the angle and ω the angular speed of rotation. Hence, the radial velocity component of a particle located at the contour is $v_C(\theta,t) = \partial r/\partial t = -\omega a_n'(\theta - \omega t)$. For a simple estimate we assume that the radial velocity field within the whole drop scales as $v(r,\theta,t) \approx r v_C(\theta,t)/R$, for $|a_n| \ll R$. Then the total kinetic energy corresponding to this motion mode reads:

$$\begin{aligned} E_{wave} &\approx \frac{1}{2}\rho \int_{\text{drop}} v^2 \mathrm{d}V \approx \frac{1}{2}\rho \frac{h}{R^2} \int_0^R r^3 \mathrm{d}r \int_0^{2\pi} v_C^2 \mathrm{d}\theta \\ &\approx \frac{1}{4}\rho \ell_c R^2 \omega^2 \int_0^{2\pi} (a_n')^2 \mathrm{d}\theta. \end{aligned} \tag{7.5}$$

The latter integral is then numerically computed from the contour profile of the drop. We neglect the tangential velocity component, which is much smaller than the radial component as shown in Fig. 7.5(b).

(iii) The shape of the Leidenfrost *star*, such as the $n = 4$ mode of Fig. 7.5(c), is well described by Eq. (7.1). The velocity of the tracked particles is directed in the purely radial direction for all modes except the $n = 6$ mode, where besides the oscillatory motion we additionally observe an overall circulation. This roll will be treated separately from the shape oscillations and in the same way as discussed above under (i).The pure radial velocity is estimated from Eq. (7.1): $v_r(\theta,t) = -\omega_n a_n \sin\omega_n t \cos n\theta$. We observed that particles located in the central area of the drop, i.e. $r \leq R_0 - a_n$, are hardly affected by the oscillations, which leads to the following approximate kinetic energy: $E_{star} \approx \rho \int_{\mathscr{V}} v_r^2 \mathrm{d}V/2$, where $\mathscr{V}$ is the volume of the drop in the region $r \geq R_0 - a_n$. After computing this integral and time-averaging, the total kinetic energy associated with the Leidenfrost stars becomes:

$$E_{star} \approx \frac{\pi}{2}\rho \ell_c R a_n^3 \omega_n^2. \tag{7.6}$$

Based on the estimates of Eqs. (7.4), (7.5) and (7.6), the kinetic energies associated with the three morphologies have been determined, see Table. 7.1. We averaged over various experiments, since no significant variations in the kinetic energy were found for drops of different size in the range $R = 5 - 8$ mm.

7.6 Discussion

The experiments discussed above yield information on the dominant mechanism triggering symmetry breaking observed in any of the three motion modes. We start with the mechanisms that can be excluded by the current investigation and end with the possible mechanisms triggering symmetry breaking:

First, destabilization by the Marangoni effect was suggested by Baumeister *et al.* [5] and *Strier et al.* [8]. They suggest that surface tension differences are present, based on the assumption that the top of the drop will be colder than the bottom. However, Biance *et al.* [7] reported a constant temperature in the drop of $99 \pm 1\,^{\circ}\mathrm{C}$, so the top-bottom symmetry is not broken.

Baumeister *et al.* [5] proposed that the driving force behind symmetry breaking might originate from the drop periodically touching the hot plate, thereby receiving a burst of energy. This mechanism can be excluded, since the Leidenfrost drop stays afloat without touching the hot plate when the plate temperature is above the Leidenfrost temperature for water, $T_L \approx 220\,^{\circ}\mathrm{C}$.

Thirdly, a plausible mechanism: The vapor flowing radially outward underneath the drop exerts a drag force on the bottom interface of the drop. As a result a toroidal vortex ring, like the one reported by Strier *et al.* [8], can be created within the drop. Although we have never observed a vortex ring, it is plausible that the vapor induces a flow inside the drop. The vortex ring may be unstable to some perturbation and trigger the breaking of symmetry we do observe in experiment.

Another possible mechanism is related to the vertical oscillation mode mentioned earlier and which was studied by Courty *et al.* [10]. We observed that the axisymmetric shape of Fig. 7.5 is then corrugated and a perturbation could trigger symmetry breaking in this vertically oscillating drop.

Finally, we discuss the mechanism that most likely leads to the formation of Leidenfrost stars: A perturbation, e.g., a nonuniform surfactant concentration, modulates the bottom interface of the drop, which results in “channels” that facilitates the outflow of vapor. Hereby zones of stronger drag are generated, where the drop is pulled radially outward. Surface tension then tries to restore the spherical

drop shape, leading to an inversion of the "channels" underneath the drop. This periodic modulation then sustains the oscillating Leidenfrost stars.

We observed that the even modes of the Leidenfrost stars are preferred over the odd modes. This is probably due to the fact that in an even mode the fluid in a lobe has a balancing counterpart in the opposite lobe, such that during the oscillations the center of mass does not move. This dynamical symmetry is absent in the odd modes, making them energetically less favorable for the Leidenfrost drop.

7.7 Conclusion

Oscillating Leidenfrost stars form spontaneously when a drop of water is deposited on a sufficiently hot plate, which should be kept above the critical temperature $T_{\text{star}} \approx 320\,^{\circ}\text{C}$. This is a capillary phenomenon, since the frequency of these shape oscillations is in good agreement with the capillary eigenfrequency of the Leidenfrost drop. We have shown that the exact geometry of the drop does not influence the frequency displayed by the Leidenfrost stars.

Three drop morphologies have been identified during the evaporation process of the Leidenfrost drop and they correspond to three motion modes in which the symmetry of the system is broken: An overall roll, a wave running over the contour, and a Leidenfrost star. In the observed transitions between these motion modes the kinetic energy is completely transferred, so the total energy of the drop is constant in all motion modes.

More experiments are needed to confirm the observed preferential drop sizes, for which specific Leidenfrost star modes are shown. Besides, a detailed study is needed to indicate the exact mechanism behind the symmetry breaking that eventually triggers the Leidenfrost stars.

Acknowledgments: We would like to thank Michel Versluis, Leen van Wijngaarden, Ko van der Weele, and Detlef Lohse, for stimulating discussions.

References

[1] J. G. Leidenfrost, *De Aquae Communis Nonnullis Qualitatibus Tractatus* (University of Duisburg, Duisburg, Germany, 1756), translated into English in: Int. J. of Heat and Mass Transfer **9**, 1153 (1966).

[2] N. J. Holter and W. R. Glasscock, *Vibrations of evaporating liquid drops*, J. Acoustical Soc. Am. **24**, 682 (1952).

[3] G. J. Schoessow and K. J. Baumeister, *Liquid drop model vibrations and simulated fission*, Chem. Eng. Prog. Symp. Ser. **62**, 47 (1966).

[4] W. B. Hall, *The stability of Leidenfrost drops*, Heat Transfer **4**, 125 (1974).

[5] K. J. Baumeister, R. C. Hendricks, and G. J. Schoessow, *Thermally driven oscillations and wave motion of a liquid drop*, Proc. Natl. Heat Transfer Conf. 158–165 (1977).

[6] H. Thimbleby, *The Leidenfrost phenomenon*, Phys. Educ. **24**, 300 (1989).

[7] A.-L. Biance, C. Clanet, and D. Quéré, *Leidenfrost drops*, Phys. Fluids **15**, 1632 (2003).

[8] D. E. Strier, A. A. Duarte, H. Ferrari, and G. B. Mindlin, *Nitrogen stars: Morphogenesis of a liquid drop*, Phys. A **283**, 261 (2000).

[9] X. Noblin, A. Buguin, and F. Brochard-Wyart, *Triplon modes of puddles*, Phys. Rev. Lett. **94**, 166102 (2005).

[10] S. Courty, G. Lagubeau, and T. Tixier, *Oscillating droplets by decomposition on the spherical harmonics basis*, Phys. Rev. E **73**, 045301 (2006).

[11] R. E. Apfel, Y. Tian, J. Jankovsky, T. Shi, X. Chen, R. G. Holt, E. Trinh, A. Croonquist, K. C. Thornton, A. Sacco Jr., C. Coleman, F. W. Leslie, and D. H. Matthiesen, *Free oscillations and surfactant studies of superdeformed drops in microgravity*, Phys. Rev. Lett. **78**, 1912 (1997).

[12] R. G. Holt, Y. Tian, J. Jankovsky, and R. E. Apfel, *Surface-controlled drop oscillations in space*, J. Acoust. Soc. Am. **102**, 3802 (1997).

[13] M. Papoular and C. Parayre, *Gas-film levitated liquids: Shape fluctuations of viscous drops*, Phys. Rev. Lett. **78**, 2120 (1997).

[14] E. Hervieu, N. Coutris, and C. Boichon, *Oscillations of a drop in aerodynamic levitation*, Nucl. Eng. and Design **204**, 167 (2001).

[15] P. G. de Gennes, F. Brochard-Wyart, and D. Quéré, *Capillarity and Wetting Phenomena: Drops, Bubbles, Pearls, Waves* (Springer-Verlag, New-York, 2004).

[16] H. Lamb, *Hydrodynamics* (6th Ed., Cambr. Univ. Press, Cambridge, UK, 1932).

[17] J. W. S. Rayleigh, *The Theory of Sound* (Macmillan, London, UK, 1877).

[18] S. Chandrasekhar, *Hydrodynamic and Hydromagnetic Stability* (Dover, New-York, 1981).

8
General Conclusion

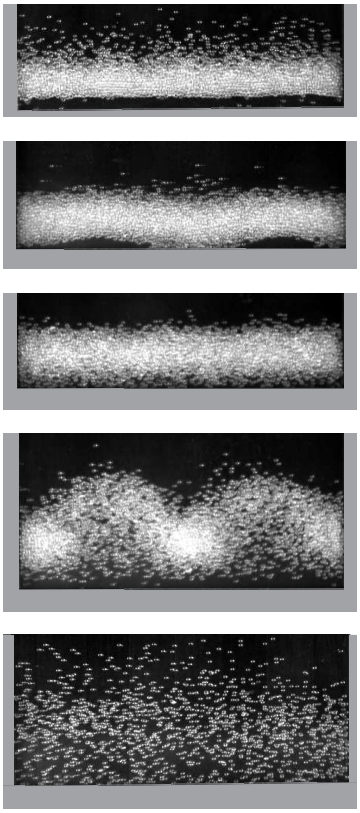

8.1 Conclusion

In this thesis collective phenomena observed in vertically shaken granular matter have been studied by means of experiments, simulations and theoretical analysis. The combined results shed light on the degree to which hydrodynamic-like models can be applied to granular systems, thereby answering the central question posed in Chapter 1.

First of all the experiments of Chapter 2 revealed a rich phase diagram featuring the following phenomena: Bouncing bed, undulations, granular Leidenfrost effect, convection rolls, and granular gas. Keeping the particle parameters fixed, we showed that the dimensionless acceleration Γ is the relevant shaking parameter for *mild* fluidization, and the dimensionless shaking strength S governs the phenomena observed for *strong* fluidization.

We then explored the details of this phase diagram, where the granular Leidenfrost effect (Chapter 3) is observed in experiment for the first time: Above a critical shaking strength, and for a sufficient number of beads, a crystalline cluster is elevated and supported by a dilute gaseous layer of fast beads underneath. This state, in which the solid and gas phases co-exist, is *quantitatively* captured by a hydrodynamic model. This is a great success for granular hydrodynamics, since granular systems cannot a priori be expected to be correctly described by continuum theory.

Exploring the phase diagram further we studied buoyancy driven granular convection in Chapter 4. These counter-rotating convection rolls with pronounced density variations are observed for strong fluidization. The experimental results are in agreement with Molecular Dynamics simulations and the onset of convection is successfully explained by a linear stability analysis of the hydrodynamic model of the Leidenfrost state. This theoretical approach for granular convection is analogous to the one used to determine the onset of Rayleigh-Bénard convection in ordinary liquids. This once more stresses the applicability of granular hydrodynamics for collective phenomena observed at strong shaking strengths.

The success of the continuum description for the Leidenfrost effect and the convection may be attributed to the fact that the clusters, the convection rolls, and also the dilute parts are sufficiently large compared to the size of a single particle. To explore the limits of continuum theory, in Chapter 5 we therefore study

a system which has a characteristic feature of the size of a single particle: The horizontal array of inelastic particles introduced by Du, Li, and Kadanoff [1]. We showed by comparing hydrodynamic theory to Molecular Dynamics simulations, that the continuum model correctly describes the density profiles but *not* the temperature. The reason for this breakdown of continuum theory is that in the steady state only one particle commutes between the left wall and the close-packed cluster on the right. Hydrodynamics assumes energy exchange throughout the dilute region, but the actual energy exchange of this single particle only takes place right *at* the boundary of the cluster. This sharp localization (of the size of one single particle) is the reason why the continuum approach starts to fail: This system marks the edge of granular hydrodynamics.

In Chapter 6 we experimentally realized the first macroscopic Smoluchowski-Feynman ratchet and the first one able to rotate continuously, consisting of four rotating vanes in a granular gas. This granular ratchet can work thanks to the fact that the granular gas is far from thermal equilibrium *and* because we have broken the symmetry of the system by coating the two sides of each vane differently. The ratchet effect sets in at a critical shaking strength S_{cr} via a continuous, smooth phase transition. At vigorous shaking a second critical phenomenon is observed: The velocity distribution develops a double maximum, due to the positive feedback which the vanes get from the convective rotation they induce in the granular gas.

In Chapter 7 we turn from granular hydrodynamics to ordinary liquids: Oscillating Leidenfrost stars. These stars form spontaneously when a drop of water is deposited on a sufficiently hot plate, i.e., higher than $T_{\mathrm{star}} \approx 320\,^{\circ}\mathrm{C}$. We have shown that this is a capillary phenomenon, since the frequency of these shape oscillations is in good agreement with the capillary eigenfrequency of the floating Leidenfrost drop. The exact geometry of the drop does not influence the frequency of oscillation of the Leidenfrost stars.

8.2 Outlook

The present study, like any research project, has not only answered many questions but also generated a number of new ones. Hopefully, these questions will become the subject of future investigations, and for this reason the most relevant and promising ones will be put forward here.

In the context of Chapter 2 the main future objective is to extend the phase diagram obtained for the quasi 2-D setup to the general case for three dimensions. This will show an even wider variety of phenomena, including oscillons, 3-D wave patterns, and 3-D convection cells [2–25]. The phase transitions of this general 3-D phase diagram constitute an interesting research field on its own. Granular systems are ideally suited to study phase transitions in non-equilibrium many particle systems, and the fact that these systems consist of much less than the 10^{23} particles of standard statistical physics means that also the influence of small number fluctuations will show up naturally.

We have already made a step towards this general 3-D phase diagram when we varied the aspect ratio for the granular Leidenfrost effect in Chapters 2, 3, and 4. In the 2-D setup of Chapter 3 we focused upon the transition from the solid phase to the Leidenfrost state (which was found to be a second order, continuous phase transition) and in the slightly higher dimensional setup of Chapter 4 we studied the transition from the Leidenfrost state to buoyancy-driven convection. It will be very interesting to see how a further increase of the dimensionality of the system will change the location of the Leidenfrost state and its transitions to other, neighboring states in the phase diagram.

The phase diagrams in the present thesis were obtained primarily from experiment and theory. We think that in order to obtain the general 3-D phase diagram also MD simulations must play a key role. One of the reasons for this is that it is very difficult to get detailed experimental information about the particle behavior inside a 3-D bed, whereas in MD simulations this information is readily available. Another reason is that there is no limit on the shaking strength in MD simulations. This becomes particularly important when we study the transition from the convective state to a granular gas, which occurs at shaking strengths beyond the reach of our shaker. It may be anticipated that this transition will be well-described by hydrodynamic theory, because this approach works best at strong fluidization.

Also in the context of Chapter 5 it will be very interesting to increase the dimensionality of the system. We anticipate that the 2-D version of the one dimensional tube of inelastic particles will show a less sharp localization of the energy exchange (so the dilute region is no longer a Knudsen gas) and hence that granular hydrodynamics may give good results.

An interesting extension would be to slowly increase the influence of gravity by tilting the system. At low tilting angles one then gets a system very similar to the one studied by Kudrolli *et al.* [26], where one sees that the cluster becomes less attached to the insulating (upper) wall. By gradually increasing the tilting

angle (up to 90 degrees) we will witness the transition to the vertical Leidenfrost effect of Chapter 3.

Next to the MD simulations and hydrodynamic theory presented in Chapter 5, we would also propose to do the corresponding experiments: To perform the experiment in "one-dimension" one can think of a horizontal rail blowing air through tiny holes, thereby elevating gliders that act like particles moving over the rail almost without friction. A vibrating wall on one side and a reflective wall on the other make the setup complete.

The position of the cluster's center of mass x_{CM} can be further studied, numerically and experimentally, by means of its probability distribution function (PDF). We expect that the PDFs for different restitution coefficients e can be rescaled to get a self-similar solution, and thereby shed light on the singular behavior of the system in the elastic limit $e \to 1$.

For the granular ratchet experiments of Chapter 6 it is experimentally not feasible to record the collisions of the particles with the vanes, so also the feedback of the vanes to the gas cannot be measured. We therefore propose to apply MD simulations to study the granular ratchet on the level of particle-vane collisions. We expect that the MD velocity field of the granular gas will confirm the presence of a large scale particle circulation, which we have conjectured to be the cause of the double-peaked velocity distribution at very strong fluidization.

In Chapter 7 we have indicated that surfactants are crucial for the Leidenfrost stars. It is therefore important to perform a study in which the amount of surfactants is varied in a controlled way. We are aware that a systematic study of the effect of surfactants is experimentally challenging [27], but we expect that the influence of the surfactants on the oscillation frequency of the Leidenfrost stars will be strong enough to yield a definitive answer.

In this thesis we have shown that hydrodynamic theory is able to describe phenomena observed in vertically shaken granular matter. To explore the applicability of granular hydrodynamics further, we think it is now crucial to put it to the test in granular systems that are only partially dynamic, such as an avalanche, granular jet and a flowing hopper. Successful hydrodynamic descriptions for some of these systems have been achieved already [28–30], and the challenge of granular research today is to form a general granular hydrodynamic theory in which the constitutive relations (including corrections for finite particle size) play a key role.

References

[1] Y. Du, H. Li, and L. P. Kadanoff, *Breakdown of hydrodynamics in a one-dimensional system of inelastic particles*, Phys. Rev. Lett. **74**, 1268 (1995).

[2] S. B. Savage, *Streaming motions in a bed of vibrationally fludized dry granular material*, J. Fluid Mech. **194**, 457 (1988).

[3] F. Melo, P. B. Umbanhowar, and H. L. Swinney, *Transition to parametric wave patterns in a vertically oscillated granular layer*, Phys. Rev. Lett. **72**, 172 (1994).

[4] F. Melo, P. B. Umbanhowar, and H. L. Swinney, *Hexagons, kinks, and disorder in oscillated granular layers*, Phys. Rev. Lett. **75**, 3838 (1995).

[5] C. R. Wassgren, C. E. Brennen, and M. L. Hunt, *Vertical vibration of a deep bed of granular material in a container*, J. Appl. Mech. **63**, 712 (1996).

[6] T. H. Metcalf, J. B. Knight, and H. M. Jaeger, *Standing wave patterns in shallow beds of vibrated granular material*, Physica A **236**, 202 (1997).

[7] S. S. Hsiau and S. J. Pan, *Motion state transitions in a vibrated granular bed*, Powder Technology **96**, 219 (1998).

[8] C. Bizon, M. D. Shattuck, J. B. Swift, W. D. McCormick, and H. L. Swinney, *Patterns in 3D vertically oscillated granular layers: Simulation and experiment*, Phys. Rev. Lett. **80**, 57 (1998).

[9] N. Mujica and F. Melo, *Solid-liquid transition and hydrodynamic surface waves in vibrated granular layers*, Phys. Rev. Lett. **80**, 5121 (1998).

[10] N. Mujica, L. Caballero, and F. Melo, *Collective motion and solid-liquid type transitions in vibrated granular layers*, Physica A **263**, 362 (1999).

[11] O. Sano, *Random motion of a marker particle on square cells formed on vertically vibrated granular layers*, J. Phys. Soc. Jpn. **68**, 1769 (1999).

[12] P. B. Umbanhowar and H. L. Swinney, *Wavelength scaling and square/stripe and grain mobility transitions in vertically oscillated granular layers*, Physica A **288**, 344 (2000).

[13] D. Blair, I. S. Aranson, G. W. Crabtree, V. Vinokur, L. S. Tsimring, and C. Josserand, *Patterns in thin vibrated granular layers: Interfaces, hexagons, and superoscillons*, Phys. Rev. E **61**, 5600 (2000).

[14] J. M. Hill, M. J. Jennings, D. V. To, and K. A. Williams, *Dynamics of an elastic ball bouncing on an oscillating plane and the oscillon*, Appl. Math. Modelling **24**, 715 (2000).

[15] J. R. de Bruyn, B. C. Lewis, M. D. Shattuck, and H. L. Swinney, *Spiral patterns in oscillated granular layers*, Phys. Rev. E **63**, 041305 (2001).

[16] S. J. Moon, M. D. Shattuck, C. Bizon, D. I. Goldman, J. B. Swift, and H. L. Swinney, *Phase bubbles and spatiotemporal chaos in granular patters*, Phys. Rev. E **65**, 011301 (2001).

[17] K. Kim and H. K. Pak, *Coarsening dynamics of striped patterns in thin granular layers under vertical vibration*, Phys. Rev. Lett. **88**, 204303 (2002).

[18] D. I. Goldman, J. B. Swift, and H. L. Swinney, *Noise, coherent fluctuations, and the onset of order in an oscillated granular fluid*, Phys. Rev. Lett. **92**, 174302 (2004).

[19] Y. S. Wong, C. H. Gan, C. H. Wang, X. Fan, D. J. Parker, A. Ingram, and J. P. K. Seville, *Instabilities in vertically vibrated granular beds at the single particle scale*, Phys. Fluids **18**, 043302 (2006).

[20] L. S. Tsimring and I. S. Aranson, *Localized and cellular patterns in a vibrated granular layer*, Phys. Rev. Lett. **79**, 213 (1997).

[21] T. Shinbrot, *Competition between randomizing impacts and inelastic collisions in granular pattern formation*, Nature **389**, 574 (1997).

[22] I. S. Aranson, L. S. Tsimring, and V. M. Vinokur, *Hexagons and interfaces in a vibrated granular layer*, Phys. Rev. E **59**, R1327 (1999).

[23] H. K. Park and H. T. Moon, *Square to stripe transition and superlattice patterns in vertically oscillated granular layers*, Phys. Rev. E **65**, 051310 (2002).

[24] S. J. Moon, J. B. Swift, and H. L. Swinney, *Role of friction in pattern formation in oscillated granular layers*, Phys. Rev. E **69**, 031301 (2004).

[25] J. Bougie, J. Kreft, J. B. Swift, and H. L. Swinney, *Onset of patterns in an oscillated granular layer: Continuum and molecular dynamics simulations*, Phys. Rev. E **71**, 021301 (2005).

[26] A. Kudrolli, M. Wolpert, and J. P. Gollub, *Cluster formation due to collisions in granular material*, Phys. Rev. Lett. **78**, 1383 (1997).

[27] R. E. Apfel, Y. Tian, J. Jankovsky, T. Shi, X. Chen, R. G. Holt, E. Trinh, A. Croonquist, K. C. Thornton, A. Sacco Jr., C. Coleman, F. W. Leslie, and D. H. Matthiesen, *Free oscillations and surfactant studies of superdeformed drops in microgravity*, Phys. Rev. Lett. **78**, 1912 (1997).

[28] D. Lohse, R. Bergmann, R. Mikkelsen, C. Zeilstra, D. van der Meer, M. Versluis, K. van der Weele, M. van der Hoef, and H. Kuipers, *Impact on soft sand: Void collapse and jet formation*, Phys. Rev. Lett. **93**, 198003 (2004).

[29] J. R. Royer, E. I. Corwin, A. Flior, M. L. Cordero, M. L. Rivers, P. J. Eng, and H. M. Jaeger, *Formation of granular jets observed by high-speed X-ray radiography*, Nature Phys. **1**, 164 (2005).

[30] P. Jop, Y. Forterre, and O. Pouliquen, *A constitutive law for dense granular flows*, Nature **441**, 727 (2006).

9

Summary

Samenvatting

Publications, Talks, and Posters

About the Author

Over de Auteur

Dankwoord

9.1 Summary

Granular matter is the general name for materials consisting of grain-like solids and can be encountered everywhere in our daily life, for instance in the form of sand, sugar, cereals and pills. Numerous industries deal with these kinds of materials, which often cause severe problems during transportation, handling, or storing. The corresponding waste of energy globally adds up to an estimated 500 billion dollar each year.

A lot of hands-on experience has been applied already to industrial applications, but the persistence of the problems with granular matter indicates that there is a great demand for fundamental research to get a better understanding of the underlying physics. The research described in this thesis focuses specifically on the collective phenomena observed in vertically shaken granular matter. In this study experiment, numerical simulation and theory are combined. The central question is to what extent hydrodynamic-like models can describe the phenomena observed in granular systems.

In Chapter 2 an experimental phase diagram for a quasi 2-D system is constructed, showing a wide range of collective phenomena observed in vertically shaken granular matter; bouncing bed, undulations, granular Leidenfrost effect, convection rolls, and granular gas. These phenomena and the transitions between them, which form the main object of study of this thesis, are characterized by the dimensionless shaking acceleration Γ (at mild fluidization), the shaking strength S (at stronger fluidization), and the number of particle layers F.

The granular version of the Leidenfrost effect, in which a dense cluster floats on a dilute layer of fast particles, is studied in more detail in a 2-D setup in Chapter 3. The granular Leidenfrost effect is observed above a critical shaking strength and for a sufficient number of particles. The experimental observations are successfully explained by a hydrodynamic model, which makes the granular Leidenfrost effect a prime example of a collective granular phenomenon captured by hydrodynamic equations.

At strong fluidization counter-rotating convection rolls are formed starting out from the Leidenfrost state. This buoyancy driven granular convection is the subject of Chapter 4, where the experimental observations are confirmed by numerical simulations and correctly captured by a linear stability analysis of the hydrody-

namic model of the Leidenfrost state as presented in Chapter 3. This approach is analogous to the one used to determine the onset of Rayleigh-Bénard convection in ordinary liquids, so once again granular hydrodynamics is successful.

Chapter 5 discusses the horizontal 1-D system of inelastic particles introduced by Du, Li, and Kadanoff (1995) as a classic example of a system in which the hydrodynamic description breaks down. In our view, this system can essentially be treated as a horizontal version of the granular Leidenfrost effect. In the characteristic steady state a single particle commutes between the driving wall and a dense cluster. The density is well captured by a hydrodynamic description incorporating the finite size of the particles. The temperature profile, however, is not described by the hydrodynamic equations, since all energy exchange is localized at the border of the cluster: Granular hydrodynamics at its edge.

In Chapter 6 we present the first granular realization of the Smoluchowski-Feynman ratchet. Our experimental setup consists of four vanes that are allowed to rotate freely in a vertically shaken granular gas. The two sides of the vanes are coated differently to induce a preferential direction of rotation, i.e., the ratchet effect. Originally, in the Gedankenexperiment of Smoluchowski and Feynman the device was submerged in a heat bath at thermal equilibrium, where the second law of thermodynamics prohibits any ratchet effect: No work can be extracted spontaneously from an environment in thermodynamic equilibrium. The granular gas, however, is far from equilibrium, so the granular ratchet *can* work. The device cleverly translates the energy from its noisy environment (which is pumped into the system by the vibrating bottom) into a directed motion. After various chemical motors on the micro-scale, this is the first macroscopic Smoluchowski-Feynman ratchet, and the first one that is able to sustain a continuous rotation.

Finally, in Chapter 7 we turn from granular hydrodynamics to ordinary liquids: Oscillating Leidenfrost stars. These form spontaneously when a drop of water is deposited on a sufficiently hot plate. Particle tracking within the drop reveals that these lateral shape oscillations form just one of the possible modes of motion in which the symmetry of the floating drop is broken. The observed transitions between these modes correspond to a transfer of kinetic energy.

The thesis ends with a general conclusion and outlook in Chapter 8.

9.2 Samenvatting

Granulaire materie, oftewel korrelvormige stoffen zoals zand, suiker, graan en pillen, kom je in het alledaagse leven overal tegen. Daarnaast wordt er in talloze industrieën met dit soort materialen gewerkt. De ervaring leert echter dat er zich tijdens het transport, bewerken, of opslaan van granulaire materie veel problemen voordoen. Naar schatting wordt hiermee jaarlijks een hoeveelheid energie ter waarde van 500 miljard dollar verspeeld.

Tot voor enkele decennia bestonden er vrijwel uitsluitend ad hoc oplossingen voor de industriële processen in kwestie, maar de problemen met granulaire materie blijken hardnekkig te zijn en dit zorgt voor een toenemende vraag naar fundamentele kennis. Het in dit proefschrift beschreven onderzoek richt zich specifiek op de effecten die ontstaan wanneer granulaire materie vertikaal geschud wordt. Hiervoor zijn experimenten, simulaties en theorie met elkaar gecombineerd. Het centrale thema is de vraag in hoeverre de waargenomen effecten te beschrijven zijn met zogeheten hydrodynamische (vloeistof-theoretische) modellen.

Hoofdstuk 2 behandelt het experiment, waarin de volgende fenomenen zijn waargenomen; bouncing bed, undulaties, het granulaire Leidenfrost effect, convectie en een granulair gas. Het blijkt mogelijk deze effecten samen te vatten in één fasediagram, waarbij de schudversnelling Γ, de schudsterkte S en het aantal lagen deeltjes F de relevante parameters blijken te zijn.

Het granulaire Leidenfrost effect wordt vervolgens in meer detail beschreven in Hoofdstuk 3. De naam van dit fenomeen is ontleend aan het 'originele' Leidenfrost effect, waarbij een druppel water minutenlang boven een hete plaat kan blijven zweven op zijn eigen laagje waterdamp. In de granulaire versie 'zweeft' een dicht gepakt cluster van deeltjes op een dunne laag van snelle deeltjes. Dit effect kan pas worden waargenomen als de schudsterkte boven een bepaalde grens komt en er bovendien voldoende deeltjes in het systeem zitten. De experimentele resultaten blijken succesvol beschreven te kunnen worden door een hydrodynamisch model. Dit maakt het granulaire Leidenfrost effect tot een schoolvoorbeeld van een granulair systeem dat zich zowel kwalitatief als kwantitatief gedraagd als een vloeistof.

Bij nog hogere schudsterktes kunnen er convectierollen ontstaan vanuit het Leidenfrost effect. In Hoofdstuk 4 worden deze convectierollen uit het experiment

vergeleken met computersimulaties en blijken ze theoretisch goed beschreven te worden door het toepassen van een lineaire stabiliteitsanalyse op het hydrodynamische model van het Leidenfrost effect uit Hoofdstuk 3. Deze theoretische aanpak is ook gebruikt voor het beschrijven van de Rayleigh-Bénard convectierollen in gewone vloeistoffen, welke je bijvoorbeeld kan zien in een pan water die je aan de kook brengt. Hydrodynamische theorie beschrijft dus wederom met succes een granulair fenomeen.

Hoofdstuk 5 behandelt de horizontale buis met een rij inelastische deeltjes geïntroduceerd door Du, Li en Kadanoff in 1995. Het kan gezien worden als een horizontale versie van het granulaire Leidenfrost effect. In de buis ontstaat na enige tijd een evenwichtssituatie waarin een enkel deeltje heen en weer beweegt tussen de wand waar de energie wordt toegevoerd en het dichte cluster van deeltjes aan de andere, reflecterende wand (zie ook het flipboek op de oneven pagina's). Het dichtheidsprofiel van deze situatie blijkt goed beschreven te worden door een hydrodynamisch model, het temperatuurprofiel echter *niet*, omdat vrijwel alle energie uitwisseling plaatsvindt bij het begin van het cluster. Dit systeem bevindt zich dus precies op de grens van de granulaire hydrodynamica en beantwoordt daarmee de centrale vraag van dit proefschrift, zoals die hierboven geformuleerd is.

In Hoofdstuk 6 presenteren we de eerste macroscopische realisatie van de Smoluchowski-Feynman ratchet. Deze bestaat uit een molentje met vier vaantjes dat vrij rond kan draaien in een vertikaal geschud gas. De twee zijden van elk vaantje hebben een verschillende coating, zodat er een voorkeurs-draairichting ontstaat: Dit heet het ratchet effect. In het oorspronkelijke gedachte-experiment van Smoluchowski en Feynman was dit molentje geplaatst in een normaal gas in thermodynamisch evenwicht. In deze situatie verbiedt de tweede hoofdwet van de thermodynamica dat het ratchet effect optreedt; immers, volgens deze wet kan er geen arbeid spontaan onttrokken worden aan een omgeving in thermodynamisch evenwicht. Een granulair gas bevindt zich echter niet in thermodynamisch evenwicht: Het is deze bijzonderheid die de Smoluchowski-Feynman ratchet in de setting van een granulair gas *wel* mogelijk maakt. De energie die in het granulaire gas alle kanten op gericht is, wordt door het instrument vakkundig omgevormd tot een beweging in één richting. Na diverse chemische ratchets op microscopische schaal is dit de eerste keer dat de Smoluchowski-Feynman ratchet op macroscopisch niveau gerealiseerd is en, belangrijker nog, de eerste waarbij het molentje voortdurend rond kan blijven draaien.

In Hoofdstuk 7 komen we nog eenmaal terug op het Leidenfrost effect, maar nu in de originele versie van een waterdruppel die op zijn eigen damplaag zweeft. Bij een voldoende hoge temperatuur van de plaat begint deze druppel stervormige oscillaties te vertonen: Dit noemen we Leidenfrost sterren. Door kleine deeltjes aan het water toe te voegen kunnen de bewegingen in de druppel gevolgd worden. Hieruit blijkt dat de stervormige oscillaties slechts één van de mogelijke bewegingsvormen zijn, die de oorspronkelijke symmetrie (de ronde vorm) van de zwevende druppel verbreken. In onze experimenten wordt een volledige overdracht van de kinetische energie tussen de verschillende bewegingsvormen waargenomen, wat neer komt op een complete overgang van de ene bewegingsvorm naar de andere.

Tot slot wordt dit proefschrift in Hoofdstuk 8 afgesloten met een algemene conclusie en een vooruitblik voor vervolgonderzoek.

9.3 Publications, Talks, and Posters

Publications

1. Ko van der Weele and Peter Eshuis,
   Zand: Vaste Stof, Vloeistof, of Gas?,
   Proceedings Woudschotenconferentie "Aan het front van de wetenschap",
   Noordwijkerhout, The Netherlands, 12-13 December 2003,
   A. Mooldijk (Ed.), Werkgroep Natuurkunde-Didactiek, University of Utrecht,
   The Netherlands (2004).

2. Ko van der Weele and Peter Eshuis,
   Clusterweek,
   Seven contributions to the "Wetenschappelijke Scheurkalender 2005"
   (Scientific tear-off calendar), 10-16 January 2005,
   Veen Magazines, Diemen, The Netherlands, ISBN: 9076988374 (2004).

3. Matthias E. Möbius, Xiang Cheng, Peter Eshuis, Greg S. Karczmar, Sidney R. Nagel, and Heinrich M. Jaeger,
   Effect of air on granular size separation in a vibrated granular bed,
   Phys. Rev. E **72**, 011304 (2005).

4. P. Eshuis, K. van der Weele, D. van der Meer, and D. Lohse,
   The granular Leidenfrost effect,
   Proceedings of "Powders and Grains 2005", Volume **2**, pp 1155-1158, 2005,
   R. Garca-Rojo, H.J. Herrmann, and S. McNamara (Eds.), Balkema Publ.,
   Leiden, ISBN: 041538348X (2005).

5. Peter Eshuis, Ko van der Weele, Devaraj van der Meer, and Detlef Lohse,
   Granular Leidenfrost effect: Experiment and theory of floating particle clusters,
   Phys. Rev. Lett. **95**, 258001 (2005).

6. Peter Eshuis, Ko van der Weele, Devaraj van der Meer, Robert Bos, and Detlef Lohse,
   Phase diagram of vertically shaken granular matter,
   Phys. Fluids **19**, 123301 (2007).

7. Peter Eshuis, Ko van der Weele, Enrico Calzavarini, Devaraj van der Meer, and Detlef Lohse,
Granular hydrodynamics at its edge: A horizontal array of inelastic particles,
Preprint (2007).

8. Peter Eshuis, Devaraj van der Meer, Ko van der Weele, and Detlef Lohse,
Granular realization of the Smoluchowski-Feynman ratchet,
Preprint (2007).

9. Peter Eshuis, Benjamin Dollet, Olivier Texier, and Devaraj van der Meer,
Oscillations of Leidenfrost stars,
Preprint (2007).

10. Peter Eshuis, Meheboob Alam, Devaraj van der Meer, Ko van der Weele, Stefan Luding, and Detlef Lohse,
Buoyancy Driven Convection in Vertically Shaken Granular Matter: Experiment, Numerics, and Theory,
Preprint (2008).

Talks

1. 22 - 26 September 2003, Cambridge, UK,
Flow Regimes, Transitions and Segregation in Granular & Particle Laden Flows.
Invited talk: Peter Eshuis, *Granular Leidenfrost effect*.

2. 12 - 13 December 2003, Noordwijkerhout, The Netherlands,
Woudschotenconferentie “Aan het Front van de Wetenschap”.
Workshop: Ko van der Weele and Peter Eshuis, *Zand: Vaste Stof, Vloeistof, of Gas?*

3. 20 - 21 January 2005, Lunteren, The Netherlands,
Wetenschappelijke FOM-dagen Statistische Fysica.
Invited talk: Peter Eshuis, *Granular Leidenfrost effect.*

4. 26 June - 10 July 2005, Maribor, Slovenia,
Let’s face Chaos through Nonlinear Dynamics.
Contributed talk: Peter Eshuis, *Granular Leidenfrost effect.*


Cambridge, UK (2003)

Amsterdam, The Netherlands (2005)

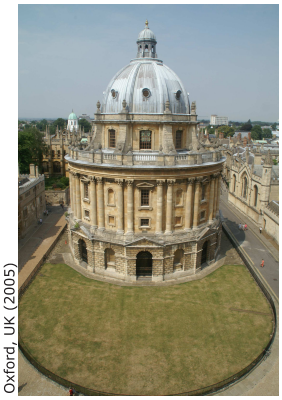
Oxford, UK (2005)


Maribor, Slovenia (2005)

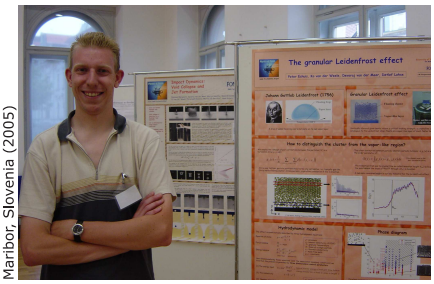

Maribor, Slovenia (2005)

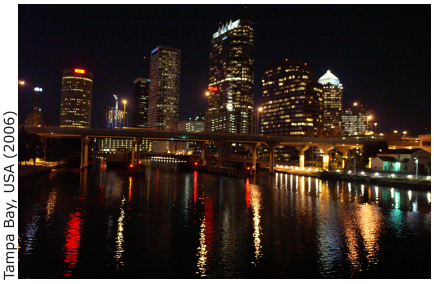
Tampa Bay, USA (2006)


Chicago, USA (2005)


Chicago, USA (2005)

5. 5 October 2005, Enschede, The Netherlands,
   JMBC course: The Physics of Granular Matter.
   Contributed talk: Peter Eshuis, *Rapid granular matter at its edge: Exploring critical phenomena and ratchets.*

6. 15 November 2005, Austin (Texas), USA,
   Center for Nonlinear Dynamics (University of Texas).
   Invited talk: Peter Eshuis, *Granular Leidenfrost effect.*

7. 20 - 22 November 2005, Chicago (Illinois), USA,
   APS-meeting for the Division of Fluid Dynamics.
   Contributed talk: Peter Eshuis, *Granular Leidenfrost effect.*

8. 13 December 2005, Veldhoven, The Netherlands,
   FOM-Decemberdagen 2005.
   Invited talk: Peter Eshuis, *Granular Leidenfrost effect.*

9. 19 - 21 November 2006, Tampa Bay (Florida), USA,
   APS-meeting for the Division of Fluid Dynamics.
   Contributed talk: Peter Eshuis, *Phase diagram of vertically shaken granular matter.*

Posters

1. 27 June - 2 July 2004, Colby College (Maine), USA,
   Gordon Research Conference: Granular & Granular-Fluid Flow.
   Poster: Peter Eshuis, Ko van der Weele, Devaraj van der Meer, and Detlef Lohse, *The granular Leidenfrost effect: Density inversion in vibrofluidized granular matter.*

2. 29 September 2004, Enschede, The Netherlands,
   The scientific meeting of the Research Institute IMPACT.
   Poster: Peter Eshuis, Ko van der Weele, Devaraj van der Meer, and Detlef Lohse, *The granular Leidenfrost effect: Density inversion in vibrofluidized granular matter.*

3. 8 - 9 November 2004, Veldhoven, The Netherlands,
   Wetenschappelijke FOM-dagen Stroming en Warmte.
   Poster: Peter Eshuis, Ko van der Weele, Devaraj van der Meer, and Detlef Lohse, *The granular Leidenfrost effect: Density inversion in vibrofluidized granular matter.*

4. 26 June - 10 July 2005, Maribor, Slovenia,
   Let's face Chaos through Nonlinear Dynamics.
   Poster: Peter Eshuis, Ko van der Weele, Devaraj van der Meer, and Detlef Lohse, *The granular Leidenfrost effect.*

5. 18 - 22 July 2005, Stuttgart, Germany,
   Powders & Grains Conference 2005.
   Poster: Peter Eshuis, Ko van der Weele, Devaraj van der Meer, and Detlef Lohse, *The granular Leidenfrost effect.*

6. 7 - 8 November 2005, Veldhoven, The Netherlands,
   Wetenschappelijke FOM-dagen Stroming en Warmte.
   Poster: Peter Eshuis, Ko van der Weele, Devaraj van der Meer, and Detlef Lohse, *The granular Leidenfrost effect.*

7. 23 - 28 July 2006, Oxford, UK,
   Gordon Research Conference Granular & Granular-Fluid Flow.
   Poster: Peter Eshuis, Ko van der Weele, Devaraj van der Meer, Robert Bos, and Detlef Lohse, *Phase diagram of vertically shaken granular matter.*

9.4 About the Author

Peter Eshuis was born in Hengelo, the Netherlands, on the 12th of January 1980. He attended high school at "De Grundel" (Hengelo), from which he graduated in 1998. Subsequently, he started studying Applied Physics at the University of Twente in Enschede.

In 2002 he performed his three months internship in the research group of Prof. dr. Heinrich Jaeger and Prof. dr. Sid Nagel at the University of Chicago (USA) on "The Multi Intruder Brazil Nut Problem". Here he really got into research on granular matter. Back at the University of Twente he continued granular research with a graduation project in the Physics of Fluids group of Prof. dr. Detlef Lohse. On the 29th of August 2003 he obtained his Master's degree cum laude on the topic "Leidenfrost Effect and Coarsening in a Granular Gas".

He carried on with scientific research as a PhD student under supervision of Prof. dr. Detlef Lohse, Prof. dr. Ko van der Weele and Dr. Devaraj van der Meer at the Physics of Fluids group in Twente, with occasional work visits to the University of Patras (Greece). The results of the research performed in this period are described in this thesis.

9.5 Over de Auteur

Peter Eshuis werd op 12 januari 1980 geboren in Hengelo, alwaar hij opgroeide in de nieuwbouwwijk “Hasseler Es”. Via de nabijgelegen basisschool “De Bron” stroomde hij in 1992 door naar het Atheneum van “De Grundel” te Hengelo. In de derde klas wist hij al dat een exacte studie wel iets voor hem was, hoewel hij toen van de decaan te horen kreeg dat “Technische Natuurkunde toch wel een heel pittige studie was...”. Dit kon hem er niet van weerhouden om, na het afronden van het VWO, vanaf 1998 Technische Natuurkunde aan de Universiteit Twente in Enschede te gaan studeren.

In 2002 liep hij voor zijn studie drie maanden stage in de vakgroep van Prof. dr. Heinrich Jaeger en Prof. dr. Sid Nagel aan de University of Chicago (VS) op het onderwerp “The Multi Intruder Brazil Nut Problem”. Hier was het dat hij gegrepen werd door granulaire materie en specifiek het onderzoek doen naar deze intrigerende materialen. Terug in Twente werd het granulaire pad vervolgt met een afstudeerproject in de Physics of Fluids groep van Prof. dr. Detlef Lohse. Op 29 augustus 2003 studeerde hij cum laude af op het onderwerp “Leidenfrost Effect and Coarsening in a Granular Gas” en verdiende daarmee zijn ir-titel.

Hij had de smaak van het onderzoek nu goed te pakken en nam het aanbod om het granulaire onderzoek nog vier jaar voort te zetten als promovendus met beide handen aan. Dit gebeurde onder leiding van Prof. dr. Detlef Lohse, Prof. dr. Ko van der Weele en Dr. Devaraj van der Meer binnen de Physics of Fluids groep aan de Universiteit Twente, met af en toe een werkbezoek aan de University of Patras (Griekenland). De resultaten van dit promotie onderzoek, waarmee hij op 14 februari 2008 zijn dr-titel hoopt te behalen, zijn beschreven in dit proefschrift.

Ptuj, Slovenia (2005)

9.6 Dankwoord

Zo. Daar is ie dan: Mijn proefschrift, beter bekend als “het boekje”. Het is het resultaat van vier jaar werk. Werk dat ik niet had kunnen verzetten zonder de mensen om mij heen. Veel personen hebben hun steentje bijgedragen, direct dan wel indirect, en hebben mij zo een promotietijd gegeven waar ik met veel genoegen op terugkijk. Het onderzoek kan namelijk nog zo interessant en uitdagend zijn, het is je omgeving die de doorslag geeft of je promotie een succes wordt. Daarvoor ben ik iedereen die hierin een rol heeft gespeeld zeer dankbaar. Een aantal personen wil ik met name noemen:

Allereerst wil ik mijn ouders, Roelof en Cock, bedanken voor de onvoorwaardelijke steun, medeleven en op z’n tijd een warme maaltijd, die ik van jullie heb mogen ontvangen. Hoewel mijn bezigheden soms ongrijpbaar voor jullie waren, kon ik altijd bij jullie terecht. Mijn proefschrift begint dan ook bij jullie.

Detlef (Prof. dr. D. Lohse), ik wil je bedanken dat je me de gelegenheid hebt gegeven om binnen de Physics of Fluids groep te kunnen promoveren. Het was een voorrecht om onder jouw vleugels wetenschap te bedrijven en heb veel geleerd van je kijk op veel verschillende onderwerpen. Wanneer ik vast zat, kon ik altijd bij je terecht ook al zaten er geen gaatjes meer in je agenda. De vele gesprekken en discussies waren altijd zeer duidelijk en verhelderend. Bij terugkomst in mijn kantoor was het dan ook duidelijk wat er gebeuren moest en zo maakten we enorme stappen voorwaarts. Detlef, bedankt voor alle leerzame ervaringen en voor de fijne samenwerking in de afgelopen jaren.

Ko (Prof. dr. K. van der Weele), je was mijn dagelijkse en inspirerende begeleider in dit onderzoek. Tijdens mijn promotie ben je professor in Patras (Griekenland) geworden, maar je vertrek uit Nederland heeft je betrokkenheid bij mijn project niet minder gemaakt. Daar ben ik je dan ook erg dankbaar voor. Mijn twee lange bezoeken aan jou in Griekenland zijn me heel dierbaar en vooral die in de herfst/nazomer van 2007 zal me nog lang heugen: De flow waar we die drie weken in zaten was ongelooflijk. Ik maak van deze gelegenheid gebruik om ook je vrouw Dorothy en je kinderen, Maria-Christina en Pieter, te bedanken voor de gastvrijheid en gezelligheid. Jou wil ik heel hartelijk bedanken voor al je feedback, steun en sturing. Ik prijs me gelukkig dat ik jou als begeleider heb gehad en ik zal onze lange (telefoon-)gesprekken over van alles en nog wat gaan missen...

Devaraj (Dr. D. van der Meer), je bent begin 2006 mijn dagelijkse begeleider geworden op het moment dat Ko naar Griekenland ging. Je theoretische kennis is welhaast onuitputtelijk en daarnaast ben je ook van andere markten thuis: Of het nou ging over experimenten, simulaties of theorie, je had steevast een antwoord op mijn vragen. Onze (wekelijkse) afspraken waren altijd zeer nuttig en brachten orde in mijn soms chaotische gedachten. Je initiatief om kernfusie als dé alternatieve energiebron onder de aandacht te brengen vind ik zeer bewonderenswaardig. Je enthousiasme werkt aanstekelijk! Met veel plezier heb ik met je samengewerkt en bedank je daarom voor de goede begeleiding en vele inspirerende (leer-)momenten.

Verder wil ik iedereen uit de Physics of Fluids groep bedanken: Aaldert, Adrian, Amy, Andrea, Arjan, Aurore, Bas, Benjamin, Bram, Chao, Christian, Christoph, Claus-Dieter, Daniel, Dennis, Edip, Enrico, Francisco, Gabriel, Gerrit, Gert-Wim, Hanneke, Henk Jan, Jeroen, Jiong, Joanita, Jos, Julian, Kazuyasu, Leen, Manish, Marlies, Martin, Mauro, Michel, Nico, Nicolas, Paolo, Philippe, Ramon, Raymond, René, Roger, Rory, Sander, Sascha, Stefan, Stephan D., Stephan G., Valeria, Wim, en alle bachelor/master studenten. Ik kan wel zeggen dat ik enorm heb genoten van alle conferenties, cursussen, uitjes, feestjes, flesjesavonden, PoF United voetbalwedstrijden, koffie- en lunchpauzes en dergelijke, die we met elkaar gedeeld hebben. Het zal straks nog raar zijn om me niet meer dagelijkse binnen de PoF-groep te begeven.

Uit deze groep wil ik nog een specifiek woord van dank richten tot mijn (ex-) kantoorgenoten Devaraj, Raymond, Gabriel en Stefan: Thanks for the good laughs, great help and nice company, it was a pleasure sharing an office with you guys!

Zonder de ondersteuning van de technici, Gert-Wim en Martin, systeembeheerder Bas en secretaresse Joanita was alles heel wat minder soepel gelopen. Bedankt voor de hulp bij de diverse setups, bij het zoeken wanneer er weer eens iets onverklaarbaar verdwenen was, bij het vastlopen van mijn computer en voor het aangeven van de juiste weg in de administratieve jungle.

Daarnaast bedank ik Robert Bos (master student) en Stijn Klaassen (bachelor student) voor de constructieve samenwerking en de behaalde resultaten, and I wish to thank Jean Walter and Olivier Texier: It has been a pleasure collaborating with you during your internships and we have achieved some nice results and insights.


Patras, Greece (2006)


Lutterzand, The Netherlands (2006)


Enschede, The Netherlands (2006)


Maribor, Slovenia (2005)

I would like to express my gratitude to my co-authors for the fruitful collaborations:

Meheboob Alam, you were really the right person at the right place in November 2007. I'm grateful that during the three weeks of your visit, thanks to your expertise on spectral methods, we achieved the theoretical breakthrough in the granular convection project.

Stefan Luding, I learned a lot from you on numerical simulations and the hours we spent harvesting the results of the simulations were always very cheerful. The pictures rendered from the convection simulations are truly beautiful, but more importantly give nice insight in parameters unavailable in the experiments. Thank you for the pleasant and productive collaboration.

Benjamin Dollet, bij je vertrek naar Rennes (Frankrijk) vroeg je me om in het Nederlands te blijven communiceren. Daarom schrijf ik dit stukje in het Nederlands en bedank ik je voor de buitengewone samenwerking in het Leidenfrost Stars project. Toen je in de groep kwam, liep ik al een tijdje met het plan rond om dit effect eens grondig te bestuderen. Tijdens een lunchpauze vertelde ik je erover en je werd meteen enthousiast, waarna dit project begon te lopen. Samen waren we een goed team, waarin we elkaar goed aanvulden. Hartelijk bedankt daarvoor.

Enrico Calzavarini, our project on the 1D tube with inelastic particles started

out as a small side project. While studying the system in greater detail, however, we were continuously surprised by the richness of this very simple system. All the discussions we had, in which we often stared at each other baffled by another freshly discovered feature, are very precious to me. Mille grazie, mille grazie.

Ik wil ook de Fundamentals of Chemical Reaction Engineering groep van Hans Kuipers bedanken voor de fijne samenwerking. Met name Martin van der Hoef, Christiaan Zeilstra en Wouter Dijkhuizen wil ik bedanken voor de interessante discussies en het voort helpen met het bestellen of lenen van glazen deeltjes in alle soorten en maten.

Furthermore I'd like to thank Heinrich Jaeger from the University of Chicago (USA) for introducing me into the beautiful world of granular matter during my internship in 2002. It was at that moment that I was triggered and really got interested in research on granular matter. The fire that got started back then is still burning strong and brought me to this PhD thesis. Therefore I'm very pleased that you were available and accepted to be a member of my graduation committee.

Mijn vrienden en (schoon-) familie wil ik heel hartelijke bedanken voor de gezellige uurtjes samen en hoewel ik jullie de laatste tijd wat minder gezien heb, ben ik blij dat jullie me af en toe op sleeptouw hebben genomen voor de broodnodige ontspanning. Jullie interesse en steun zijn me heel dierbaar.

Mijn paranimfen, Henk Jan en Bertine, wil ik speciaal bedanken dat jullie er altijd voor me zijn. Als collega en zus delen we veel met elkaar en ik vind het dan ook erg fijn dat ik jullie bij deze speciale gelegenheid dichtbij me kan hebben.

Janneke, ik weet niet hoe ik jou kan bedanken voor al je liefde, steun en vertrouwen, die je me de afgelopen jaren hebt gegeven. Samen zullen we daarop voort bouwen, waarbij ik niet meer bij nacht en ontij mijn bed hoef uit te springen om weer wat aan mijn proefschrift te doen. Ik ben je enorm dankbaar dat je er voor me bent en ik kijk met nieuwsgierigheid om de hoek om te zien wat de toekomst ons brengen gaat.

Wat je nog meer kan leren van granulaire materie

Als de dingen in je leven je even allemaal te veel worden, als 24 uur in een dag niet meer genoeg tijd lijkt, denk dan eens aan dit verhaal...

Een leraar stond voor de klas met een aantal voorwerpen voor zich liggen. Toen de les begon, nam hij zonder iets te zeggen de lege pot van de mayonaise en begon deze te vullen met golfballetjes. Toen deze hier helemaal mee gevuld was, vroeg de leraar aan zijn studenten of de pot nu helemaal vol was. Zij antwoordden van wel.

Toen nam de leraar een doos met kralen en kiepte deze in de pot. Hij schudde lichtjes met de pot en de kralen rolden tussen de open plekken tussen de golfballetjes. Weer vroeg de leraar aan zijn studenten of de pot nu vol was. Ze gaven weer hetzelfde antwoord: Ja, de pot is vol.

De leraar nam nu een doos met zand en kiepte dit zand in de pot met golfballetjes en kralen. Natuurlijk vulde het zand alle ruimte op tussen de golfballetjes en de kralen. Weer vroeg de leraar aan zijn studenten of de pot nu vol was: De studenten antwoordden van wel.

Van onder het bureau nam de leraar nu twee koppen koffie en kiepte de hele inhoud van deze twee koppen koffie in de pot met golfballetjes, kralen en zand. De koffie vulde de ruimte op tussen het zand. De studenten begonnen te lachen.

“Nu”, zei de leraar, “nu wil ik dat jullie deze pot zien als jullie eigen leven. Deze pot gevuld met golfballetjes, kralen, zand en koffie, stelt namelijk het leven van een mens voor. De golfballetjes zijn de belangrijke dingen in het leven: Je familie, je kinderen, je geloof, je gezondheid en je favoriete bezigheden. Dingen die ervoor zorgen dat als er niets meer op de wereld was dan deze dingen, je leven toch gevuld zou zijn. De kralen zijn de dingen die daarna belangrijk zijn. Je werk, je huis, je auto. Het zand, dat staat voor de kleine dingetjes in je leven.”

“Als je het zand als eerste in de pot kiept en hem hiermee vult, is er geen plek meer voor de kralen of voor de golfballetjes. Datzelfde geldt ook voor je eigen leven. Als je al je tijd en energie aan de kleine dingetjes besteedt, dan kun je nooit meer ruimte hebben voor de dingen die belangrijk voor je zijn. Besteed aandacht aan de dingen die belangrijk voor je zijn. Speel bijvoorbeeld met je kinderen. Neem

je partner mee uit eten. Doe nog iets leuks, er is altijd nog wel ergens tijd om het huis te poetsen of dat kledingstuk te repareren."

"Zorg eerst voor de golfballetjes, de dingen die echt het allerbelangrijkste voor je zijn. Stel je prioriteiten. De rest is maar zand."

Eén van de studenten steekt een vinger op en vraagt waar de twee koppen koffie in die pot dan voor zouden moeten staan.

De leraar lacht en zegt de student dat ze daarmee een heel goede vraag heeft gesteld. "Ik wilde daarmee alleen nog maar weer eens aangeven en bevestigen, dat, hoe vol je leven ook mag zijn, er is altijd wel een plekje om samen met een vriend of een dierbare een kopje koffie te drinken."

Agia Efimia, Greece (2006)

Stellingen

behorende bij het proefschrift van Peter Eshuis:

COLLECTIVE PHENOMENA
IN VERTICALLY SHAKEN
GRANULAR MATTER

14 februari 2008

1. Voor de collectieve fenomenen die optreden wanneer granulaire materie zachtjes geschud wordt, is de schudversnelling Γ de relevante dimensieloze parameter. Bij harder schudden neemt de schudsterkte S deze rol over.
   Dit proefschrift, Hoofdstuk 2

2. De effecten die men waarneemt in een granulair systeem dat voldoende hard geschud wordt, voldoende deeltjes bevat en tenminste twee ruimtelijke dimensies heeft, laten zich voortreffelijk beschrijven met hydrodynamisch modellen.
   Dit proefschrift, Hoofdstuk 2, 3, 4 en 5

3. De viscositeit van een granulaire vloeistof blijkt direct gerelateerd te zijn aan de energiegeleiding door het systeem via het dimensieloze getal van Prandtl, waarbij dit getal net als in gewone vloeistoffen van orde 1 is.
   Dit proefschrift, Hoofdstuk 4

4. Een granulair gas vormt de ideale achtergrond voor de Smoluchowski-Feynman ratchet, aangezien de tweede hoofdwet van de thermodynamica op zo'n gas niet van toepassing is.
   Dit proefschrift, Hoofdstuk 6

5. De stervormige oscillaties die optreden in een waterdruppel zwevend op een gloeiende plaat heter dan 320 °C volgen precies de capillaire eigenfrequentie die behoort bij de grootte van de druppel.
   Dit proefschrift, Hoofdstuk 7

6. De sterkte van een artikel ontstaat door de onverwachte resultaten, die je in eerste instantie uit het veld slaan, ten goede te keren.

7. Hoe meer je je in de natuur verdiept, hoe mooier zij wordt en daarin vindt de wetenschapper nog altijd zijn/haar voornaamste drijfveer.

8. Veel weten is mooi, je kennis en kunde goed over kunnen brengen is nog veel mooier. Het verstandig gebruik van beeldspraak die iedereen herkent, kan zelfs de lastigste materie verteerbaar maken én laten beklijven.

9. Of een verschijnsel tegenintuïtief is, hangt af van het perspectief waarin men zich bevindt.

10. Wanneer je iets snel gedaan wilt hebben, geef het dan aan iemand met een druk bezette agenda.